ABSTRACT

Bayarbadrakh, Baramsai. Neutron Capture Reactions on Gadolinium Isotopes. (Under the direction of Dr. G. E. Mitchell and U. Agvaanluvsan).

The neutron capture reaction on ^{155}Gd, ^{156}Gd and ^{158}Gd isotopes has been studied with the DANCE calorimeter at Los Alamos Neutron Science Center.

The highly segmented calorimeter provided detailed multiplicity distributions of the capture γ-rays. With this information the spins of the neutron capture resonances have been determined. The new technique based on the statistical pattern recognition method allowed the determination of almost all spins of ^{155}Gd s-wave resonances. The generalized method was tested for s- and p-wave resonances in ^{94}Mo and ^{95}Mo isotopes. The results were compared with previous resonance data as well as results from other methods.

The ^{155}Gd(n,γ)^{156}Gd cross section has been measured for the incident neutrons energy range from 1 eV to 10 keV. The results are in good agreement with other experiments. Neutron resonances parameters were obtained using the multilevel R-matrix code SAMMY. The fitted radiation and neutron widths, Γ_γ and Γ_n were compared with the nuclear data library ENDF/B-VII.0 and with a recent experiment at RPI.

With the new spin assignments and resonance parameters, level spacings and neutron strength functions were determined for s-wave resonances in ^{155}Gd.

The Monte Carlo code DICEBOX was used to simulate the γ-decay of the compound nuclei ^{156}Gd, ^{157}Gd and ^{159}Gd. The DANCE detector response was taken into account with a GEANT4 simulation. The simulated and experimental spectra were compared to determine suitable model parameters for the photon strength functions (PSFs) and the level density (LD). The shape of the photon strength function which gave the best agreement with the DANCE spectra contained four low-lying Lorentzian resonances, two for the scissors mode and two for the M1 spin flip mode.

Neutron Capture Reactions on Gadolinium Isotopes

by

Bayarbadrakh Baramsai

A dissertation submitted to the Graduate Faculty of
North Carolina State University
in partial fullfillment of the
requirements for the Degree of
Doctor of Philosophy

Physics

Raleigh, NC

2010

Approved By:

Dr. Mohamed A. Bourham	Dr. Christopher R.Gould
Dr. John H. Kelley	Dr. Undraa Agvaanluvsan Co-chair of Advisory Committee
Dr. Gary E. Mitchell Chair of Advisory Committee	

DEDICATION

To my parents, N.Baramsai and L.Ulziibuyan

BIOGRAPHY

Bayarbadrakh Baramsai

Personal information

Born 21 January 1978, Zavkhan, Mongolia
Married with Oyu Batbold, 3 children

Education

M.S. in physics, National University of Mongolia, 2003
B.S. in physics, National University of Mongolia, 1999

Professional Experience

Research Assistant, North Carolina State University, 2007 to present

Teaching Assistant, North Carolina State University, 2006-2007

Junior researcher, Frank Laboratory of Neutron Physics, JINR, Dubna, Russia, 2004-2006

Research Assistant, Nuclear Research Center, National University of Mongolia, 2001-2004

Researcher, Mongolian National Center for Standardization and Metrology, 1999-2001

ACKNOWLEDGMENTS

This work was completed with the help of many people to whom I owe a great debt. My first and foremost thanks go to Prof. Gary E. Mitchell for his support and valued advice throughout my graduate study and for giving me a great opportunity to work at Los Alamos National Laboratory. His guidance and editing in order to make this thesis readable is especially appreciated.

I am also grateful to Dr. U. Agvaanluvsan and Dr. D. Dashdorj for their suggestions and support during my Ph.D. program at NCSU. I would like to thank the other members of my graduate committee Dr. Mohamed A. Bourham, Dr. Christopher R.Gould and Dr.John H. Kelley.

A huge debt of gratitude is owed the DANCE collaborators and researchers of the LANSCE-NS group for their hospitality and for the friendly environment. I would especially like to thank Dr. J. Ullmann, Dr. A. Couture and Dr. M. Jandel for their encouragement of my research and many valuable discussions. From these people, I always found an answer to my questions related to nuclear physics clearly and quickly. Doing research with this effective working group was a great help in finishing my Ph.D. program in a relatively short time. I am especially indebted to Dr. M. Krticka, Charles University, Prague, for his help on the DICEBOX simulations. The discussions with Dr. F. Tovesson and Dr. K. M. Hanson were very helpful in using a pattern recognition method for the spin assignments.

I also would like to thank the professors of the Physics Department at NCSU for their enlightening lectures. I thank Mrs. Ina E. Lunney, Mrs. Megan M Freeman and Mrs. Julie Quintana-Valdez for their professional administrative assistance.

The second part of my acknowledgment is to people who I knew before I pursued my graduate study at NCSU. I am deeply thankful to Prof. G. Khuukhenkhuu for his long time support and encouragement. I also thank to Profs. B.Dalkhsuren, N.Ganbaatar, P.Zuzaan, G. Ochirbat, S.Lodoisamba, Ch. Bayarkhuu, S. Davaa, D. Sangaa, M. Ganbat, Kh. Odbadrakh and N. Norov. There are many more faculty and staff members of the National University of Mongolia to whom I say thanks.

It was a great privilege to work in the Frank Laboratory of Neutron Physics in Dubna. I would like to thank Dr. Yu.M.Gledenov, P.V. Sedyshev, M.Sedysheva, P.J. Shalanski and Nikolai Ivanovich for hosting my research in Dubna.

Many warm and happy memories accumulated related to my friends. I thank to all of my friends for their long time friendship.

My deepest gratitude goes to my family for their unflagging love and support throughout my life. (In Mongolian) Namaig turuulj, udii zeregt hurtel usguj ugsun hairt aav N.Baramsai, eej L.Ulziibuyan nartaa yunii umnu mehiin eoslie. Ta hoeriin maani hair, umug tushig uguigeer minii uchuuhen amjilt herhen tusuulugduh bilee. Mun hairt ah B.Galbdrakh duu B.Oyunbadrakh bolon tednii ger buliihend bugded n bayarlalaa gej helie. Hadam eej Ts. Nandintsetsegt, nadad uuriin tursun huu shig handaj, itgej baidagt n chin setgeleesee talarhaj baina. Busad buh hamaatnuuddaa ner durdalguigeer bugded n tomoos tom talarhaliin ug ilgeej baina.

Last, but most definitely not least, my deepest thanks goes to my wife B. Oyu and our children B. Ujin, B. Bilegtugs and B. Tugsmergen for their love and patience when I was away from family responsibilities and concentrating on my studies. Without her help and encouragement, this thesis would not have been completed.

TABLE OF CONTENTS

LIST OF TABLES

LIST OF FIGURES

Chapter 1

Introduction

In this thesis we present the results of neutron capture experiments on gadolinium isotopes. The experiments on ^{155}Gd, ^{156}Gd and ^{158}Gd isotopes were performed at the Los Alamos Neutron Science Center (LANSCE) using the state-of-the-art Detector for Advanced Neutron Capture Experiments (DANCE). The major results from these experiments can be divided into three parts. First, a new method to determine the spin of the neutron resonances is introduced. Using this new technique, we assigned a spin to almost all resonances in ^{155}Gd. Second, the ^{155}Gd(n,γ)^{156}Gd cross section was measured for the incident neutron energy range from 1 eV to 10 keV. Resonance parameters such as Γ_n and Γ_γ were extracted from the experimental cross section. Lastly, the radiative decay of the compound nucleus was studied in the framework of the statistical model of nuclear reactions. Phenomenological model parameters were established to describe the low energy behavior of the Photon Strength Function (PSF)

a. Determining the neutron resonance spins: The spin of the neutron resonances is an important parameter for resonance analysis, such as the spin dependence of the strength function, level density and average radiative width. The resonance spin is $\vec{J} = \vec{I} + \vec{l} + 1\vec{/}2$, where $\vec{I}$ is the spin of the target nucleus, $\vec{l}$ is the angular momentum of the incident neutron and $1\vec{/}2$ is neutron spin. Because of the centrifugal potential barrier, the s-wave ($l = 0$) neutrons interact more strongly with nuclei than the p-wave ($l = 1$) or higher angular momentum neutrons. As a consequence, resonances observed in medium-weight and heavy nuclei at low neutron energies are in almost all cases s-wave. All s-wave resonances on an even-even target have the same spin, while neutron resonances in odd-A

samples have two spin possibilities, $J = I + 1/2$ and $J = I - 1/2$.

The DANCE detector consists of 160 BaF_2 scintillation crystals surrounding a target with $\sim 4\pi$ solid angle. The highly efficient system detects most of the γ-rays emitting from the compound nucleus; the high segmentation gives valuable information about the γ-ray multiplicity (the number of γ-rays from the compound nuclear resonance in one cascade). The excited compound nucleus reaches its ground state after several successive γ-decays. Each γ-ray in the cascade carries part of the excitation energy and the total angular momentum. Obviously the total energy of the γ rays is equal to the initial excitation energy and the sum of the angular momenta is equal to the spin difference of the initial and final states. In other words, the compound nuclei emit γ-rays with different energies and multipolarities. The emission probability of a given γ ray is dependent on the transition type: electric dipole (E1), magnetic dipole (M1) etc. One expects that the average number of γ rays emitted by the compound nucleus contains information about the spin of the initial state. Experiments and Monte Carlo simulations of the γ-ray cascade combined with detector response simulations demonstrated that the γ-ray multiplicity distributions can be used for spin assignment of neutron resonances. In recent years, several variations of the γ-ray multiplicity method were introduced and spin assignments were made for the resonances measured by DANCE detector. In this thesis, we introduce a new spin assignment method that has some improvements on the previous techniques. This new method was applied to the s- and p-wave resonances in ^{155}Gd, ^{94}Mo and ^{95}Mo.

b. Capture Cross Section: The neutron capture cross-section is a very important in many practical applications. Gadolinium has the highest absorption cross section for thermal neutrons for any stable nuclide. Since it has a very large cross section, accurate knowledge of the cross section is of considerable interest in reactor control applications. It is used as a secondary, emergency shut-down measure in some nuclear reactors, particularly of the CANDU type. Also, it is very effective for use with neutron radiography and in shielding nuclear reactors.

The magnitude of the nuclear cross section can vary greatly with incident neutron energy, as well as for different target nuclei. In the epithermal energy region, the cross section has sharp rises known as resonances. The neutron capture resonances are parametrized by the resonance energy E, the neutron width Γ_n, the radiative width Γ_γ, and the spin and parity J^π. Determination of the quantum numbers of individual nuclear states are also of

interest from a theoretical viewpoint. The resonance energy corresponds to discrete energy levels in the compound nucleus – these provide information on the nuclear level density. The average spacing between successive resonances is the the average level spacing. The individual neutron resonance parameters help provide average nuclear properties such as the s-wave (or p-wave) strength function and the average radiative width that are useful in global systematics. The mass numbers of the stable Gd isotopes, $152 \leq A \leq 160$, places them in the valley of the split $4s$ giant resonance of the s-wave strength function. Accurate experimental values help to establish appropriate optical potential parameters. Global systematics such as the mass number dependence of the s-wave strength function or of the level density parameters are especially important for theoretical predictions of cross-sections on radioactive nuclei for which no experimental data is available.

c. Photon Strength Function: There are many theoretical models and codes used to understand nuclear reaction mechanisms and to utilize them in practical applications. The Hauser-Feshbach (HF) statistical model of nuclear reactions has been used extensively for the determination of nuclear cross sections in nuclear data libraries and nuclear reaction rates for astrophysics. Nuclear level densities (LD) and photon strength functions (PSF) are the important ingredients in HF theory.

Experimentally obtained γ-ray spectra have a complicated dependence on both the PSFs and the LD. The inverse problem – to recover the energy dependence of PSF and LD from experimental spectra – is almost impossible. But, the experimental γ-ray spectra can be reproduced by Monte-Carlo simulation since the γ-decay cascade is usually a purely statistical process. The predicted PSF and LD models are inputs to the simulation code. Currently, no completely consistent theory of the PSFs has been produced. Many phenomenological models have been introduced to explain various experimental evidence. As a result, we tried many combinations of the PSFs and the LD to find a model that reproduces experimental spectra. The parameters of the "best fit" models were obtained and interpreted.

This thesis is composed of 7 chapters and 8 appendices. As is traditional, the first and the last chapters are the Introduction and Summary. Chapter 2 provides some basic understanding about the theoretical aspects of neutron induced reactions. Chapter 3 explains experimental details. Chapter 4 introduces the spin assignment method that we have developed and compare with results from previous methods. In Chapter 5 the abso-

lute capture cross section obtained by the DANCE experiment is determined. Based on the experimental data individual resonance parameters are obtained. Chapter 6 compares experimental γ-ray spectra with DICEBOX + Geant4 simulations. The comparison provides the parameters of phenomenological models of the photon strength functions.

Chapter 2

Theoretical Background for the Neutron Capture Reaction

Nuclear reactions are basic for exploring the microscopic nature of nuclei. Depending on the type and/or energy of the interacting particles, the reactions are variously classified and explained by physical theories. Since the neutron has no electric charge, it interacts with atomic nuclei without any Coulomb barrier. This property brings neutron-induced reactions into many practical applications. Theoretical studies of these reactions have developed as one of the most important branches of nuclear physics. Here we focus on the neutron capture reaction. We briefly review aspects of neutron capture reactions in this chapter.

In a neutron radiative capture reaction, a bombarding neutron is absorbed by the target nucleus to form a heavier isotope of the target element, followed by the emission of one or more γ-rays which carry off the excitation energy. The excitation energy of the compound nucleus is equal to the sum of the neutron separation energy and the kinetic energy of the bombarding neutron.

The reaction mechanism depends crucially on the incident neutron energy. A schematic diagram of the reaction mechanism is shown in Fig. 2.1. Consider the collision of an incident particle with a nucleus. The incident particle may penetrate into the nucleus, collide with some nucleon, and excite it to a level above the Fermi surface. Then there appears a vacancy (hole) at some lower-lying level. The incident nucleon, having left the entrance channel, also occupies a level above the Fermi surface. The state thus formed may

be regarded as a two-particle-one-hole (2p1h) excited state of the compound system. If at least one of the two nucleons possesses an energy higher than that required for separation, there are two possible results: (1) the nucleon may leave the nucleus without interacting with any other nucleon – this is called a direct reaction; (2) the nucleon may collide with some other nucleon and thus form a three-particle-two-hole (3p2h) excited state of the compound system. If none of the nucleons in the 2p1h state has sufficient energy to leave the nucleus, then the second alternative is the only possible one. Afterwards, the nucleon undergoes collisions with other nucleons, and the excitation energy is gradually distributed among many or all the nucleons of the compound system. Compound (2p1h) states are referred to as doorway states.

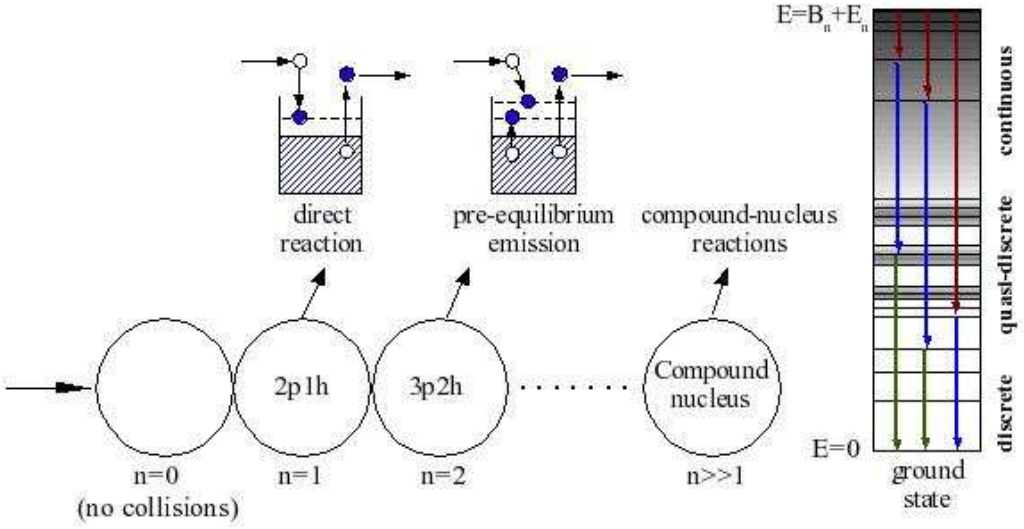

Figure 2.1: A schematic diagram of the reaction processes.

At higher incident energies (well above 10 MeV), it is highly probable that direct-reactions will dominate. On the other hand, if the incident energy is sufficiently low, the incident neutron is absorbed by the nucleus and the excitation energy is distributed among the nucleons long before some particle escapes from the nucleus. This is defined as compound nucleus formation. Direct and compound-nuclear reactions are the limiting cases. In reality, there occur many nuclear reactions of an intermediate nature. A compound system formed as the probe is captured by the nucleus may decay before the incident particle energy is distributed among all the nucleons of the target (pre-equilibrium emission). The direct and

the pre-equilibrium reaction mechanisms are not discussed in this thesis.

In the following sections we will briefly review the formal theory of nuclear reactions and provide some detail about compound-nuclear reactions in the framework of the statistical model of nuclear reactions.

2.1 Elements of Scattering Theory

There exists a large amount of material explaining the formal theory of nuclear reactions; here we shall only introduce basic concepts and provide equations of scattering theory without derivations. A valuable detailed account of the R-matrix theory of nuclear reactions is given by Lane and Thomas [1]; its application to neutron capture reactions is provided by Lane and Lynn [2].

In a typical nuclear reaction, two nuclear particles collide to produce products different from the initial particles. In scattering theory the term *channel*, $c \equiv (\alpha, l, s, J)$, is introduced to specify incoming or outgoing particles and the relative motion of the pairs. Here α represents the particles that make up the channel; the channel includes mass, charge, spin and all other quantum numbers for each of the two particles, l is the orbital angular momentum of the relative motion of the particles, s is a channel spin that is the vector sum of the spins of the two particles ($\vec{s} = \vec{i} + \vec{I}$), and J is a total angular momentum that is equal to the vector sum of s and l: $\vec{J} = \vec{s} + \vec{l}$.

The processes and states initiated by the reaction can be completely described in terms of the wave function Ψ, which is a solution of the Schrodinger equation

$$(H_0 + V)\Psi = E\Psi, \tag{2.1}$$

where the Hamiltonian H of the system is represented as a sum of kinetic energy operators H_0 and interaction potentials V of all the particles of the system. One can solve this equation [3] with boundary conditions providing the presence of a converging wave in the entrance channel c and diverging waves in outgoing channels. The general solution of the equation in the region in which the interacting potential vanishes may be written

$$\Psi = \sum_c C_c (I_c - \sum_{c'} U_{c',c} O_{c'}), \tag{2.2}$$

where I_c and $O_{c'}$ represent incoming and outgoing waves, respectively, and the quantities $U_{c',c}$ constitute the collision matrix (or S-matrix).

For any reaction, the collision matrix has two very fundamental properties: it is unitary $U^{\dagger}U = 1$ and symmetric $U_{p,q} = U_{-q,-p} = U_{q,p}$. These results follow, respectively, from the conservation of probability and from time-reversal symmetry.

The cross-section is given in terms of the collision matrix as

$$\sigma_{c,c'} = \frac{\pi}{k_{\alpha}^{2}} g_{\alpha}^{J} \left| e^{2iw_c} \delta_{c,c'} - U_{c,c'} \right|^2 \delta_{JJ'}, \tag{2.3}$$

where k_α is the wave number associated with the incident particle pair α, g_α^J is the spin statistical factor and w_c is the Coulomb phase-shift (zero for non-Coulomb channels like neutron capture). The spin statistical factor is given by

$$g_{\alpha}^{J} = \frac{(2J+1)}{(2I+1)(2i+1)}, \tag{2.4}$$

and the center-of-mass momentum K_α by

$$K_{\alpha}^{2} = (\hbar k_{\alpha})^2 = \frac{2mM^2}{(m+M)^2} E. \tag{2.5}$$

Here E is the kinetic energy of the incident particle in the laboratory system.

2.2 R-Matrix Theory

In the general expression (2.3), the reaction cross-sections are completely determined by the collision matrix. Therefore the central problem is to determine the U-matrix. In order to find the U-matrix, it is necessary to characterize the wave function in the internal region where particles actually interact. Since the nuclear force is short range, we can assume a surface separating the interaction region from the region of free motion. If the channel interaction is central, such a surface is a sphere. We denote the channel radius as R_α. Since the wave function must satisfy continuity requirements, the internal and external wave functions, as well as their derivatives, must be equal on the boundary surface. Within the context of these conditions, the U-matrix can be expressed in terms of a matrix R which contains a hypothetical set of states of the system inside the interaction region. There are several alternative derivations and formulations of R-matrix theory, but we do not intend to go deeply into questions of mathematical techniques. In order to give an account of the formal procedure employed in R-matrix theory, we consider the simplest case of spinless

neutral particle potential scattering with a single open channel. The radial part of the Schrodinger equation is given by

$$\frac{d^2u_l}{dr^2} + \left(\frac{2m}{\hbar^2}[E - V(r)] - \frac{l(l+1)}{r^2}\right) u_l = 0. \tag{2.6}$$

Consider an arbitrary state λ with energy E_l and wave function $u_l^{(\lambda)}$ that satisfies Eq. (2.6). Take the equations for two different states and subtract them after multiplying the equation for one wave function by the other wave function. Then integrate the difference over r from zero to interaction range R. Considering $u_l^{(1)} = u_l^{(2)} = 0$ at the origin we obtain the following Green relation

$$\left(\frac{du_l^{(1)}}{dr}u_l^{(2)} - \frac{du_l^{(2)}}{dr}u_l^{(1)}\right) |_{r=R} = \frac{2m}{\hbar^2}[E_2 - E_1] \int_0^R u_l^{(1)}u_l^{(2)}dr. \tag{2.7}$$

Consider a complete set of states within the interaction region. These states are the solutions of Eq. (2.6). From the time reversal invariance of the interaction, the eigenfunctions of these states are real. In Eq. (2.7), using the boundary condition that the derivative of the wave function is zero at $r = R$, one finds the eigenfunctions to be orthogonal in the interaction region:

$$\int_0^R u_l^{(\lambda)}u_l^{(\lambda')}dr = \delta_{\lambda,\lambda'}. \tag{2.8}$$

The real eigenfunctions $u_l^{(\lambda)}$ form a complete set in the interaction region. The true wave function of the compound nucleus is not stationary since the compound system can decay. Instead the wave function for the internal region of the nucleus may be expanded in terms of the complete set of states:

$$\Psi(r) = \sum_\lambda c_\lambda u_l^{(\lambda)}(r), \quad (0 < r < R), \tag{2.9}$$

where

$$c_\lambda = \int_0^R \Psi(r)u_l^{(\lambda)}(r).$$

Making use of Eq. (2.7):

$$c_\lambda = \frac{\hbar^2}{2m}\frac{u_l^{(\lambda)}(R)\left(\frac{d\Psi(r)}{dr}\right)_R}{E_{l\lambda} - E}. \tag{2.10}$$

Substituting Eq. (2.10) into Eq. (2.9) we find

$$\Psi(r) = \frac{\hbar^2}{2m}\left(\frac{d\Psi(r)}{dr}\right)_R \sum_\lambda \frac{u_l^{(\lambda)}(r)u_l^{(\lambda)}(R)}{E_{l\lambda} - E} = G_l^E(r,R)R\frac{d\Psi(R)}{dr}, \tag{2.11}$$

where $G_l^E(r,R)$ employs the definition of the Green function for Eq. (2.6)

$$G_l^E(r,R) = \frac{\hbar^2}{2mR}\sum_\lambda \frac{u_l^{(\lambda)}(r)u_l^{(\lambda)}(R)}{E_{l\lambda} - E}. \tag{2.12}$$

Equation (2.11) relates the wave function of the compound system corresponding to an arbitrary energy E in the internal region. The R-function can be immediately expressed in terms of the Green function boundary value

$$R_l(E) = G_l^E(R,R) = \sum_\lambda \frac{\gamma_{l\lambda}^2}{E_{l\lambda} - E}, \tag{2.13}$$

where the quantity $\gamma_{l\lambda}$ is referred to as the reduced width amplitude and $\gamma_{l\lambda}^2$ as the reduced width of the energy level E_λ:

$$\gamma_{l\lambda}^2 = \frac{\hbar^2}{2mR}[u_l^{(\lambda)}(R)]^2. \tag{2.14}$$

The R-matrix for the multi-channel case is given below and the detailed derivation is given in [1].

$$R_{cc'}(E) = \sum_\lambda \frac{\gamma_{\lambda c}\gamma_{\lambda c'}}{E_\lambda - E}. \tag{2.15}$$

Equation (2.15) gives the general energy dependence of the R-matrix. The quantities $\gamma_{\lambda c}$ and E_λ do not depend on energy. Individual levels λ of the compound nucleus contribute in the R-matrix in an additive way. The poles of the R-matrix (i.e., the compound nucleus energy eigenvalues E_λ) are located on the real energy axis. The different $R_{cc'}(E)$ are associated with these same poles. The residues of the diagonal elements $R_{cc}(E)$ for a pole $E = E_\lambda$ (equal to $-\gamma_{\lambda c}^2$) are related to the residues of the off-diagonal elements $R_{cc'}(E)$ for the same pole (equal to $-\gamma_{\lambda c}\gamma_{\lambda c'}$).

2.2.1 Neutron Resonance Reactions

In the general case the incident neutron wave function penetrates weakly into the nucleus. If the particle energy is equal or close to the resonance level energy E_λ, then the internal wave function is appreciably different from zero. In other words, resonance capture reactions will be observed at the R-matrix poles.

Relation between the R-matrix and the collision matrix U

The R-matrix which describes the external-region behavior of the wave functions u_c, is completely determined by the properties of the compound nucleus, i.e., by the interaction in the internal region. The observable cross-sections, however, are described by the U-matrix responsible for the asymptotic behavior of the wave functions Ψ_c. Therefore in order to relate the observable cross-sections with the properties of the compound systems, one has to express the U-matrix in terms of the R-matrix. The matrix equation is given as

$$U = \omega \left[1 + 2iBRB \frac{1}{1 - iBRB} \right] \omega. \tag{2.16}$$

Here, the diagonal matrices B and ω are $B_{cc'} \equiv \delta_{cc'} \sqrt{k_\alpha R_\alpha}$ and $\omega_{cc'} \equiv \delta_{cc'} e^{-ik_\alpha R_\alpha}$.

Since the collision matrix is unitary and symmetric (and hence, the matrix $\omega^{-1} S \omega^{-1}$ is also unitary and symmetric), the matrix BRB is Hermitian and symmetric. In other words, the R-matrix is real and symmetric.

Breit-Wigner formula for an isolated level

The dispersion formula for the energy dependence of the R-matrix takes into account contributions of many compound nucleus levels. For simplicity, assume that a single level contributes in the sum (Eq. 2.15):

$$R_{cc'}(E) = \frac{\gamma_{\lambda c} \gamma_{\lambda c'}}{E_\lambda - E}. \tag{2.17}$$

This assumption is justified if the resonance is sufficiently well isolated. Substituting Eq. (2.17) in Eq. (2.16) and making use of the U-matrix and the cross-section relation, we obtain the Breit-Wigner formula for the cross-section of the transition from channel c into channel c':

$$\sigma_{cc'} = \frac{\pi}{k_\alpha^2} \frac{\Gamma_c^{(\lambda)} \Gamma_{c'}^{(\lambda)}}{(E - E_\lambda)^2 + \frac{1}{4}\Gamma_\lambda^2}, \tag{2.18}$$

where $\Gamma_c^{(\lambda)}$ and $\Gamma_{c'}^{(\lambda)}$ are partial widths, Γ_λ^2 is the square of the total width of the energy level λ,

$\Gamma_c^{(\lambda)} = 2\gamma_{\lambda c}^2 P_c$, where P_c is a *penetration factor* and $\Gamma_\lambda = \sum_{c=1}^{N} \Gamma_c^{(\lambda)}$.

The spin dependent cross-section of the resonance transition $c \to c'$ may be obtained by multiplying the right hand side of Eq. (2.18) by spin-statistical factor g_α^J (Eq. 2.4).

The individual resonance parameters of the neutron capture reaction are the resonance energy $E_{\lambda,n}$, the widths $\Gamma_n^{(l)}$, Γ_γ and the spin and parity of the resonances. In Chapter

4 and 5 we will introduce experimental methods to determine those individual resonance parameters. For low-energy neutrons and medium nuclei, the experimental measurements produce radiation widths much smaller than neutron widths ($\Gamma_n >> \Gamma_\gamma$).

2.2.2 Statistical Assumptions Concerning Resonance Parameters

The compound nuclear states are extremely complex superpositions of different configurations. Therefore, the quasi-bound states that characterize the system will be represented by a random number which is sum of many approximately independent variables. The randomness of the $\gamma_{\lambda c}$ may be placed on a quantitative basis, as suggested by Porter and Thomas [4]. Porter and Thomas (PT) deduced that the reduced neutron widths of resonances characterized by same quantum numbers obeyed a chi-square distribution of one degrees of freedom – $\nu = 1$:

$$P(x)dx = \frac{1}{\sqrt{2\pi y}} e^{-y/2}, \tag{2.19}$$

where y = $\gamma_\lambda^2/\langle\gamma_\lambda^2\rangle$ The PT distribution is approximately verified experimentally by neutron resonance data, but it is difficult to obtain $\nu = 1$ for several reasons: (i) According to the PT distribution, the smallest widths are the most frequent. Due to finite experimental resolution, a number of these weak resonances remain undetected and a test of the PTD would lead to an incorrect value of ν. (ii) Misidentification of statistical fluctuations as weak resonances will also give an incorrect value of ν. (iii) Many weak s-wave resonances are indistinguishable from strong p-wave resonances. The extra p-wave resonance population will again lead to wrong estimates of ν. (iv) Other factors that affect the sequence of the levels are non-statistical phenomena, such as doorway states.

The width analysis of neutron resonances is a widely used test for missing levels.

The Gaussian Orthogonal Ensemble

Wigner initiated the use of random matrices in nuclear physics to describe the level spacings distribution [5]. In Random Matrix Theory (RMT), the nuclear Hamiltonian H was chosen as real and symmetric, $H_{ij} = H_{ji} = H_{ij}^*$, since the nuclear processes are invariant under time-reversal. Although the real nuclear Hamiltonian is not known, the statistical nature of the matrix elements of H seems clear. The Gaussian Orthogonal Ensemble (GOE) is used to interpret results for the distribution of nuclear states [6,7]. The ensemble is defined

by the probability density $P(H)$ of the matrices H [8]:

$$P(H)d[H] = N_0 exp\left(-\frac{N}{4\lambda^2}Tr(H^2)\right)d[H]. \tag{2.20}$$

Here N_0 is a normalization factor and λ is a parameter which defines the average level density. The volume element in matrix space, $d[H]$, is the product of the differentials dH_{ij} of the independent matrix elements

$$d[H] = \prod_{i<j} dH_{ij}. \tag{2.21}$$

From the symmetry of the matrices (H has $N(N+1)/2$ independent elements), one may writes the probability density as a product of terms each of which depends only on a single matrix element:

$$P(H)d[H] = N_0 \prod_{i\leq j} exp\left(-\frac{N}{4\lambda^2}H_{ij}^2\right)dH_{ij}. \tag{2.22}$$

Therefore, in the GOE the independent matrix elements are uncorrelated Gaussian distributed random variables with zero mean value and a second moment [8]. Another important constraint imposed on $P(H)$ is its invariance under orthogonal transformations of the basis, $P(H)d[H] = P(H')d[H']$ [9]. Each of the matrices belonging to the ensemble may be obtained by orthogonal transformations of H, which also belong to the ensemble. As a consequence, there does not exist a preferred direction in Hilbert space, and the ensemble is generic. Hence, one may infer that the eigenvalues and eigenfunctions are uncorrelated random variables.

For realistic systems Hilbert space is finite. In the limit $N \to \infty$, the projections of the eigenfunctions onto an arbitrary vector in Hilbert space have a Gaussian distribution centered at zero. This gives the PT distribution.

The distribution of the eigenvalue spacings, $P(s)$, was obtained by Wigner by studying the simplest case of a matrix with dimensions $N = 2$ [5]. The nearest neighbor spacing distribution (NNS) depends on ratio of the actual level spacing, D, and the mean level spacing $\overline{D}$ (The result is also known as the Wigner surmise):

$$P(s) = \frac{\pi s}{2}e^{-\pi s^2/2}, \tag{2.23}$$

where $x = D/\overline{D}$.

In the GOE, the mean level density is defined as $\rho(E) = \overline{\sum_i (E - E_i)}$, and for $N \to \infty$, it is given by

$$\rho(E) = \frac{N}{\pi\lambda}\sqrt{1 - \left(\frac{E}{2\lambda^2}\right)}. \tag{2.24}$$

This equation is usually referred to as Wigner's "semicircle law". The mean level spacing, $D(E) = \rho^{-1}(E)$ tends to zero as N goes to infinity. This shows that the statistical theory is suitable to describe the local properties of levels, but is not suitable to describe the global behavior (see explanations in [8,9]).

Global Properties of Resonances

The simplest way to determine the average level spacing is to count the neutron resonances. The average level spacing is defined by the number of resonances, N, with the same spin and parity, J^π, in an energy interval ΔE:

$$< D_{lJ} >= \frac{\Delta E}{N-1}. \tag{2.25}$$

In practice, the average level spacing is usually determined by the reciprocals of the slope of the staircase plot (see Fig. 4.9 in Chapter 4).

Another important parameter, the neutron strength function, was introduced from the optical model of nuclear reactions:

$$S_l = \frac{< g\Gamma_n^l >}{(2l+1)D_l} = \frac{1}{(2l+1)\Delta E}\sum_j g_j \Gamma_{nj}^l, \tag{2.26}$$

where g_j is the spin statistical weight factor for angular momentum J and Γ_{nj}^l is the reduced neutron width given by

$$\Gamma_{nj}^l = \sqrt{\frac{1}{E_0}}\frac{\Gamma_{nj}}{V_l}, \tag{2.27}$$

where V_l is the penetration factor (e.g., see [10]). For s-wave resonances, the penetration factor is equal to 1. The error on the strength function is estimated to be $\sqrt{2/N}S_0$, based on the PT distribution of the widths.

Feshbach, Porter and Weisskopf [11] calculated S_0 with the optical model and predicted the maxima of the s-wave strength function at about mass number $A \approx$11, 52, 144 and 305. These broad resonances are associated with the nodes of the continuum single particle wave function corresponding to n = 3 ($A \approx 52$) and 4 ($A \approx 144$), respectively. Improved optical potential calculations give reasonable agreement with experimental values [10].

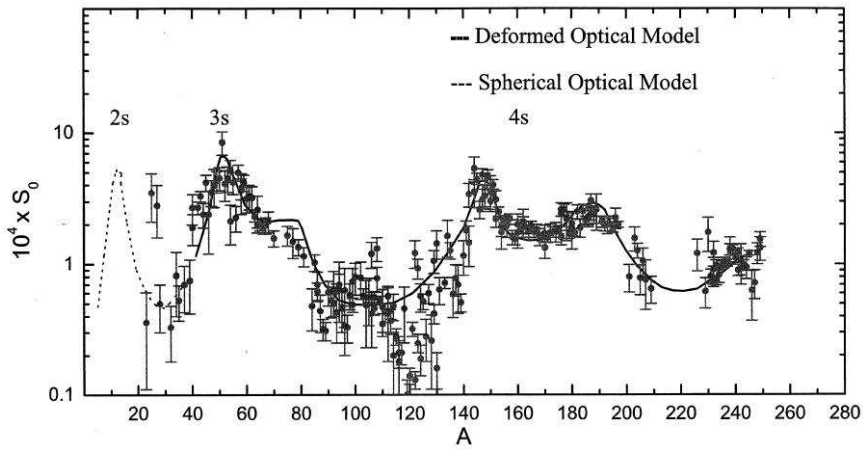

Figure 2.2: Theoretical and experimental values of the s-wave strength function. Solid and dotted curve represents deformed and spherical optical model calculation. The figure is taken from [10].

However, a comparison of theoretical and experimental values for both s- and p-wave strength functions indicate a lack of detailed agreement in certain mass regions, especially the region between the $3s$ and $4s$ giant resonances for S_0 in Fig. 2.2. Possible explanations for this behavior include an additional isospin-dependent term in the optical model calculations.

2.3 Statistical Models of Nuclear Reactions

Statistical approaches in nuclear physics started from Bohr's statement of the independence hypothesis in 1936 [12]. He assumed that a nuclear reaction occurs in two independent stages: that is, formation of the compound nucleus and disintegration into reaction products. His idea was motivated by the discovery by Fermi of many narrow resonances in light nuclei [13]. The lifetime of these resonances is of the order of 10^{-16} sec. On the other hand, one can estimate the characteristic nuclear time to be equal to 10^{-22} sec. These relatively long lived quasi-stationary states arose because of the excitation energy of the compound nucleus is distributed over numerous degree of freedom. Therefore, it takes a very long time for energy to concentrate in one nucleon. The Weisskopf theory is the earliest statistical theory of compound nuclear decay, which can be explained essentially using classical statistical and geometrical arguments [14]. The same is not true of the much used Hauser-Feshbach (HF) theory [15, 16], which relies on quantum mechanical transmission

coefficients.

2.3.1 Hauser Feshbach Theory

According to Bohr's hypothesis, the compound reaction cross-section is factored into the cross-section for fusion from the entrance channel α, σ_α, and the probability P_β for the decay of the compound nucleus to channel β:

$$\sigma_{\alpha\beta} = \sigma_\alpha P_\beta. \tag{2.28}$$

The principle of detailed balance (a consequence of the time reversal invariance of the Hamiltonian) relates the cross-section to its inverse:

$$k_\alpha^2 \sigma_{\alpha\beta} = k_\beta^2 \sigma_{\beta\alpha}. \tag{2.29}$$

One obtains the cross-section for the time-reversed reaction $\beta \rightarrow \alpha$ by interchanging the indexes α and β in Eq. (2.28). Substituting both expressions in the detailed-balance relation (2.29), we find

$$\frac{k_\alpha^2 \sigma_\alpha}{P_\alpha} = \frac{k_\beta^2 \sigma_\beta}{P_\beta}. \tag{2.30}$$

The left-hand side of this equation depends only on channel α, and the right-hand side only on channel β. Since α and β are arbitrary channels, both sides must be equal to a channel-independent quantity, which we call ξ. Then we find that the probability for the decay of the compound nucleus to a channel β is given by

$$P_\beta = \frac{k_\beta^2 \sigma_\beta}{\xi}. \tag{2.31}$$

The decay probabilities must satisfy $\sum_\beta P_\beta = 1$ and this equation yields

$$\xi = \sum_\beta k_\beta^2 \sigma_\beta. \tag{2.32}$$

Thus, we obtain the compound reaction cross-section that is exclusively determined by the partial fusion cross-sections in all channels:

$$\sigma_{\alpha\beta} = k_\beta^2 \frac{\sigma_\alpha \sigma_\beta}{\sum_\gamma k_\gamma^2 \sigma_\gamma}. \tag{2.33}$$

Fusion

Fusion is, by definition, the process by which a compound nucleus composed of the sum of projectile and target nucleons is formed. The fusion cross-section is equal to the total compound reaction cross-section, i.e., it is given by the compound reaction cross-section (Eq. 2.33) summed over all final channels

$$\sigma_\alpha = \sum_\beta \sigma_{\alpha\beta}. \tag{2.34}$$

First we note that the partial reaction cross-section for a given channel and angular momentum can be expressed in terms of the collision matrix element (Eq. 2.3). Recalling the unitary property of the collision matrix, we can write reaction and elastic scattering cross-sections as

$$\sigma_{\alpha\beta} = \frac{\pi}{k_\alpha^2}(2l+1)\left[1 - |U_{\alpha\alpha}|^2\right], \tag{2.35}$$

and

$$\sigma_{\alpha\alpha} = \frac{\pi}{k_\alpha^2}(2l+1)\left|1 - U_{\alpha\alpha}\right|^2. \tag{2.36}$$

Note that Eq. (2.35) refers to the reaction and not to the absorption cross-section. The absorption cross-section is the sum of the average reaction cross-section and a fluctuating term (*compound-elastic scattering*) of the average elastic scattering

$$\sigma_\alpha = \frac{\pi}{k_\alpha^2}(2l+1)\left[1 - |\overline{U_{\alpha\alpha}}|^2\right]. \tag{2.37}$$

We introduce the (optical) transmission coefficient

$$T_\alpha = 1 - |\overline{U_{\alpha\alpha}}|^2, \tag{2.38}$$

and have

$$\sigma_\alpha = \frac{\pi}{k_\alpha^2}(2l+1)T_\alpha. \tag{2.39}$$

We may rewrite the compound reaction cross-section by substituting Eq. (2.39) into Eq. (2.33)

$$\sigma_{\alpha\beta} = \frac{\pi}{k_\alpha^2}(2l+1)\frac{T_\alpha(\varepsilon_\alpha)T_\beta(\varepsilon_\beta)}{\sum_\gamma T_\gamma(\varepsilon_\gamma)}. \tag{2.40}$$

This is the *Hauser-Feshbach formula* [15] that expresses the compound reaction cross-section purely in terms of transmission coefficients. The spin weight factor needs to

be included, if the particles have a spin. The probability that a given channel spin s is formed from projectile i and target I spin is

$$P(s) = \frac{2s+1}{(2i+1)(2I+1)},$$

and similarly the probability of s combining with l to give J is

$$P(s) = \frac{2J+1}{(2s+1)(2l+1)}.$$

Multiplying the probabilities by $(2l+1)$ weighting gives the cross section including the statistical factor

$$\sigma_{\alpha\beta} = \frac{\pi}{k_\alpha^2} \sum_{J,\pi} \frac{(2J+1)}{(2I+1)(2i+1)} \frac{T_\alpha(\varepsilon_\alpha) T_\beta(\varepsilon_\beta)}{\sum_\gamma T_\gamma(\varepsilon_\gamma)}. \tag{2.41}$$

Equations such as (2.41) apply to (charged or uncharged) particle emission reactions. For the neutron capture reactions, the T_α may be calculated with the optical model and the γ-ray transmission coefficients must be replaced by $T(E_\gamma) = E_\gamma^{2l+1} f^{XL}(E_\gamma)$. The expression for the compound reaction cross-section contains two important quantities: the photon-strength function, $f^{XL}(E_\gamma)$, and the level density $\rho(E, J)$, which we shall discuss in the following sections.

2.3.2 Level Density

The level density (LD) of the nucleus is defined as the number of nuclear states per unit energy. In order to calculate the level density one must, strictly speaking, determine all eigenvalues (and their degeneracy) of the nuclear Hamiltonian H_A and count how many of these fall into the energy interval $\varepsilon_A + d\varepsilon_A$. This can be done only in very simple models, as for example the independent-particle model. Even then, the explicit calculation of levels is onerous, and one usually takes recourse to more indirect methods.

In practice, there are two common methods to determine the level density experimentally. At low excitation energy the number of levels is limited and the individual levels of the nucleus well separated. At this energy region, one may determine LDs by directly counting the observed excited states, but this procedure is limited by the accuracy and completeness of the available data. With increasing excitation energy, the number of levels increases, the spacing of the levels becomes smaller than the experimental resolution,

and the nature of the excitation becomes very complicated. Therefore, at high excitation energies a statistical procedure is employed to describe the level density as we discussed in Sec. 2.2.2. Most of the existing experimental data are based on measuring LDs at an energy close to the neutron binding energy by counting the number of neutron resonances observed in low-energy neutron reactions.

The Level Density in the Fermi Gas Model

Bethe initiated theoretical modeling of level densities with his landmark papers in 1936 and 1937 [17, 18]. Bethe's Constant Temperature Formula (CTF) was based on a Fermi Gas Model (FGM) of the nucleus. In the Fermi gas model the nucleus is regarded as an ideal gas of A fermions enclosed in the fixed nuclear volume.

The most convenient way of describing the thermodynamics of the ideal Fermi gas is to introduce the notion of the *grand-canonical ensemble*, where the system is assumed to have a fixed temperature T and a fixed chemical potential μ. The many particle state i with energy E_i and particle number N_i are distributed according to

$$w_i = w_i(\mu, \beta) = \frac{1}{Z(\mu, \beta)} e^{-\beta(E_i - \mu N_i)}, \tag{2.42}$$

where $Z(\mu, \beta)$ is the *grand partition sum* over all states i of the system:

$$Z(\mu, \beta) = \sum_i e^{-\beta(E_i - \mu N_i)}, \tag{2.43}$$

where $\beta = 1/k_B T$ is the inverse temperature, and k_B is the Boltzmann constant.

The procedure for calculating the level density is to derive expressions for the average particle number in the grand-canonical ensemble:

$$\overline{N(\mu, \beta)} = \sum_i w_i N_i = A, \tag{2.44}$$

and for the average energy

$$\overline{E(\mu, \beta)} = \sum_i w_i E_i = E, \tag{2.45}$$

which are functions of the parameters μ and β. These average quantities are then set equal to the actual number of fermions A and the actual energy of the system E.

By inverting these relations one obtains the chemical potential, μ, and the temperature, β, as function of A and E. One then calculates the entropy $S = S(\mu, \beta) = S(A, E)$

with the help of the thermodynamic relation

$$S(A,E) = \int_{E_0}^{E} \frac{dE'}{T(A,E')}, \tag{2.46}$$

where E_0 is the energy of the ground state of the system. The density of states $\rho(A,E)$ for given particle number A and total energy E in terms of the entropy $S(A,E)$ is finally obtained with the help of the fundamental relation

$$\rho(A,E) = \rho(A,E_0)e^{S(A,E)/k_B}. \tag{2.47}$$

Following a similar procedure for a gas of independent fermions, we can derive analytic expressions for the functions $A = A(\mu,\beta)$ and $E = E(\mu,\beta)$. The expression for the ground state ($T = 0$) is

$$A = \frac{16\pi}{3}\frac{(2m\epsilon_F)^{3/2}}{(2\pi\hbar)^3}V, \tag{2.48}$$

where m is the nucleon mass, ϵ_F is the Fermi energy, that is the value of the chemical potential for the ground state of the system.

Considering the nuclear volume, $V = (4\pi/3)R^3$ with $R = r_0A^{1/3}$, the Fermi energy is determined as

$$\epsilon_F = \frac{(9\pi)^{2/3}}{2mc^2}\left[\frac{\hbar c}{2r_0}\right]^2. \tag{2.49}$$

The ground state energy of the system is

$$E_0 = \frac{3}{5}\epsilon_F A. \tag{2.50}$$

Calculation of the average energy at finite temperature ($T > 0$) is given in the low temperature approximation as

$$E = E_0 + g(\epsilon_F)\frac{\pi^2}{6\beta^2}. \tag{2.51}$$

and the excitation energy $E^* = E - E_0$ becomes, with $\beta = 1/k_BT$,

$$E^* = a[k_BT]^2. \tag{2.52}$$

Here we have introduced the *level density parameter*

$$a = \frac{\pi^2}{6}g(\epsilon_F), \tag{2.53}$$

where $g(\epsilon_F)$ is the single-particle density of the states at Fermi energy.

The single-particle states of fermions with momentum p in the interval $(p,\, p+dp)$ and volume V is

$$g(p)dp = 4\frac{V}{(2\pi\hbar)^3}4\pi p^2 dp, \tag{2.54}$$

where the factor 4 has been introduced to take-account of spin-isospin degeneracy. In terms of the single-particle energy $\epsilon(p) = p^2/2m$, this takes the form

$$g(\epsilon)d\epsilon = 4\frac{V4\pi\sqrt{2}m^{3/2}}{(2\pi\hbar)^3}\epsilon^{1/2}d\epsilon. \tag{2.55}$$

With the help of Eq. (2.48) the density of states can now be written

$$g(\epsilon) = \frac{3}{2}\frac{A}{\epsilon_F^{3/2}}\epsilon^{1/2}. \tag{2.56}$$

Substituting in Eq. (2.49) the nucleon mass $mc^2 = 940$ MeV and the nuclear radius parameter $r_0 = 1.1$ fm, we find the Fermi energy in nuclei $\epsilon_F \approx 40$ MeV. The value of the level density parameter is then obtained from Eqs. (2.53) and (2.56) as

$$a \approx \frac{A}{16}\ \mathrm{MeV}^{-1}. \tag{2.57}$$

This value is about a factor of two small compared to the empirical value of $a \approx A/8$ (see Fig. 2.3), because the single-particle level density at the Fermi energy is smaller for a Fermi gas in a spherical box than for a realistic nucleus, in which the well widens towards the top.

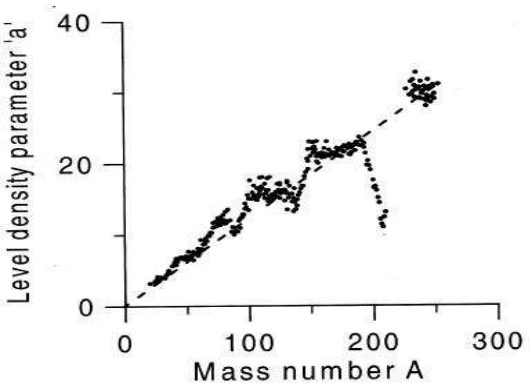

Figure 2.3: Empirical values of the LD parameters, a, obtained by counting neutron resonances and fitting the formula $\ln\rho = 2\sqrt{aE^*}$. The straight line $a = A/8$ reproduces the average trend of the empirical values of a.

The Bethe Formula

The change of entropy for constant volume V and particle number A is connected with the change of energy by the relation

$$dS = \frac{dE}{T}. \tag{2.58}$$

According to the inverse of Eq. (2.52)

$$S = \int_{E_0}^{E} \frac{dE'}{T} = k_B \int_0^{E*} dE^{*\prime} \sqrt{\frac{a}{E^{*\prime}}} = 2k_B\sqrt{aE^*}. \tag{2.59}$$

Introducing the new notation $\rho(A, E) = \rho_A(E^*)$, we now employ the relation 2.47 and find for the level density

$$\rho_A(E^*) = \rho_A(0)e^{2\sqrt{aE^*}}. \tag{2.60}$$

This is the Bethe formula, in which the level density depends exponentially on the excitation energy E^*. The dependence on the nucleon number A is mainly contained in the level density parameter a. Figure 2.3 displays the value of the parameter a. The average trend of the LD parameter is well fit by a straight line.

Strong deviations from the overall trend ($a = A/8$) are mainly due to shell effects, which are not included in this simple model. Other corrections are due to pairing effects and "bulk" nuclear matter estimates of the single particle spacing also have a large effect. In order to account for these effects, several phenomenological extensions and modifications of the Fermi gas model have been proposed, to which pairing and shell effects are added semi-empirically. One of the earliest corrections to the FGM was by Newton [19]. In his modification the odd-even effects were included by means of a pairing energy shift and this was called the Back-Shifted Fermi Gas model (BSFG). Gilbert and Cameron expanded on Newton's model [20] combining the BSFG formula at high excitation energies with the CTF for lower energies. Other modified forms of the LD formula were reported in [21–23]; also note a review by Iljinov on this topic [24].

However, we often need LDs for many unstable nuclei, for which they cannot be determined experimentally. For such nuclei, physical understanding of the parameters is limited, and therefore the extrapolation to nuclei far from the stability line is still rather problematic. New theories may provide an accurate description of an improved physical understanding of the relevant level density parameters. There has been remarkable progress

made in theoretical approaches at a microscopic level, such as taking into account shell effects, pairing correlations, and collective effects [25, 26], but their use in practical applications is rather complicated. A recent calculation method based on Shell Model Monte Carlo (SMMC) [27–29] techniques makes predictions for level densities, and the results appear promising. Showing that these calculations can correctly describe existing data would provide increased confidence for level density predictions far from stability.

A Practical Level Density Formula

We used the DICEBOX code [30] for simulation of the radiative decay of the compound nucleus. The current version of the code offers two options for the LD formula [31]; the Constant-Temperature Formula, and the Back Shifted Fermi Gas formula (and its modification with a polynomial). The CTF has the form

$$\rho(E,J) = f_J \frac{1}{T} e^{\frac{(E-E_0)}{T}}, \tag{2.61}$$

where the free parameters T and E_0 are, respectively nuclear temperature and the back-shift.

The second formula reads

$$\rho(E,J) = f_J \frac{\exp\left(2\sqrt{a(E-E_1)}\right)}{12\sqrt{2}\sigma a^{1/4}(E-E_1)^{5/4}}, \tag{2.62}$$

where σ is a spin cut-off parameter, a is the conventional shell-model LD parameter, and E_1 is a back shift related to the pairing energy. The spin factor f_J in above equations represents the probability that a randomly chosen level has a spin J [20]

$$f_J = \frac{2J+1}{2\sigma^2} e^{\frac{-(J+1/2)^2}{2\sigma^2}}. \tag{2.63}$$

For the CTF, a semi-empirical prescription of the σ is used [32]:

$$\sigma = 0.98 A^{0.29}, \tag{2.64}$$

where A is the mass number.

For the BSFG formula, the spin cut-off factor is assumed to be

$$\sigma = 0.2980 A^{1/3} a^{1/4} (E-E_1)^{1/4}. \tag{2.65}$$

T, E_0, E_1, a are the input parameters of the code that are determined from experimental data. It is to be stressed that both expressions (2.61 and 2.62) describe level

density with a specified spin and not specified parity. Therefore, to obtain the level density for a fixed spin J and a fixed parity π the right-hand side of these equations are reduced by factor of 2.

2.3.3 Gamma-Ray Transitions

The γ-ray emission channel is considered a universal channel, since γ ray emission is always energetically allowed.

Going back to the compound nuclear reaction cross section formula (2.28), the probability P_β for the decay of the compound nucleus to the γ-ray emission channel is described as resulting from the interaction of the nucleus with an external electromagnetic field. The complete field consists of the electric field E and magnetic field B. The nucleus and the electromagnetic field interact weakly, so that the interaction can be treated as a perturbation. The unperturbed initial state of the system is the excited nuclear state and the electromagnetic field in its ground state, i.e., no photons. The final state is the nuclear ground state and the electromagnetic field with one photon. The transition probability from an initial state ξ_i to a final state ξ_f, calculated by the "golden rule" of time-dependent perturbation theory, is

$$P_{fi}^{(XL)}(E_\gamma) = \frac{8\pi}{\hbar}\frac{(L+1)}{L[(2L+1)!!]^2}\left(\frac{E_\gamma}{\hbar c}\right)^{2L+1} B(XL;\xi_i, J_i \to \xi_f, J_f), \tag{2.66}$$

where the *reduced transition probability* is

$$B(XL;\xi_i, J_i \to \xi_f, J_f) \equiv \frac{1}{2J_i+1}|<\xi_i J_i||H_{XL}||\xi_f J_f>|^2. \tag{2.67}$$

The units of the reduced transition probabilities for the electric and magnetic components are respectively

$$[B(EL)] = e^2 f m^{2L}, \qquad [B(ML)] = \mu_N^2 f m^{2L-2}.$$

The transition probabilities (Eq. 2.66) may be given in useful numerical forms as:

$$\begin{aligned} P_{fi}^{(EL)}(E_\gamma) &= 2.786\times 10^{20} k(L) E_\gamma^{2L+1} B(EL), \\ P_{fi}^{(ML)}(E_\gamma) &= 3.081\times 10^{18} k(L) E_\gamma^{2L+1} B(ML), \\ k(L) &\equiv \frac{L+1}{L[(2L+1)!!]^2}. \end{aligned} \tag{2.68}$$

Selection Rules for Radiative Transitions

In a transition, the emitted particle carries away angular momentum L, which for the photon must be at least 1, since it is a vector particle. The first selection rule is that there are no $E0$ or $M0$ gamma transitions. However, electromagnetic $E0$ transitions are possible via internal conversion, where the nucleus de-excites by ejecting an atomic electron. The absence of all $M0$ transitions results fundamentally from the absence of magnetic monopoles in nature. Since the total angular momentum must be conserved during the transition, we have

$$\mathbf{J_i} = \mathbf{J_f} + \mathbf{L}, \tag{2.69}$$

where $||\mathbf{L}|| = \hbar\sqrt{L(L+1)}$ and the corresponding quantum numbers must satisfy $|J_f - J_i| \leq L \leq |J_f + J_i|$. Denoting the parity of the initial state by π_i and that of the final state by π_f, we then have the parity conservation selection rule

$$\pi_i\pi_f = \begin{cases} (-1)^L & \text{for } EL, \\ (-1)^{L-1} & \text{for } ML. \end{cases} \tag{2.70}$$

These considerations generate different sets of transitions rules depending on the multipole order and type, as presented in table 2.1.

Table 2.1: Lowest multipolarities for gamma transitions.

$\Delta J = \lvert J_f - J_i \rvert$	0^a	1	2	3	4
$\pi_i\pi_f = -1$	E1	E1	M2	E3	M4
$\pi_i\pi_f = 1$	M1	M1	E2	M3	E4

^{a} not $0 \rightarrow 0$

Single-Particle Matrix Elements

Weisskopf first estimated the *reduced transition probability* [33], assuming a single proton moving independently within a nuclear square well potential. It is not surprising that the extreme single-particle model does not yield good values for γ-transition probabilities. However, the simple formulas are often used as reference values for comparing experimental data. For electric transitions we have the so-called *Weisskopf single-particle estimate* or *Weisskopf unit* (W.u.)

$$B_W(EL) = \frac{(1.2)^{2L}}{4\pi}\left(\frac{3}{L+3}\right)^2 A^{2L/3} e^2 f m^{2L}, \tag{2.71}$$

and for magnetic transitions

$$B_W(ML) = \frac{10}{\pi}(1.2)^{2L-2}\left(\frac{3}{L+3}\right)^2 A^{(2L-2)/3}\mu_N^2 fm^{2L-2}. \tag{2.72}$$

By substituting the above relations for $B(EL)$ and $B(ML)$ in (2.68) we get Weisskopf estimates for transition probabilities per unit time. Tables 2.2 list the relevant numerical expressions.

Table 2.2: Radiative Transition Probabilities.

Electric Transitions

XL	$B_W(EL)$, (e^2fm^{2L})	$P_W(EL)$, (sec^{-1})
E1	$6.446 \times 10^{-2}A^{2/3}$	$1.023 \times 10^{14}E^3A^{2/3}$
E2	$5.940 \times 10^{-2}A^{4/3}$	$7.265 \times 10^{7}E^5A^{4/3}$
E3	$5.940 \times 10^{-2}A^{2}$	$3.385 \times 10^{1}E^7A^{2}$

Magnetic Transitions

XL	$B_W(EL)$, (e^2fm^{2L})	$P_W(ML)$, (sec^{-1})
M1	1.790	$3.184 \times 10^{13}E^3$
M2	$1.650A^{2/3}$	$2.262 \times 10^{7}E^5A^{2/3}$
M3	$1.650A^{4/3}$	$1.054 \times 10^{1}E^7A^{4/3}$

The transition energies E are to be given in MeV

As a consequence of these simple model calculations, we may conclude that the transition probability decreases drastically with increasing multipolarity. Therefore the likeliest transition is the one of the lowest multipolarity allowed by the angular momentum and parity selection rules. For the same multipole, electric transitions are strongly favored over magnetic.

An exact theoretical calculation of the transition probability is impossible because the wave functions describing the state are unknown. Moreover, highly excited states are involved in the neutron capture process whose excitation energy is $E^* = E_n + B_n$, where B_n is a neutron separation energy and E_n is the kinetic energy of the neutron. The wave function of the compound system will be a complicated superposition of many states. However, the transition matrices involving highly excited states may be estimated based on certain models.

2.3.4 Models for Photon Strength Functions

Recall that the P_{fi} denotes a probability per unit time for a gamma transition from an initial nuclear state i to a final nuclear state f. The lifetime of the transition is $1/P_{fi}$ and the Heisenberg uncertainty principle relates the transition probability with the partial γ-ray radiation width as

$$\Gamma_{fi} = \hbar P_{fi}.$$

The photon strength function for γ-ray emission of multipole type XL is defined via the average partial radiation width for transitions from initial state i with energy E_i, spin J_i and parity π_i to a final level f as

$$\overline{\Gamma}^{(XL)}(E_i, J_i, \pi_i \rightarrow E_f) = \frac{f^{XL} E_\gamma^{2L+1}}{\rho(E_i, J_i, \pi_i)}. \tag{2.73}$$

where $f_{XL}(E_\gamma)$ is a photon-strength function (PSF) which is considered a slowly varying function of the energies E_i and E_f compared to the extremely rapid (exponential) variation of the level density and $\rho(E_i, J_i, \pi_i)$ is the level density at the initial state i.

The γ-ray transmission coefficients in the Hauser-Feshbach statistical model calculation for multipolarity L of type X (where $X = M$ or E) are given by

$$T_{XL}(E_\gamma) = 2\pi f_{XL}(E_\gamma) E_\gamma^{2L+1} \tag{2.74}$$

In most cases, it may be assumed that only $E1$, $M1$ and $E2$ multipolarities contribute in radiative capture reaction. Therefore, we discuss only those specific transitions in detail. In the single particle model, the f_{XL} is assumed to be constant. Rough estimates of the $E1$, $M1$ and $E2$ partial radiation widths are given by Blatt-Weisskopf [34] as

$$f_{sp}^{E1} = k^{E1} \frac{A^{2/3}}{D_0}, \tag{2.75}$$

$$f_{sp}^{M1} = k^{M1} \frac{1}{D_0}, \tag{2.76}$$

and

$$f_{sp}^{E2} = k^{E2} \frac{A^{4/3}}{D_0}, \tag{2.77}$$

where D_0 is the spacing of single particle states which is about 0.5-1.0 MeV [10]. Based on the available thermal and resonance neutron capture data Bartholomew [35] showed that

the theoretical f^{E1} and f^{M1} values agree with the experimental values with $D_0 = 15$ MeV. This is much larger than the single particle spacing which reflects the overestimate of the Weisskopf single particle values [10]. Experimental estimates and surveys of the single-particle PSFs are given in the work of Axel [36], Carpenter [37], McCullagh, Stelts and Chrien [38] and Kopecky and Uhl [39, 40]. The recommended systematics of the strengths in these works yields $f^{E1} = 9.23 \times 10^{-11} A^{1.43\pm0.14}$ and $f^{M1} = 1.58 \times 10^{-9} A^{0.47\pm0.21}$ for γ-ray energies near 6 to 7 MeV [39]. The scatter of the data around the average value is rather large, by a factor of 2 or 3 for $E1$ ($M1$) radiation [31]. It is believed that these uncertainties originate from residual Porter-Thomas fluctuations. As more data became available, it became evident that the single-particle model could not estimate the values of total radiation widths and that a more realistic model was needed.

Brink-Axel Model of the E1 radiation

The inverse process of the neutron capture reaction is the photo-nuclear reaction; the time reversal invariance of the nuclear reaction allows an alternative approach to study the electric dipole radiative strength function. The experiments observed a giant electric dipole resonance (GEDR) in photo-nuclear reactions. A large amount of experimental data showed that the Lorentz shape gave a reasonably good approximation to the GDR:

$$\sigma_{abs}(E) = \frac{\sigma_0 E^2 \Gamma_G^2}{(E^2 - E_G^2)^2 + E^2 \Gamma_G^2}, \tag{2.78}$$

where σ_0, Γ_G and E_G are respectively the peak cross section, full width at half maximum (FWHM) and peak position of the GDR.

Brink [41] hypothesized that the formation of the GDR does not depend on the properties of the nuclear state (excitation energy, spin and parity). This implies that the photo-absorption cross section depends only on the photon energy $E_\gamma = E_f - E_i$. Based on the detailed-balance principle and Brink's hypothesis, Axel [36] formulated the γ-ray strength function as

$$f^{(E1)}(E_\gamma) = \frac{1}{3(\pi\hbar c)^2} \frac{\sigma_0 E_\gamma \Gamma_G^2}{(E_\gamma^2 - E_G^2)^2 + E_\gamma^2 \Gamma_G^2}. \tag{2.79}$$

The existence of the GEDR is explained as collective dipole vibrations of proton and neutron fluids in the nucleus. It is assumed that two classical modes of the collective motion exist; The first mode of the GEDR is a vibration of proton vs. neutron fluids within a fixed nuclear surface [42] and the second mode assumes vibration of two incompressible

spheres corresponding to protons and neutrons [43]. Since the position of the GEDR is approximated by $E_G = 31.2A^{-1/3} + 20.6A^{-1/6}$, where the $A^{-1/6}$ and $A^{-1/3}$ terms correspond to each mode of vibration, the real GEDR is a mixture of these two modes [44]. Equation (2.79) describes the PSF for spherical nuclei. For deformed nuclei, the GEDR splits into two (or three) modes of vibration corresponding to oscillations along the symmetry axis and those perpendicular to it. Therefore, the PSF of deformed nuclei is represented by the superposition of two Lorentzian with different sets of parameters.

The Lorentzian shape of the E1 strength function gives a reasonable agreement with photo-absorption data in medium-weight and heavy nuclei. The parameters of the Lorentz curve are usually obtained from fitting (γ,n) data near the maximum of the resonance. Obviously, the (γ,n) data gives information above the neutron separation energy and the behavior of the PSF below the particle separation energy is an open question. A great deal of information on the $E1$ strength function below the neutron separation energy has been accumulated from various experiments. It became evident that simple Lorentzian shape of the GEDR may be inadequate at energies close to the neutron binding energy [45]. However, the standard Lorentzian model significantly underestimates the γ-decay spectra at low energies, $E_\gamma \leq$ 1-2 MeV [46]. For these reasons, some extension of the model was required.

The Fermi Liquid model of the E1 radiation

The first model for the low-energy approximation of the $E1$ strength was developed by Kadmenskii, Markushev and Furman (KMF) [47]. According to the Fermi Liquid Model (FLM) for a nucleus which is characterized by strongly interacting quasi-particles, the $E1$ PSF for spherical nuclei is given by [47]

$$f^{(E1)}_{KMF}(E_\gamma, T) = \frac{1}{3(\pi\hbar c)^2} F_K \frac{\sigma_0 E_G \Gamma_G \Gamma(E_\gamma, T)}{(E_\gamma^2 - E_G^2)^2}, \tag{2.80}$$

where the quantity F_K is determined by the Landau parameter F_0' and F_1' as

$$F_K = \frac{(1 + 2F_1'/3)^{1/2}}{(1 + 2F_0')^{1/2}}.$$

The value $F_K = 0.7$ is adopted in the KMF model. The temperature T and energy dependence of the GEDR damping width is given by

$$\Gamma(E_\gamma, T) = \Gamma_G \frac{E_\gamma^2 + 4\pi^2 T^2}{E_G^2}, \qquad T = \sqrt{\frac{E_x - \Delta}{a}}. \tag{2.81}$$

Here T is the temperature of the final level for the γ decay at excitation energy E_x, Δ is a pairing energy and a is the level density parameter.

The predictions of the KMF model give reasonable agreement with the experimental strength of $E1$ transitions to the low energy levels [30]. Since Eq. (2.80) diverges at $E_\gamma = E_G$, the KMF model cannot describe data near maximum of the GEDR.

Other Phenomenological Models of the PSF

In order to describe adequately the γ-ray strength functions for both spherical and deformed nuclei, several phenomenological models have been introduced such as the Enhanced Generalized Lorentzian (EGLO) [40,48] and the Generalized Fermi-Liquid (GFL) [49].

The Generalized Lorentzian (GLO) model consists of two terms: (i) a Lorentzian with energy and temperature dependent width according to Eq. (2.81) and (ii) the (non-zero) $E_\gamma \to 0$ limit of the KMF model

$$f_{GLO}^{(E1)}(E_\gamma) = 8.68 \times 10^{-8} \sigma_G \Gamma_G \left[E_\gamma \frac{\Gamma(E_\gamma, T)}{(E_\gamma^2 - E_G^2)^2 + E_\gamma^2 \Gamma(E_\gamma, T)} + 0.7 \frac{\Gamma(E_\gamma = 0, T)}{E_G^2} \right]. \quad (2.82)$$

The GLO model provides for some spherical nuclei a good description of average resonance capture (ARC) data, capture cross sections and γ-ray production spectra [50]. For spherical and transitional nuclei, the KMF model provides a reasonable description of experimental data, but for deformed nuclei the BA model seems to yield more acceptable agreement [31]. In order to reproduce data for deformed nuclei an *empirical* modification of the damping width was proposed [51] as

$$\Gamma_{en}(E_\gamma, T) = \left[k_0 + \frac{E_\gamma - \epsilon_0}{E_G - \epsilon_0}(1 - k_0) \right] \frac{\Gamma_G}{E_G^2}(E_\gamma^2 + 4\pi^2 T^2), \quad (2.83)$$

which is determined by two parameters k_0 and ϵ_0.

The damping width (Eq. 2.81) was replaced by Eq.(2.83) in the EGLO model. The value of the *enhancement* factor k_0 is chosen by reproducing the experimental $E1$ strength around the reference energy ϵ_0 which is recommended to be $\epsilon_0 \approx 4.5$ MeV [40]. Note, that $k_0 = 1$ yields the GLO model. The recommended systematics of the parameter k_0 as a function of mass number A depends strongly on the level density model adopted [40]. Namely, for BSFG level density this is

$$k_0 = \begin{cases} 1.0 & \text{for } A < 148 \\ 1.0 + 0.09(A - 148)^2 \exp\left[-0.18(A - 148)\right] & \text{for } A \geq 148, \end{cases} \quad (2.84)$$

while for the level density model proposed by Katarina, Ramamurthy and Kapoor [23], which is close to the CTF, k_0 has the form

$$k_0 = \begin{cases} 1.5 & \text{for } A < 145 \\ 1.5 + 0.131(A-145)^2 \exp\left[-0.154(A-148)\right] & \text{for } A \geq 145. \end{cases} \tag{2.85}$$

Chapter 3

Experimental Techniques and Data Processing

The neutron capture experiments on ^{155}Gd, ^{156}Gd and ^{158}Gd isotopes were carried out by the time-of-flight method at the 20.3-meter flight path of the Los Alamos Neutron Science Center (LANSCE) at the Los Alamos National Laboratory. The linear accelerator delivers two proton beams at 800 MeV: an H^+ and an H^- beam. After acceleration the H^+ and H^- beams are separated. The H^- beam is injected into a Proton Storage Ring for accumulation and delivery to the neutron scattering center or to the weapons neutron research center. The 100-μA current proton beam hits the tungsten target with a 20-Hz repetition rate and neutrons are produced via the spallation process. The DANCE detector is located on Flight Path 14 at the Manuel Lujan Jr. Neutron Scattering Center, which is designed to view only the uncoupled water moderator and not the tungsten target itself.

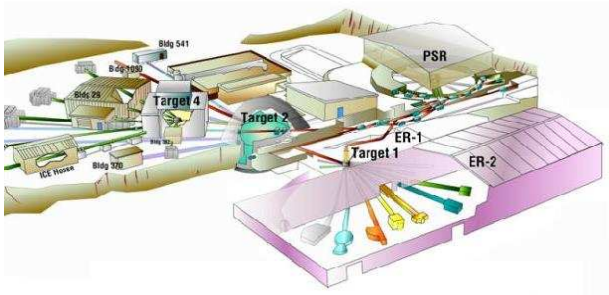

Figure 3.1: Los Alamos Neutron Science Center.

The gadolinium targets were prepared at the Oak Ridge National Laboratory as self-supporting metal foils. The thicknesses of the foils are 1.008 mg/cm^2, 10.272 mg/cm^2 and 9.30 mg/cm^2 for the ^{155}Gd, ^{156}Gd and ^{158}Gd targets, respectively. The isotopic composition of the targets is listed in table 3.1.

Table 3.1: Isotopic composition of the targets. The amount of isotope is listed as the percentage of the target material.

	Isotopic Abundance, Percent						
target	^{152}Gd	^{154}Gd	^{155}Gd	^{156}Gd	^{157}Gd	^{158}Gd	^{160}Gd
(nat.ab.)	(0.20%)	(2.18%)	(14.80%)	(20.47%)	(15.65%)	(24.85%)	(21.86%)
^{155}Gd	0.03	0.63	**91.74**	5.12	1.14	0.94	0.40
^{156}Gd	< 0.01	0.11	1.96	**93.79**	2.53	1.20	0.41
^{158}Gd	< 0.1	< 0.1	0.96	1.70	3.53	**92.0**	1.82

3.1 DANCE Detector

The DANCE (Detector for Advanced Neutron Capture Experiments) array is designed to measure prompt γ-rays following neutron capture on small and/or radioactive samples. The maximum rate limit for radioactive targets is about 1 detected event per 30 nanoseconds.

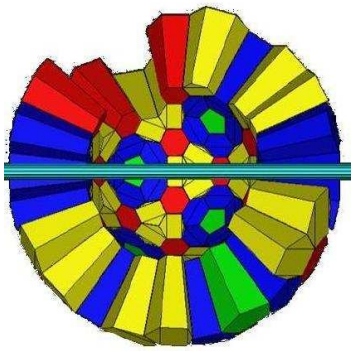

Figure 3.2: The DANCE calorimeter showing a cutaway view of the detector. Different colors indicate different shape of the crystals.

The array consists of 160 BaF_2 crystals of four different shapes that are arranged in a 4π geometry. Each crystal has an equal 734 cm^3 volume and a length of 15 cm. One advantage of the detector is that it measures the total energy of the reaction; events can be separated by Q-value. Based on the signal waveform from the BaF_2 crystals, the system can distinguish γ rays from alpha particles. The high segmentation of the detector enables measurement of the γ-ray multiplicity and the fast scintillator's timing leads to a precise determination of the neutron time-of-flight. The efficiency of the array for detecting a single 1 MeV γ ray is approximately 86%; for a typical γ-ray cascade, where 3 or 4 photons are emitted, the total efficiency is more than 95% [52–54].

3.2 Data Acquisition System

A detailed description of the DANCE data acquisition (DAQ) is given in [55]. The pulse from the crystals photomultiplier output was digitized in Acqiris DC265 digitizers with 8-bit resolution at a sampling rate of 500 MHz. Waveform digitization presents a unique challenge: the per-event data size greatly exceeds the more typical per event data size when using traditional CAMAC (Computer Automated Measurement and Control) electronics. For DANCE the overall data rate can approach 400 Terabyte per day, depending on the target material. Such a data rate cannot be economically recorded for experiments that last up to two weeks, with several such experiments conducted per year. Our solution is to extract and record only the most fundamental information from each waveform, leading to at least a 20 to 1 compression factor. Each waveform was processed on-line to obtain the following information before writing the data to disk: (1) the presample integral of a background baseline is reduced to one integral of 100-ns width, (2) the fast component of the light output to 32 data points at 2-ns sampling, (3) the slow component reduced to five sequential integrals each 200 ns wide, and (4) two time stamps, relative to the beam pulse and to a master clock. The data from the 15 front-end computers were correlated by a single rack-mounted computer and written to a MIDAS data structure.

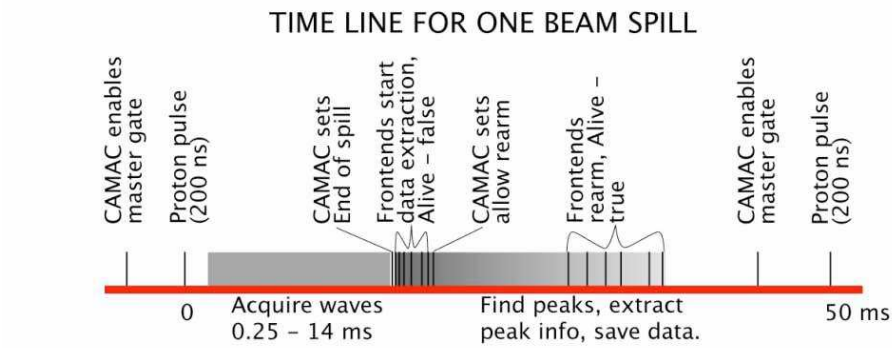

Figure 3.3: Acquisition sequence of events for one proton beam pulse.

The DANCE DAQ was configured in two different data acquisition modes, segmented and continuous. In the segmented mode, the DAQ was enabled with the proton beam pick-off trigger T_0, which arrives slightly before the beam pulse. An individual event

was triggered when at least two crystals inside a $\gamma - \gamma$ coincidence window of 200 ns registered a pulse above a 30-mV discriminator threshold, corresponding to 120-keV γ energy. After a valid trigger, further data acquisition was blocked for 3.5 μs to allow for event analysis and rearming of the Acqiris cards. The DAQ stops after a maximum "looking time" (T_S = 14 ms or 2 ms), and the data were written to disk. Figure 3.3 shows the basic sequence of events during a single proton beam spill.

Two settings of looking time 14 ms and 2 ms in sequential mode cover the neutron energies of 0.02 eV to 0.5 MeV and 1.0 eV - 0.5 MeV, respectively. Although this covers the entire energy range of interest, the dead time corrections inherent in this data acquisition mode become increasingly large at neutron energies above a few eV and over strong resonances. Therefore, we used the continuous mode, which is essentially dead-time free. In the continuous mode all of the digitizers trigger simultaneously in two independent 250-μs wide windows starting from $T_0 + T_{delay}$. The 500-μs wide double continuous window covers the neutron energy range from 8.5 eV to 1 MeV. For the ^{156}Gd and ^{158}Gd targets, the first resonance is at 33.23 eV and 22.30 eV, respectively. therefore it was not necessary to adjust the delay time for these two measurements. However, for the ^{155}Gd target, the first resonance is at 2.008 eV. Therefore we collected data in three different sets of windows: the first window is from 1 MeV to 8.53 eV, the second window is from 8.53 eV to 3.29 eV and the last window is adjusted from 3.79 eV to 1.36 eV.

3.3 Data Analysis

The first steps of the data analysis are performed by the "DANCE Analyzer" software that consists of the following major steps [55]:

1. Calculating the total raw integrals, including baseline subtraction, and determining the time-of-flight for each crystal signal.

2. Sorting the individual signals acquired during a proton beam spill into physics events.

3. Calibrating all of the raw signals to produce physics quantities.

4. Calculating physics quantities from calibrated data.

5. Gating and graphing the data and providing different kinds of histograms for further analysis.

The "Analyzer" requires large amount of memory and CPU usage in the computer to replay the data and the analyzing process continues for several hours. Different sets of gates are applied on neutron and γ-ray energy and the analyzer need to be re-run every time one changes the gates. Clearly, it takes a long time processing to obtain the desired results. Instead, the last step of the analysis is performed by different software "DANA" to save time and computer resources. The energy and time calibration software provides the input parameters for the "Analyzer".

3.3.1 Detector Calibration

Energy Calibration: The BaF_2 crystals were calibrated using ^{88}Y, ^{22}Na, and ^{60}Co γ-ray standards. Because of the scintillators temperature changes, small gain shifts are observed in the light output of each crystal. Since Ba and Ra are chemical homologues, the BaF_2 crystals always contain radioactive isotopes from the uranium decay chain; the alphas from the radioactive decay can be used to adjust the gain shifts. The scintillation light of the BaF_2 crystals has a fast component with a 220-nm wavelength and 0.6-ns decay time constant, and a slow component with a 310-nm wavelength and 600-ns decay time constant. The fast component was obtained by integrating the BaF_2 signal during the first 64 ns, and the slow component was obtained by integrating the signal in the next 1 μs.

The intensity ratio between the fast and slow components is radiation-type dependent, which allows for particle identification if both components are measured. To differentiate between gammas and alphas, the fast versus slow integral can be used, as shown in Fig. 3.4. The α-peaks were fit for each crystal and for each run (see Fig. 3.5) and the α energies were used to update the calibration parameters.

Time Calibration: The scintillation light emitted from the crystals is converted into electrical signals by the PMT. The signal passes though all of the electronics and eventually is registered as an event in the data acquisition computer. If all of the 160 crystals fired simultaneously, the events would still be registered with time deviations because of the different signal transferring times for the crystals (different cable lengths could affect the timing, for instance). Since the size of this deviation is comparable to our γ-γ coincidence

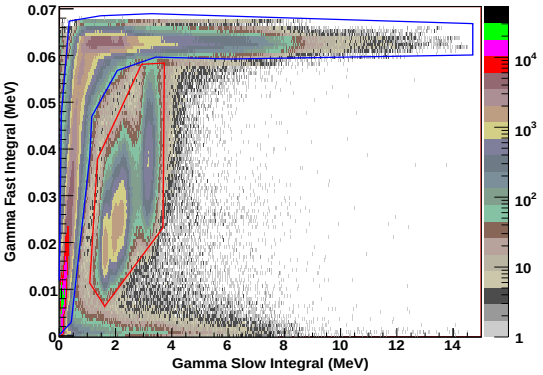

Figure 3.4: Slow versus Fast integral particle discrimination. The blue contour gates γ-rays, while the red contour gates α particles.

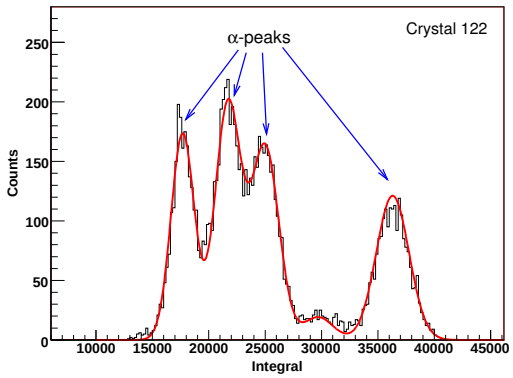

Figure 3.5: The α particle energy spectrum in the ^{226}Ra decay chain.

time window, time synchronization of the crystals must be performed. In order to do this, we choose one of the crystals as a reference and the time deviations are adjusted relative to this crystal.

3.3.2 Background Subtraction

There are several sources of background in DANCE experiments, which can be sorted into three major types [54].

- A time-independent background that is not correlated with the neutron beam. Natural radioactivity, or in case of BaF_2 detectors, intrinsic radioactivity, are prominent examples. If the sample is radioactive, it will introduce another source of time-independent background. The events due to α-decays are suppressed with the slow vs. fast integral method as mentioned before. The crystals contain not only α but also β activity that arises from the Ra decay chain, such as ^{214}Bi and ^{210}Bi. The β particles and γ rays originating from the decay chain are easily recognized by their total energy deposited in the crystals. The low energy contributions of the total energy spectrum (Fig. 3.6) are the signature of the these events.

- A second source of background is correlated with the time structure of the beam. For instance, neutrons scattered from the beam transport materials or γ-flashes originating

at the neutron production area. Since the γ rays travel with the speed of light, they usually arrives before the neutron beam and the γ related background is small.

- The most serious source of background is sample-related; this is discussed in the following.

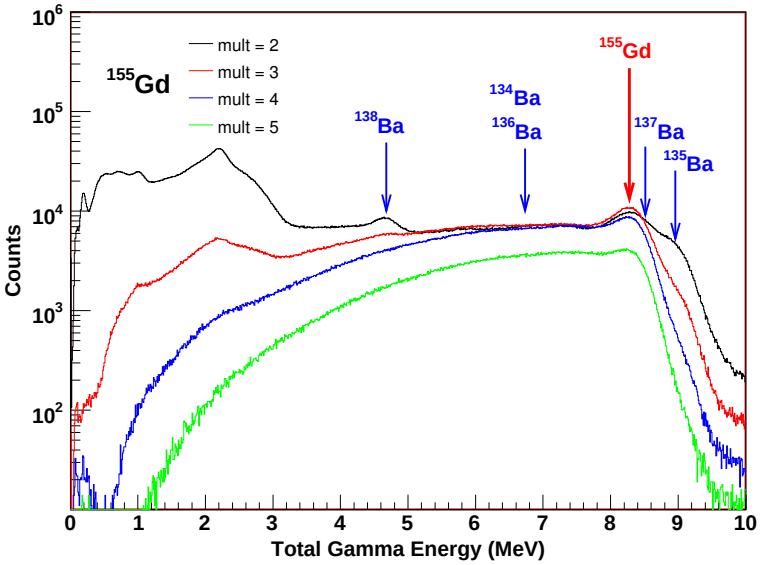

Figure 3.6: Total gamma-ray energy spectra for cluster multiplicity m = 2 - 5. The red arrow indicates the Q-value of ^{155}Gd(n,γ)^{156}Gd reaction. The blue arrows indicates Q-values of radiative capture on Ba isotopes: ^{135}Ba(n,γ) with Q = 9.108 MeV (natural abundance 6.6%), ^{137}Ba(n,γ) with Q = 8.612 MeV (n.a. 11.2%), ^{136}Ba(n,γ) with Q = 6.906 MeV (n.a. 7.9%) and ^{138}Ba(n,γ) with Q = 4.723 MeV (n.a. 71.7%). (Black m = 2, Red m = 3, Blue m = 4, Green m = 5).

Neutrons scattered from the target nuclei are captured in the BaF_2 crystals and create a similar signature as capture in the sample. In order to reduce the scattered neutrons, a ^{6}LiH shell of 6-cm thickness surrounds the target. Despite the absorbing effects of the ^{6}LiH shell, the transmitted neutrons can induce (n,γ) reactions in the crystals either promptly or during the slowing down process. A single γ-ray rarely deposits its total energy in a several crystals because of Compton scattering and pair production. Adjacent crystals that fire in an event are grouped together as a "cluster". The capture γ-rays from the gadolinium target, located at the center of the crystals, are emitted into a 4π solid angle and create several clusters. On the other hand, the capture event of the scattered neutrons in the Ba isotopes are already primarily localized in one of the crystals and create one or

two clusters. In other words, low cluster multiplicity spectra have high background. This effect is shown in the total γ-ray energy spectra Fig. 3.6 with different multiplicities.

Since DANCE is a calorimetric detector, the total γ-ray energy deposited in the BaF_2 crystals from the capture events should be close to the reaction Q-value. The Q-value for the ^{155}Gd(n,γ)^{156}Gd reaction is equal to 8.536 MeV and gating around the peak improves the signal-to-noise ratio significantly (Fig. 3.7). For the ^{155}Gd data, the best signal-to-noise ratio is obtained at the multiplicity gates m = 3-7 and the total-energy gate E_{sum} = 6.5-8.7 MeV.

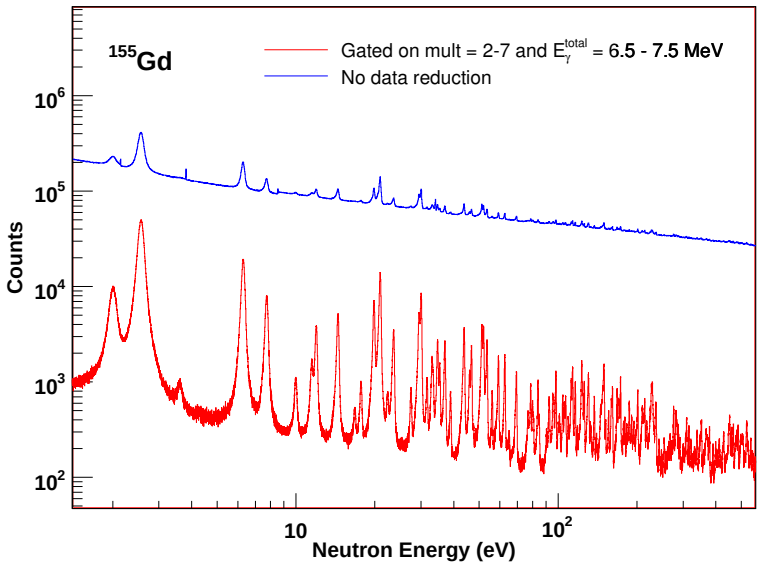

Figure 3.7: Neutron energy spectrum with gates on m = 3-7 and E_{sum} = 6.5-8.7 MeV compared with an ungated spectrum.

Residual background still exists under the peak of interest due to the finite energy resolution of the detector. The contribution of neutron elastic scattering on the ^{155}Gd target cannot be measured directly but can be estimated from the capture events in the Ba crystals. Since the ^{208}Pb isotope has a very small capture cross section and almost constant scattering cross section over a wide range of neutron energy, the total γ-ray energy spectra from the scattered neutron background were measured using ^{208}Pb targets. The events above the ^{155}Gd(n,γ)^{156}Gd reaction Q-value correspond to the scattered neutrons captured on ^{137}Ba (Q = 8.612 MeV) and ^{135}Ba (Q = 9.108 MeV) isotopes in BaF_2 crystals (see Fig. 3.6). Therefore, the total γ-ray energy spectra measured with ^{208}Pb and ^{155}Gd

targets were normalized to the number of events above the Q-value. Figure 3.8 shows total γ-ray energy spectra before and after the background subtraction.

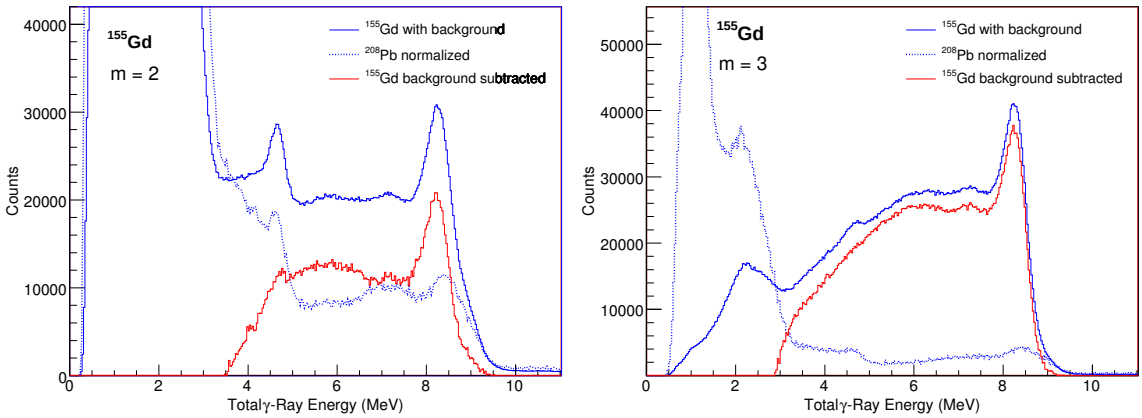

Figure 3.8: Total energy spectra for ^{155}Gd, normalized ^{208}Pb and their subtraction. The blue line represents ^{155}Gd data with background, the dashed blue line normalized ^{208}Pb data and the red line represents the spectrum after background subtraction.

3.4 Experimental Conditions and Uncertainties

3.4.1 Error Propagation

Reporting the uncertainties of the physics quantities determined by the measurement is one of the substantial parts of any physics experiment. The uncertainties can be derived from following equations:

- For Y γ-ray capture events (Y counts), the standard deviation is $\sqrt{Y}$, in other words, the observed number of counts is: $Y \pm \sqrt{Y}$

- For the computed quantity $g(x, y, z)$ which is the function of variables x, y, z, the standard deviation σ_g is:

$$\sigma_g^2 = \sigma_x^2 \left(\frac{\partial g}{\partial x}\right)^2 + \sigma_y^2 \left(\frac{\partial g}{\partial y}\right)^2 + \sigma_z^2 \left(\frac{\partial g}{\partial z}\right)^2 . \tag{3.1}$$

  Note that statistically 67% of the measurements will fall within 1σ and 95% within 2σ.

As an example, the uncertainty is calculated for the average multiplicity introduced in chapter 4;

$$\langle M_J \rangle = \sum_{m=1}^{max} mY_J(m) / \sum_{m=1}^{max} Y_J(m),$$

where $Y_J(m)$ is an experimental yield at multiplicity m for any resonance bin and its uncertainty is $\sqrt{Y_J(m)}$. Using the Eq. (3.1) we can calculate respectively the uncertainties in the numerator and denominator as

$\sigma^2_{num} = \sigma^2_{m=1} + 4\sigma^2_{m=2} + ... + m^2_{max}\sigma^2_{m=max} = \sum_{m=1}^{max} m^2 Y_J(m)$

and $\sigma^2_{denom} = \sigma^2_{m=1} + \sigma^2_{m=2} + ... + \sigma^2_{m=max} = \sum_{m=1}^{max} Y_J(m).$

The total uncertainty in the average multiplicity is

$$\begin{aligned} \sigma_{\langle M_J \rangle} &= \sqrt{\frac{\sigma^2_{num}}{\left(\sum_{m=1}^{max} Y_J(m)\right)^2} + \langle M_J \rangle^2 \frac{\sigma^2_{denom}}{\left(\sum_{m=1}^{max} Y_J(m)\right)^2}} \\ &= \langle M_J \rangle \sqrt{\frac{\sum_{m=1}^{max} m^2 Y_J(m)}{\left(\sum_{m=1}^{max} mY_J(m)\right)^2} + \frac{1}{\sum_{m=1}^{max} Y_J(m)}}. \end{aligned}$$

Several sources of systematic and statistical errors exist, depending on the experimental conditions. Uncertainties in the neutron capture experiments include: the amount of material in the target, the number of neutrons hitting the target, the energy of the neutrons inducing the reaction and the efficiency of the detector registering the reaction products, etc. The total uncertainty of the cross section is given by Eq. (3.1) including all of the errors.

3.4.2 Corrections for Experimental Conditions

In general, it is not possible to directly compare the cross sections extracted from experiments to those generated via any theory. This is because "perfect" experimental conditions do not exist. The R-Matrix code "SAMMY" is used, to include accurate mathematical descriptions of the experimental conditions and to extract resonance parameters [56].

- **Doppler Broadening:** This effect is caused by the thermal motion of the individual nuclei in the sample. Four options are available within SAMMY to account for Doppler broadening; three are based on the free-gas model (FGM), and the fourth is a crystal-lattice model. In our analysis we used the free-gas model to calculate the broadening function. The formula for the FGM expression for Doppler broadening takes the form

$$\sigma_D(E) = \frac{1}{\Delta_D\sqrt{\pi}} \int_0^\infty \left[e^{-4(E-\sqrt{EE'})^2/\Delta_D^2} - e^{-4(E+\sqrt{EE'})^2/\Delta_D^2} \right] \sigma(E') \sqrt{E'/E} dE.$$

  In this expression, σ_D is the Doppler-broadened cross section and σ is the unbroadened cross section. The Doppler width Δ_D is given by

$$\Delta_D = \sqrt{\frac{4mEkT}{M}}.$$

  Here, m represents the neutron mass, M the target (sample) mass, k is Boltzmann's constant, and T is the effective temperature. In the SAMMY input file we provided the temperature and sample thickness as the input parameters.

- **Resolution broadening:** The broadening is the result of, for example, the finite size of the neutron producing target and of the detectors, and the non-negligible burst width and time-channel width. In time-of-flight measurements, the neutron energy is determined by the flight path length and the travel time.

$$E_n = \frac{1}{2}mv^2 = \frac{1}{2}m\left(\frac{L}{t}\right)^2$$

  where m is the neutron mass and v its velocity. From this definition, it is clear that two types of resolution broadening are possible; one due to distributions in time and the other due to distributions in length. The distribution in time includes the time-channel width, and the beam burst width. The flightpath length traversed by a neutron depends on its position of origin within the neutron-producing target, on its position of interaction within the sample, and on the position at which it is detected. Unlike Doppler broadening, for which the mathematical descriptions apply universally to all experiments, the description of the resolution broadening changes from experiment to experiment. Instead, each analysis code has its own version of resolution broadening, with specific formulations for specific experimental sites or setups. For this reason, many distinct types of resolution broadening are available in SAMMY [56]. We used an

option which is a empirical function designed to describe the experimental situation for the linac at Rensselaer Polytechnic Institute (RPI resolution function). This resolution function may be described by the sum of a chi-squared function (with six degrees of freedom) plus two exponential terms. The total resolution function appropriate for data measured on that machine is then the convolution of the target-detector resolution function, with a Gaussian function representing the electron burst and a square function representing the channel width. The parameters are adjusted for the DANCE facility by fitting ^{238}U peaks for which energies and widths of the resonances are well known.

- **Self Shielding and Multiple Scattering:** These corrections must be made for the finite (non-infinitesimal) size of the sample which causes interactions beyond those described by the cross section for individual nuclei. A nucleus deep inside the sample may lie "in the shadow" of other nuclei, and hence see only a portion of the original neutron flux. This effect, designated self-shielding, is easily and accurately calculated. The probability that capture will occur at depth z (within dz) can be written as

$$\frac{n}{D}e^{-n\sigma_t z/D}\sigma_c dz,$$

where n is the sample thickness in $atoms/barn$ and D is the sample thickness in the same unit as z. Subscripts t and c denotes total and capture cross section, respectively. Integrating over z (from 0 to D) gives the self-shielded capture yield

$$Y_0 = [1 - e^{-n\sigma_t}] \left(\frac{\sigma_c}{\sigma_t}\right).$$

Some neutrons will be first scattered by one nucleus (during which process it gives up part of its energy to that nucleus) and subsequently interact with another nucleus. The scattering correction is the increase in the observed capture cross section due to capture of neutrons that have been scattered out of the original beam path. Calculation of the scattering effect is more complicated than self-shielding, because it involves the product of: (a) the probability of reaching a position (x, y, z) inside the sample, (b) the probability of scattering from that position into solid angle Ω within $d\Omega$, (c) the probability of those scattered nuclei reaching position q within dq along that direction, and (d) the probability of being captured at that location. This

product is then integrated over the position q, over solid angle, and over the sample volume, giving the single-scattering result.

Derivation of the effect of two or more scatterers followed by capture is accomplished in a similar manner to the derivation of the single-scattering effect. The exact expression for k scatters involves (3k +3) embedded integrations; it is therefore necessary to make severe approximations in order to derive an expression that can be calculated in a finite amount of time. The self-shielding and multiple scattering corrections are calculated by the SAMMY code using the sample size (thickness and radius) as an input parameter.

Chapter 4

Spin Assignment Methods

Spin assignments of the resonances are useful to determine the level density, the spin dependence of the s-wave strength function, the average radiative width and the effect of intermediate structure and doorway states.

In this chapter we will discuss different spin determination methods for DANCE data and introduce the new method that we have developed. The spin values determined from previous methods are compared with the results of our new method for ^{155}Gd resonances, and the generalized new method is tested for p-wave resonances of ^{94}Mo and ^{95}Mo.

4.1 Introduction

The events registered by the DANCE detector can be sorted by their cluster multiplicity. We denote the experimental yield with cluster multiplicity m at neutron energy E as $Y_m(E)$, which is a component of the "yield vector" in multiplicity space:

$$Y(E) = [Y_1(E), Y_2(E), ..., Y_{max}(E)]^T, \tag{4.1}$$

where $Y_{max}(E)$ is the yield at the maximum multiplicity chosen, and the superscript T denotes the transpose of a vector or a matrix throughout this thesis. Note that the "multiplicity" in the following text will always be the "cluster multiplicity".

As shown by Monte-Carlo simulation [57], the "multiplicity" is a good representation of the true "γ-ray multiplicity", which is equal to the number of γ-rays emitted by the compound nucleus in the capture event. Therefore, the ratio $y_m(E) = Y_m(E)/Y_{total}(E)$

is approximately equal to the m-step cascade probability. The multiplicity distribution can be derived by normalizing the yields at each multiplicity to the total number of counts:

$$y(E) = \Omega^{(J)} = [\omega_1^{(J)}, \omega_2^{(J)}, ..., \omega_{max}^{(J)}]^T, \tag{4.2}$$

where $y_m(E) = \omega_m^{(J)} = Y_m(E)/Y_{total}(E)$ is a normalized yield and $Y_{total}(E) = Y_1(E) + Y_2(E) + ... + Y_{max}(E)$.

The ground-state spin of ^{155}Gd is $3/2^-$. Capturing an s-wave neutron leads to $J^\pi = 1^-$ and 2^- resonances in ^{156}Gd. The γ-ray transition probability depends on the spin and parity of the initial and final states, as explained in Sec. 2.3.3. Therefore, there are two different cascade schemes that result in two different multiplicity distributions, corresponding to the spins of the resonances. As an example, Fig. 4.1 shows the multiplicity distributions of ^{155}Gd resonances with spin $J = 1^-$ and $J = 2^-$.

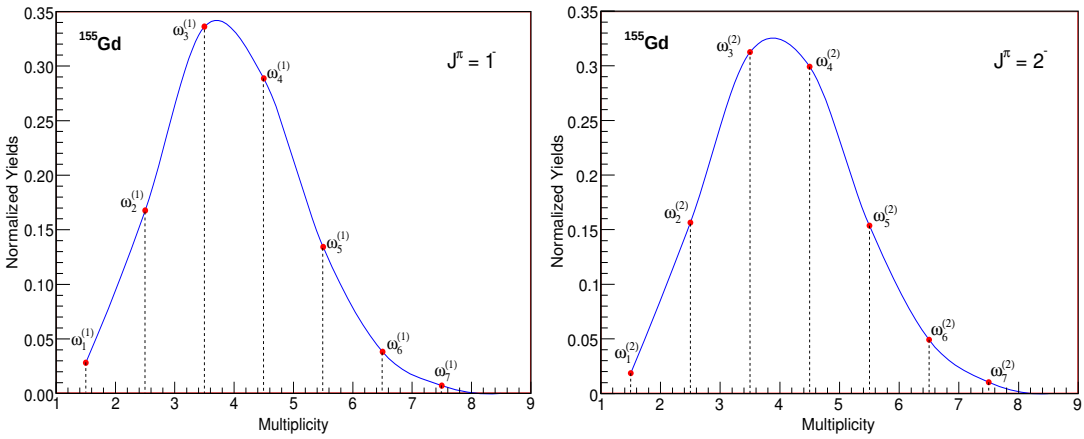

Figure 4.1: Multiplicity distributions of the spin $J = 1$ resonance at neutron energy $E_n = 21.03$ eV and spin $J = 2$ resonance at neutron energy $E_n = 14.51$ eV in ^{155}Gd.

We shall assume that there are different multiplicity distributions for the cascades initiated from states with different spin, but that the distributions are similar for cascades initiated from states with the same spin. Most of the spin determination methods depend upon this assumption. C. Coceva *et al.* [58] initiated the γ-ray multiplicity method at the electron linear accelerator at Geel, Belgium and later variations of the initial method were applied in many experiments.

4.2 Previous Methods

In recent years, various implementations of the γ-ray multiplicity method were introduced to assign the spins of neutron resonances measured with the DANCE detector. In the following sections, we briefly outline the methods and discuss the results for ^{155}Gd(n,γ)^{156}Gd data.

4.2.1 Average multiplicity

The average multiplicity $\langle M_J \rangle$ is defined as the average number of transitions per cascade initiated from a resonance with spin J: $\langle M_J \rangle = \sum_{m=2}^{max} m P_J(m)/P_J(m)$, where $P_J(m)$ is the probability of m transitions in the cascade [59]. Figure 4.2 shows the result of the method applied to ^{155}Gd resonances.

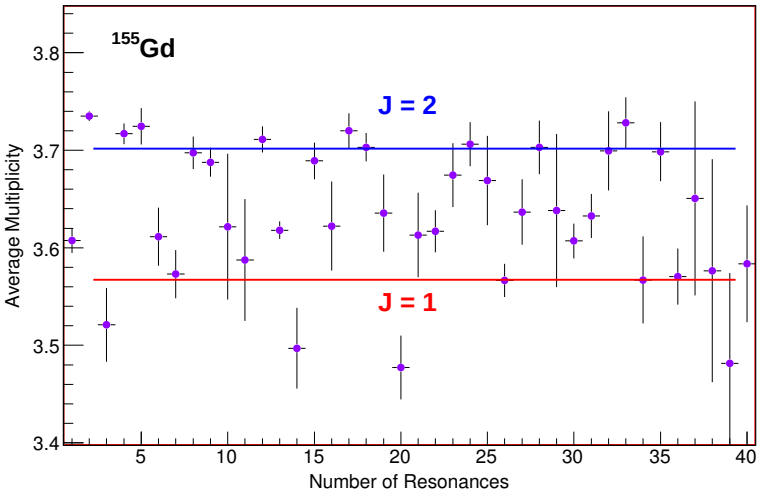

Figure 4.2: Average multiplicity of the ^{155}Gd resonances between neutron energy $E_n = 2.01$ eV and $E_n = 70.0$ eV.

This method could be utilized for resolved resonances, but for partially or unresolved resonances it is unreliable. If the unresolved resonances have different spins, the average multiplicity $\langle M_J \rangle$ is between the values for the two different spins. If the difference between the averages for the two spin groups is small ($\Delta M/\langle M_J \rangle \approx 3\%$ for ^{155}Gd), it is difficult to assign the spins of the weak resonances. Since the neutron flux decreases with increasing energy, the situation become worse at higher energies.

4.2.2 Oak Ridge Method

P.E. Koehler introduced a novel version of the γ-ray multiplicity method [60]. He introduces the function $Z_i^{(J)}(E)$ shown below:

$$Z_1^{(1)}(E) = \sum_{m=a}^{b} Y_m^{(1)}(E) - N_1 \sum_{m=c}^{d} Y_m^{(1)}(E) = 0, \tag{4.3}$$

$$Z_2^{(2)}(E) = \sum_{m=a}^{b} Y_m^{(2)}(E) - N_2 \sum_{m=c}^{d} Y_m^{(2)}(E) = 0, \tag{4.4}$$

where a, b, c, and d are integers, N_i is a normalization constant and $Y_m^{(J)}(E)$ is the yield for a resonance with spin J.

Using isolated resonances for which the spin J is known, the constants N_i are calculated so that the residual yield of the resonances will be zero (Eqs. 4.3 and 4.4). With the assumption that the multiplicity distribution is the same for resonances with the same spin, applying Eq. (4.3) or (4.4) to an arbitrary resonance gives zero or nonzero residuals, depending on the spin of the resonance. In other words, if the resonance has spin $J = 1$, then Eq. (4.3) gives zero residuals and Eq. (4.4) gives non-zero residuals and vice versa. Thus the equations act as spin filters when they are applied to the neutron energy bins.

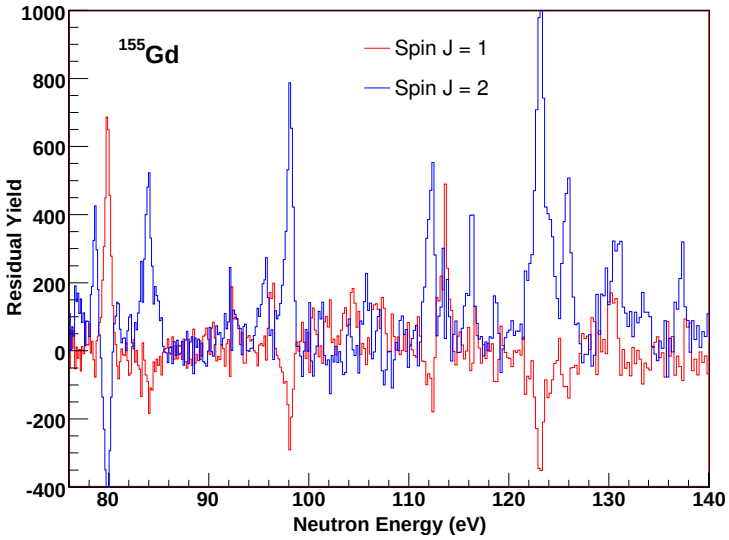

Figure 4.3: Spin determination using the Oak Ridge method between $E_n = 75$ eV and 120 eV for ^{155}Gd. The blue line shows spin 2 resonances, while the red line shows spin 1 resonances

As an example, Fig. 4.3 shows the results of this method in the neutron energy region between 80 eV and 120 eV. A similar picture could be shown for the entire resonance energy range. From the figure we can directly assign $J = 2$ to the resonances at 84.2 eV, 92.5 eV and 98.3 eV, and $J = 1$ to the resonances at 96.6 eV and 104.5 eV.

The spin assignments are uncertain for weak resonances such as those at 94.10 eV and 100.2 eV. Besides, Fig. 4.3 shows that for some resonances the residual yield at one spin group has a negative value instead of zero. Moreover, for some resonances, both equations yield nonzero residuals – the two spin groups seem to overlap at some resonances. (This effect may be reasonable for spin doublets). These facts reveal that due to Porter-Thomas fluctuations the multiplicity distribution is not exactly same for all resonances with the same spin. To deal with these difficulties more general methods of spin determination have been developed.

4.3 Method of Pattern Recognition

The main advantages of the new method may be outlined as follows:

1. It does not choose a single isolated resonance as a prototype. Instead, it estimates the maximum likelihood values of the multiplicity distribution using all of the neutron resonances. Thus it considers the variation of the multiplicity distribution due to Porter-Thomas fluctuations and to experimental errors.

2. The probability density function (PDF) is determined in a multi-dimensional multiplicity space. Thus this method uses as much information as is available and the sensitivity of the method is improved.

3. Based on the estimated PDF, it introduces a discriminant function that minimizes the classification error. The hypothesis testing classifies the experimental data into different spin groups and calculates the probability that the spin assignment is correct.

4.3.1 Introduction to Statistical Pattern Recognition

Humans have developed highly sophisticated skills for sensing their environment and taking actions according to what they observe, such as recognizing faces, understanding spoken words, distinguishing fresh food from its smell, etc. In general, pattern recognition

is a method that gives similar capabilities to machines. This method aims to classify data (patterns) based either on *a priori* knowledge or on statistical information extracted from the patterns. Thus, it may be considered as a problem of estimating density functions in a multi-dimensional space and dividing the space into the regions of categories or classes. In our problem, the resonances with same spin and parity will be classified into the same cluster in multiplicity space. The classification techniques are also called *cluster analysis* or *discriminant function analysis*.

Consider a simple example to illustrate the method. We would like to sort two kinds of fish, sea bass and salmon, on a conveyor belt according to species. Assume that a fisherman told us that a sea bass is generally longer than a salmon. Thus we can use length as a feature and decide between sea bass and salmon according to a length threshold l^*. Even though an average sea bass is longer than an average salmon, there are many

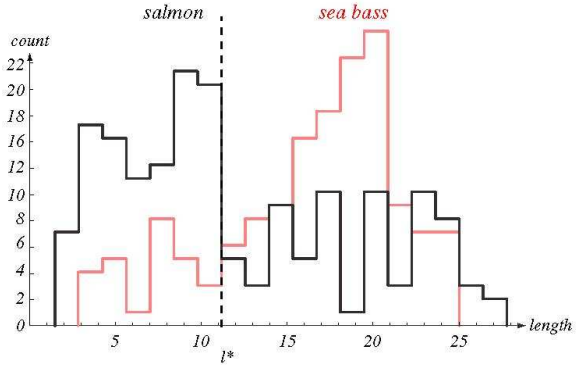

Figure 4.4: Histograms of the length feature for two types of fish.

examples where this observation does not hold. To reduce the decision error we may use the additional feature that sea bass are typically wider than salmon. Each fish image is now represented as a point (feature vector)

$$x = \begin{pmatrix} x_1 = length \\ x_2 = width \end{pmatrix}$$

in a two-dimensional feature space.

From the 2D scatter plot in Fig. 4.5 we can see that adding more features improves the results. The feature space can be multidimensional. However, adding more features does

not always improve the results. Namely, an unreliable feature or one that is correlated with an existing feature, will not give additional information. The result may become even worse if the feature added has large experimental error; in addition one needs to be careful about measurement and computational costs.

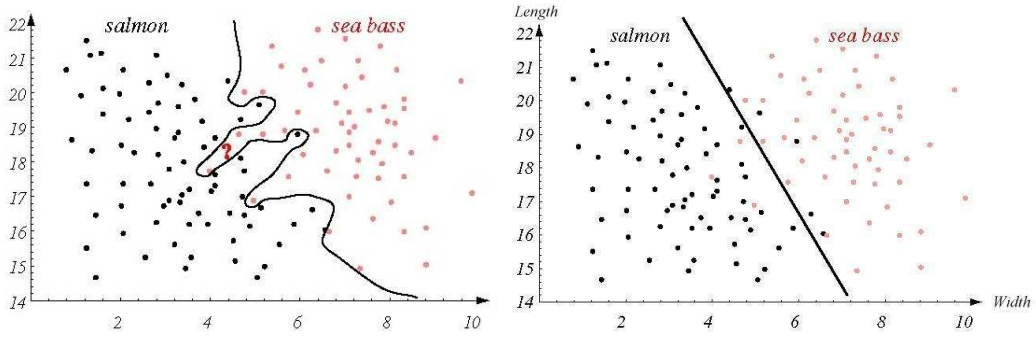

Figure 4.5: 2D Scatter plot of length and width features.

The feature space is divided into two regions by the *decision boundary*. How can we choose this boundary to make a reliable decision? In principle, one may find more complex models with complicated boundaries for the given sample, as shown on the left side in Fig. 4.5. However, it cannot be a perfect decision for any sample. Thus , one has to find the theoretically best classifier for the given distribution of the random variables. This problem is *statistical hypothesis testing* and the *Bayes classifier* is the best classifier which minimizes the classification error [61].

We should also consider the costs of different errors that we make in our decisions. In our example, the customers who buys salmon will object vigorously if they have sea bass in their cans, while the customers who buy sea bass will not be unhappy if they occasionally have some expensive salmon in their cans. Hence, a *higher priority* for the salmon needs to be added into the decision rule. The Bayes classifier considers this rule by including an *a priori* probability.

Consider the method for the spin assignment of neutron resonances in ^{155}Gd. The experimental yields are a multi-dimensional vector, as shown in Eq. (4.1); the “feature space” will be the ”multiplicity space”. In DANCE experiments, the backgrounds for low multiplicity events are large compared to real capture events. From Fig. 4.1 it is clear that the contribution of multiplicity $m = 1$ events is less than 5% for both spins; ignoring this

component will not greatly affect the total counts. The Q-value of the ^{155}Gd(n,γ) reaction is rather high, equal to 8.536 MeV, and so the background subtraction method gives high uncertainty for low multiplicity events (see explanations in chapter 3). For this reason, $m = 2$ events still contain significant backgrounds after subtraction. In addition there are negligible events with $m \geq 7$. Therefore, the multiplicity space is confined to $3 \leq m \leq 6$, which is $p = 4$ dimensional.

We assume that only s-wave neutron resonances are experimentally observed in ^{155}Gd. The p-wave and higher l resonances are negligible for ^{155}Gd due to the orbital angular momentum potential barrier and the minimum of the p-wave strength function in this region. Thus, the normalized yields will create two clusters in m-space, corresponding to $J^\pi = 1^-$ and $J^\pi = 2^-$ resonances.

For the two groups of resonances, the normalized yield Eq. (4.2) can be written as

$$y(E) = \begin{bmatrix} y_1(E) \\ y_2(E) \\ \cdots \\ y_{max}(E) \end{bmatrix} = \alpha_1(E) \begin{bmatrix} \omega_1^{(1)} \\ \omega_2^{(1)} \\ \cdots \\ \omega_{max}^{(1)} \end{bmatrix} + \alpha_2(E) \begin{bmatrix} \omega_1^{(2)} \\ \omega_2^{(2)} \\ \cdots \\ \omega_{max}^{(2)} \end{bmatrix}, \tag{4.5}$$

where $y_m(E)$ is the normalized yield at multiplicity m and $\alpha_1(E)$ and $\alpha_2(E)$ are the weights for the contributions of spin $J = 1$ and spin $J = 2$, respectively, at neutron energy bin E. If the yield at neutron energy bin E belongs to an isolated resonance with spin 1, then $\alpha_1(E) = 1$ and $\alpha_2(E) = 0$ and vice versa for spin 2. For the partially resolved or unresolved resonances the yield at bin E contains a contribution from both spin groups and

$$\alpha_1(E) + \alpha_2(E) = 1.$$

We may also use one of the yields, $Y_m(E)$, as a normalization factor instead of $Y_{total}(E)$. Since $m = 3$ events have the highest counting statistics and low background, we use $Y_3(E)$ to normalize the other events. Equation (4.5) may be rewritten as

$$y'(E) = \alpha_1(E) \begin{bmatrix} \omega_4'^{(1)} \\ \omega_5'^{(1)} \\ \omega_6'^{(1)} \end{bmatrix} + \alpha_2(E) \begin{bmatrix} \omega_4'^{(2)} \\ \omega_5'^{(2)} \\ \omega_6'^{(2)} \end{bmatrix}, \tag{4.6}$$

where $y'_m(E) = Y_m(E)/Y_3(E)$ and $\omega'_m = \omega_m/\omega_3$.

For convenience we omit the notation "prime" in the following expressions – ω replaces ω'.

4.3.2 Probability Density Function

Eqs. (4.5) and (4.6) can be solved analytically, determining the multiplicity distributions (Fig. 4.1) from the prototype resonance. If the multiplicity distributions were exactly the same for all resonances with the same spin, then the equations would give conclusive results. But, experimental errors and backgrounds distort the multiplicity distributions. Even if there were perfect experimental results with no errors or backgrounds, the multiplicity distributions will not be the same due to the PT fluctuations. Consequently, the calculated weights, $\alpha_J(E)$, would behave same as in the results of the Oak Ridge method and we could not assign the spin of the weak resonances.

The normalized yields, $y_m(E)$, distribute around the mean values $\omega_m^{(J)}$ which has two centroids, corresponding to $J^\pi = 1^-$ and $J^\pi = 2^-$. The radiative decay of the compound nuclei is a statistical process. Based on the central limit theorem, we may assume that the distribution function is a Gaussian.

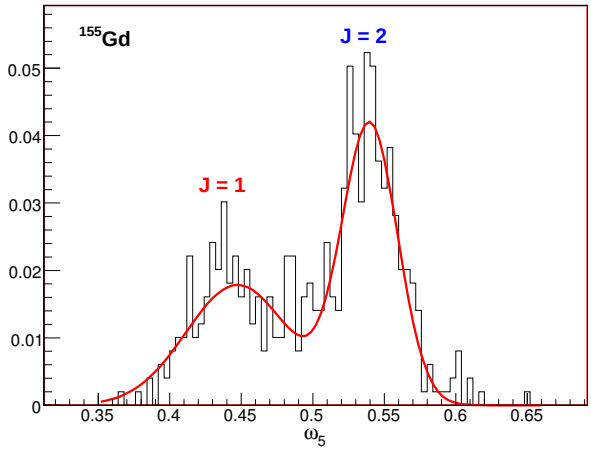

Figure 4.6: Probability Distribution Function for normalized yields of ^{155}Gd at multiplicity $m = 5$.

Since we have two spin groups, the probability density function (PDF) is a mixture of two Gaussians. The centroids of the Gaussians $\omega_m^{(1)}$ and $\omega_m^{(2)}$ represent the m component of the multiplicity distribution for the corresponding spins. The widths of the Gaussians

are the sum of the experimental uncertainty and the PT fluctuations $\sigma^2 = \sigma^2_{exp} + \sigma^2_{PT}$. The distribution of the normalized yields for the multiplicity $m = 5$ component is shown in Fig. 4.6. This is analogous to the distribution shown in Fig. 4.4. A similar distribution plot can be obtained for any other multiplicity.

Generalizing this behavior, the PDF is multivariate normal in multiplicity space. We have confined the multiplicity space to $m_{min} = 3$ and $m_{max} = 6$, with the events at $m = 3$ used for normalization. In other words, the feature vector will be a three dimensional random vector whose components are the normalized yields at multiplicity 4, 5 and 6. The joint PDF, $g(y|\Omega)$, will be a mixture of two multivariate normal distributions corresponding to two spin groups.

$$g(y|\Omega) = \beta_1 f_1(y|\Omega_1, \Sigma_1) + \beta_2 f_2(y|\Omega_2, \Sigma_2), \tag{4.7}$$

where Ω forms a parameter space: $\Omega = (\Omega_1, \Omega_2, \Sigma_1, \Sigma_2, \beta_1, \beta_2)^T$. The parameters β_1 and β_2 are the mixing weights that represent the number of spin $J = 1$ and $J = 2$ resonances in the sample. The mixing weights may also be called the *a priori* probability for any resonance to have spin $J = 1$ or $J = 2$. They satisfy the condition:

$$\begin{cases} \beta_1 \geq 0 \ , \ \beta_2 \geq 0 \\ \beta_1 + \beta_2 = 1 \end{cases} \quad \text{hence, if } \beta_1 = \beta \text{ then } \beta_2 = 1 - \beta.$$

The multivariate normal density functions are described as follows:

$$f_k(y|\Omega_{(k)}, \Sigma_{(k)}) = \frac{1}{(2\pi)^{N/2}|\Sigma_{(k)}|^{1/2}} \exp -\frac{1}{2}(y - \Omega_{(k)})^T \Sigma^{-1}_{(k)}(y - \Omega_{(k)}) \text{ with } k = 1, 2, \tag{4.8}$$

where $\Omega_{(k)} = [\omega_4^{(k)}, \omega_5^{(k)}, \omega_6^{(k)}]^T$ (with $k = 1$ and 2) is a column vector with three components, $\Sigma_{(k)}$ is a covariance matrix that is a real, 3×3 dimensional positive definite matrix, N denotes a sample size or bin numbers in resonance region of neutron energy, the normalized yields are described as $y = [y(1), y(2), \ldots, y(i), \ldots, y(N)]$ and each data point is a 3-dimensional vector $y(i) = [y_4(i), y_5(i), y_6(i)]^T$. Note, the normalized yields are a function of neutron energy, $y_m(E)$, in Eq. (4.2). The normalized yield samples in Eq. (4.8) are collected from each neutron energy bin, i, which is equivalent to $y_m(i) = y_m(E)$.

4.3.3 Optimum Design Procedure and Hypothesis Testing

The purpose of the analysis is to determine to which class or spin group a given resonance belongs. In order to accomplish this purpose, we need to set a "decision bound-

ary", $h(y)$, to separate the distributions into two regions (Fig. 4.5). The term, $h(y)$, is called the *discriminant function*, and is a function of the parameters of the distribution. The simplest form of the function is called the Linear Classifier.

Figure 4.7 shows the two dimensional scatter plot with a *linear discriminant function*, where small circle points depict the location of the sample, $y(i) = [y_5(i), y_6(i)]^T$, and solid elliptical lines are the contour lines of the PDF.

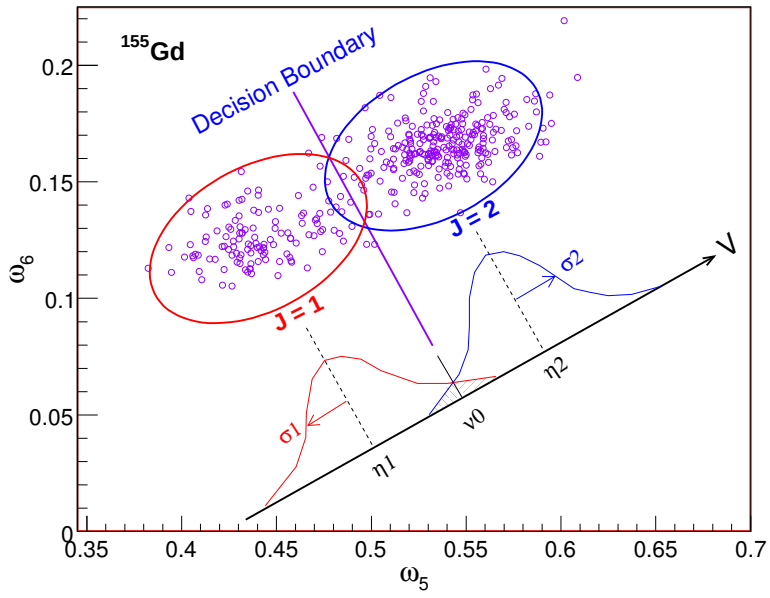

Figure 4.7: Two dimensional example of the multivariate normal distributions.

The linear discriminant function is

$$h(y) = V^T y(i) + \nu_0 \begin{cases} > 0 \rightarrow \omega_1 \\ < 0 \rightarrow \omega_2 \end{cases}, \tag{4.9}$$

which means that $y(i)$ belongs to spin 1 if $h(y) > 0$ and belongs to spin 2 if $h(y) < 0$.

Equation (4.9) indicates that a p-dimensional vector $y(i)$ is projected onto a vector V. Our goal is to find the optimum coefficients $V = [v_1, v_2, \ldots, v_p]^T$ and the threshold value ν_0 for the given distributions. The criteria to find the optimum values is the minimization of the error with respect to V and ν_0 [61].

Skipping detailed discussions about the optimization criteria of the linear discriminant function, we note that no linear classifiers work well for distributions which are not

separated by mean-difference, but are only separated by the covariance-difference . In this case, one needs a higher order classifier such as quadratic.

4.3.4 Bayes Classifier

A decision rule is simply based on the probabilities and can be written as follows:

$$\begin{cases} p_1(y) > p_2(y) \rightarrow \omega_1 \\ p_1(y) < p_2(y) \rightarrow \omega_2 \end{cases} \tag{4.10}$$

where ω_k represents a spin group and $p_k(y)$ is *a posteriori* probability determining whether y belongs to ω_1 or ω_2.

Using Bayes theorem, the *a posteriori* probability $p_k(y)$ is calculated from *a priori* probability β_k and the conditional density function $f_k(y)$,

$$p_k(y) = \frac{\beta_k f_k(y|\Omega_{(k)}, \Sigma_{(k)})}{g(y|\Omega)}, \tag{4.11}$$

where the density function $f_k(y|\Omega_{(k)}, \Sigma_{(k)})$ and the mixture density function $g(y|\Omega)$ are given in Eqs. (4.7) and (4.8).

Based on the decision rule, the discriminant function is determined and the equation is called the *Bayes test for minimum error*

$$h(y) = -\ln f_1(y|\Omega_1, \Sigma_1) + \ln f_2(y|\Omega_2, \Sigma_2) < \ln \frac{\beta_1}{\beta_2} \rightarrow \begin{cases} \omega_1, \text{if true} \\ \omega_2, \text{if false} \end{cases} \tag{4.12}$$

We have already determined the distribution function $f_k(y)$ in Eq. (4.8); substituting it in Eq. (4.12) we find

$$h(y) = \frac{1}{2}(y - \Omega_1)^T \Sigma_1^{-1}(y - \Omega_1) - \frac{1}{2}(y - \Omega_2)^T \Sigma_2^{-1}(y - \Omega_2) + \frac{1}{2} \ln \frac{|\Sigma_1|}{|\Sigma_2|}. \tag{4.13}$$

The parameters of the distribution are unknown. So we need to estimate them from the experimental data.

4.3.5 Parameter estimation

We will estimate the parameter vector $\Omega = (\Omega_1^T, \Omega_2^T, \Sigma_1, \Sigma_2, \beta)^T$, by a maximum likelihood (ML) method. The likelihood function for Ω formed from the observed data y is

given by

$$L(\Omega) = \prod_{i=1}^{N} g(y|\Omega) = \prod_{i=1}^{N} \left[\beta f_1(y|\Omega_1, \Sigma_1) + (1-\beta) f_2(y|\Omega_2, \Sigma_2)\right]. \tag{4.14}$$

In practical applications, it is convenient to maximize the log-likelihood function. The position of the maximum of $L(\Omega)$ and $l(\Omega)$ are identical:

$$l(\Omega) = \ln L(\Omega) = \ln \left[\prod_{i=1}^{N} g(y|\Omega)\right] = \sum_{i=1}^{N} \ln g(y|\Omega). \tag{4.15}$$

Obviously, there are no analytical solutions for the likelihood equations of the mixture model. Hence, the parameters are usually estimated by an iteration method known as the Expectation-Maximization (EM) algorithm. Each EM iteration consists of two steps, an E-step and an M-step. Given an estimation of the population means, covariance matrices $\Sigma_{(k)}$, and mixing proportions β, the E-step is computes the *a posteriori* probability (Eq. 4.11) that data y_i belongs to the spin group 1 or 2. In the M-step, parameters are estimated from the data given the conditional probabilities $f_k(y_i|\Omega_{(k)}, \Sigma_{(k)})$. The expressions of the parameters can be stated as [62]:

$$\beta_k = \frac{1}{N} \sum_{i=1}^{N} f_k(y_i|\Omega_{(k)}^{old}, \Sigma_{(k)}^{old}), \tag{4.16}$$

$$\Omega_{(k)} = \frac{\sum_{i=1}^{N} y_i f_k(y_i|\Omega_{(k)}^{old}, \Sigma_{(k)}^{old})}{\sum_{i=1}^{N} f_k(y_i|\Omega_{(k)}^{old}, \Sigma_{(k)}^{old})}, \tag{4.17}$$

$$\Sigma_{(k)} = \frac{\sum_{i=1}^{N} f_k(y_i|\Omega_{(k)}^{old}, \Sigma_{(k)}^{old})(y_i - \Omega_{(k)}^{old})(y_i - \Omega_{(k)}^{old})^T}{\sum_{i=1}^{N} f_k(y_i|\Omega_{(k)}, \Sigma_{(k)})}, \tag{4.18}$$

where the superscript "old" represents the last iteration for which the values remained constant in the present iteration.

A priori probabilities are initialized from the $2J+1$ level density law and remain constant during the iteration. The covariance matrix initially was set as a three dimensional identity matrix. The E-step and M-step are iterated until a steady state or a maximum number of iterations is reached. However, the stopping criterion for the EM algorithm is a well known problem and the results of EM are highly dependent on the initial values. Convergence is usually fast for our data and we have not found problems concerning this issue. About 15 iterations will result in solutions that are accurate to about 1 percent.

4.3.6 Results for ^{155}Gd resonances

The EM algorithm provides a spin assignment and the probability that the assignment is correct. Using the new technique, we have determined the spins for almost all of the *s*-wave resonances in ^{155}Gd. As an example, Fig. 4.8 shows a graphical illustration of the results in the neutron energy range between 1 eV and 25 eV. The rest of the results are shown in Appendix A.

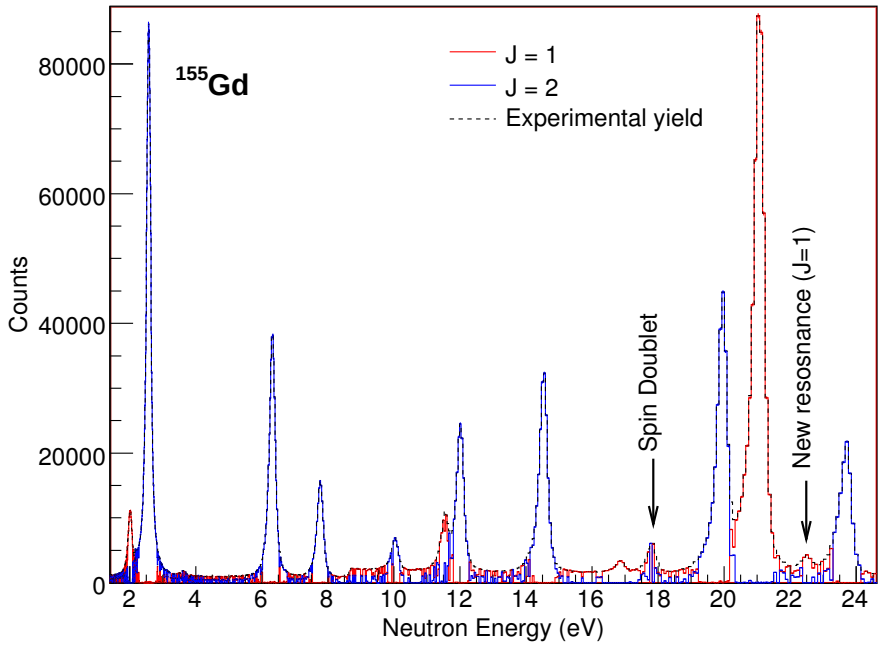

Figure 4.8: Spin assignments of the neutron resonances in ^{155}Gd.

The last iteration of the EM iteration gives the *a posteriori* probabilities $p_1(y)$ and $p_2(y)$ for each neutron energy bin. The relative yields for spin $J = 1$ and $J = 2$ shown in Fig. 4.8 were calculated by multiplying the probabilities times the experimental yield. For example, $p_1(y) \approx 1$ and $p_2(y) \approx 0$ for the bins of spin $J = 1$ resonance at 21.03 eV and multiplying them with Y_{exp} gives nearly zero yields for spin $J = 2$ (blue line in Fig. 4.8) and $Y_1 \approx Y_{exp}$ (red line in Fig. 4.8). As we can see, for most cases, the relative yields for spin $J = 1$ or $J = 2$ resonances agree with the experimental yields, indicating that the probabilities are nearly 100 percent. For some resonances the relative yields from both spin groups are noticeable (see for example resonance at 17.77 eV). Those cases suggest spin

doublets. However, this effect could also be observed for weak resonances due to background contamination. Therefore we assigned spin doublets only for strong resonances.

Based on these results, we plot the cumulative number of resonances as a function of resonance energy – see Fig. 4.9. The reciprocal of the slope of the staircase plot determines the average level spacing of the s-wave neutron resonances. The average level spacing of the s-wave neutron resonances is calculated as $D_0 = 1.76 \pm 0.09$ eV.

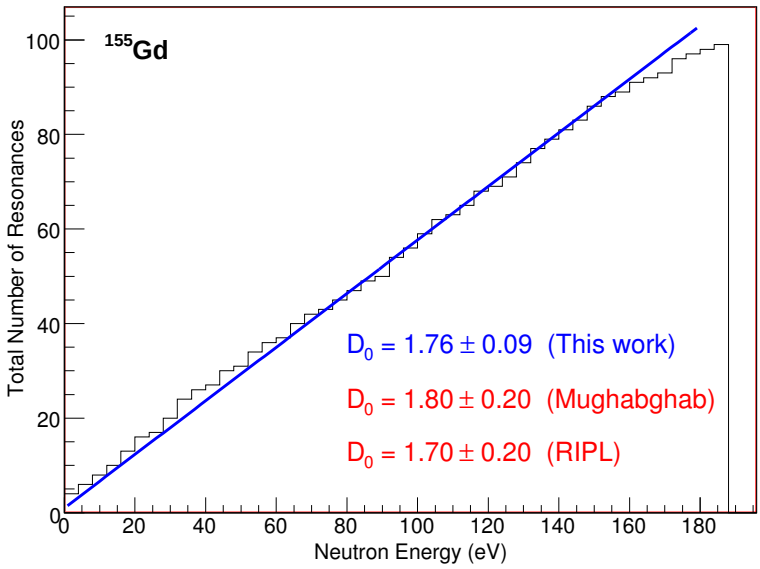

Figure 4.9: Cumulative sum of s-wave resonances in ^{155}Gd.

The staircase plots were drawn for each spin group (Fig. 4.10) and the average level spacings determined as $D_{0.1} = 4.6 \pm 0.4$ eV and $D_{0.2} = 2.9 \pm 0.2$ eV, respectively, for $J = 1$ and $J = 2$ resonances. The level spacing for the two spin groups is in agreement with the expected $2J + 1$ level spacing. The error of the average spacings was calculated by the formula given in [10]

$$\Delta D = \frac{0.53D}{\sqrt{N}}.$$

Table 4.1 shows the spin assignment results and compares them with the data in reference [10]. The spin assignments and the probabilities given in the table are the results of the EM algorithm. The average multiplicities, $\langle M_J \rangle$, were calculated by the equation given in Sec. 4.2.1.

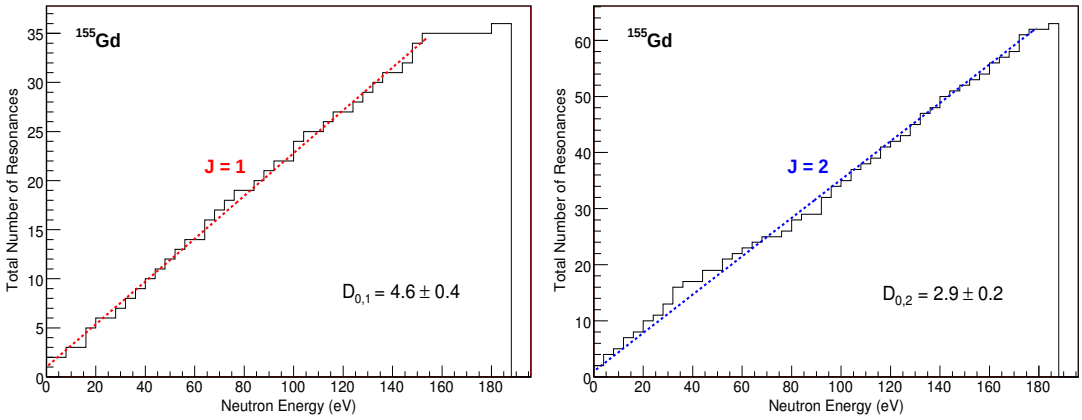

Figure 4.10: Cumulative sum of spin $J = 1$ (left) and $J = 2$ resonances (right) in ^{155}Gd.

Table 4.1: Spin assignments of neutron resonances for the ^{155}Gd(n,γ)^{156}Gd reaction. The DANCE results are compared with the results quoted in the compilation by Mughabghab [10].

Mughabghab			This Work			
En, eV	J	$g\Gamma_n$ (meV)	J	Prob. (%)	$\langle M_J \rangle$	Comment
2.01	1	0.278 ± 0.003	1	99.5	3.61	
2.57	2	2.18 ± 0.02	2	99.7	3.74	
3.62	-	0.033 ± 0.002	1	78.2	3.52	New
6.3	2	2.50 ± 0.15	2	99.5	3.72	
7.75	2	1.40 ± 0.05	2	99.9	3.72	
10.01	2	0.21 ± 0.02	2	97.4	3.61	
11.53	1	0.45 ± 0.03	1	98.4	3.57	
11.99	2	1.10 ± 0.05	2	98.1	3.70	
14.51	2	2.4 ± 0.2	2	99.5	3.69	
17.77	2	0.49 ± 0.03	2	95.8	3.62	
17.80	-	-	1	99.4	3.59	Spin doublet
19.92	2	5.7 ± 0.4	2	99.0	3.71	
21.03	1	19.5 ± 0.9	1	99.8	3.62	

Table 4.1 – continued from previous page

Mughabghab			This Work			
En, eV	J	$g\Gamma_n$ (meV)	J	Prob. (%)	$\langle M_J \rangle$	Comment
22.44	-	-	1	65.4	3.50	New
23.67	2	3.9 ± 0.1	2	97.4	3.69	
27.57	2	0.84 ± 0.02	2	99.3	3.62	
29.58	2	5.4 ± 0.4	2	98.7	3.72	
30.1	2	13.0 ± 3.0	2	99.0	3.70	
31.72	2	1.40 ± 0.04	2	97.9	3.64	
33.14	-	1.4 ± 0.3	1	98.0	3.48	New
33.51	2	1.2 ± 0.3	2	91.2	3.61	
34.83	1	4.6 ± 0.3	1	99.1	3.62	
35.47	2	2.30 ± 0.12	2	99.5	3.67	
37.12	2	6.3 ± 0.2	2	99.4	3.71	
39.0	2	1.3 ± 0.2	2	97.4	3.67	
43.92	1	13 ± 1	1	100	3.57	
46.1	1	2.8 ± 0.2	1	93.8	3.64	
46.87	2	6.7 ± 0.3	2	98.6	3.70	
47.73	1	0.49 ± 0.04	2	78.6	3.64	Disagree
51.38	1	14.0 ± 0.7	1	99.8	3.61	
52.13	1	14.6 ± 0.5	1	99.6	3.63	
53.03	1	1.70 ± 0.06	2	99.5	3.70	Disagree
53.74	2	9.6 ± 0.7	2	98.7	3.73	
56.22	1	2.7 ± 0.2	1	99.8	3.57	
59.32	2	8.3 ± 0.2	2	99.5	3.70	
62.84	1	10.0 ± 0.4	1	100	3.57	
64.09	1	0.32 ± 0.04	2	99.9	3.65	Disagree
65.2	2	1.0 ± 0.2	1	96.7	3.52	Disagree
68.78	1	-	2	61.6	3.58	Disagree
69.4	1	7.9 ± 0.3	1	99.2	3.60	
77.0	2	2.0 ± 0.1	2	98.7	3.61	
77.8	1	0.90 ± 0.05	1	75.9	3.59	

Table 4.1 – continued from previous page

Mughabghab			This Work			
En, eV	J	$g\Gamma_n$ (meV)	J	Prob. (%)	$\langle M_J \rangle$	Comment
78.8	2	5.3 ± 0.5	2	99.5	3.64	
80.05	2	0.39 ± 0.14	1	97.6	3.38	Disagree
80.9	2	1.8 ± 0.2	2	100	3.59	
84.2	2	6.9 ± 0.2	2	95.5	3.65	
85.0	2	2.30 ± 0.12	2	96.7	3.64	
90.5	2	1.60 ± 0.06	1	66.6	3.53	Disagree
92.5	-	2.70 ± 0.29	1	86.3	3.60	New
92.8	-	3.90 ± 0.36	2	98.1	3.61	New
94.1	1	0.68 ± 0.05	1	53.4	3.67	
95.7	-	4.80 ± 0.33	2	99.2	3.67	New
96.6	1	4.70 ± 0.31	1	97.4	3.64	
98.3	-	13.00 ± 0.39	2	100	3.74	New
100.2	2	1.6 ± 0.2	2	58.5	3.68	
101.4	-	3.4 ± 0.3	2	98.4	3.71	New
102.1	-	1.3 ± 0.2	1	93.8	3.57	New
104.4	1	6.8 ± 0.8	1	99.8	3.58	
105.9	2	4.6 ± 0.4	2	95.9	3.67	
107.1	1	7.8 ± 0.6	1	79.7	3.62	
109.6	2	3.5 ± 0.3	2	93.8	3.67	
112.4	2	11.3 ± 1.5	2	95.9	3.73	
113.8	1	19 ± 3	1	99.7	3.61	
116.5	2	13.0 ± 1.7	2	95.8	3.69	
117.8	-	-	1	93.1	3.66	Spin Doublet
118.6	2	2.5 ± 0.2	2	84.5	3.67	
123.4	2	27.0 ± 4.3	2	99.2	3.73	
124.4	2	8.3 ± 0.9	2	65.5	3.68	
126.0	2	15.4 ± 2.1	2	74.7	3.71	
128.6	1	1.40 ± 0.17	1	93.3	3.69	
129.8	-	3.20 ± 0.53	2	86.6	3.67	New

Table 4.1 – continued from previous page

Mughabghab			This Work			
En, eV	J	$g\Gamma_n$ (meV)	J	Prob. (%)	$\langle M_J \rangle$	Comment
130.8	1	36.4 ± 5.7	1	90.6	3.67	
133	-	2.8 ± 0.4	[2]	87.5	3.67	Weak
133.8	-	2.9 ± 0.5	[1]	96.4	3.65	Weak
134.7	-	1.1 ± 0.2	2	76.1	3.75	
137.8	2	16.0 ± 1.5	2	93.2	3.68	
138.5	-	-	1	100	3.58	Spin Doublet
140.4	2	3.10 ± 0.34	1	73.4	3.61	Disagree
141.4	-	1.30 ± 0.21	2	93.5	3.66	New
145.6	2	7.7 ± 0.7	2	97.0	3.68	
146.9	-	4.7 ± 0.6	2	98.5	3.66	New
148.2	1	12.0 ± 1.4	1	97.0	3.61	
149.6	-	25.0 ± 7.2	1	92.1	3.62	New
150.2	-	31 ± 11	2	94.8	3.68	New
152.2	1	6.0 ± 0.5	1	99.0	3.58	
154	-	1.4 ± 0.2	[2]	-	3.60	Weak
156.3	1	9.6 ± 0.8	1	99.9	3.59	
160.1	2	12.0 ± 1.3	2	100	3.72	
161.6	2	25.0 ± 3.2	2	97.2	3.74	
168.3	2	22.6 ± 2.4	2	98.7	3.76	
170.3	-	10.4 ± 1.5	1	53.1	3.70	New
171.4	-	11.5 ± 1.6	2	99.4	3.72	
173.5	2	41 ± 5	2	96.9	3.71	
175.6	2	2.60 ± 0.29	2	99.6	3.74	
178.0	2	7.3 ± 0.7	2	99.9	3.77	
180.4	2	11.0 ± 1.1	2	96.8	3.73	
183.3	1	8.0 ± 0.8	1	75.3	3.63	

4.3.7 Generalization for p-wave resonances

For low energy neutrons on medium and heavy mass targets the orbital angular momentum barrier plays a crucial role. This leads to the occurrence of only s-wave resonances in the eV energy region for ^{155}Gd. However, for lighter mass isotopes such as ^{94}Mo and ^{95}Mo many p-wave resonances are observed. This is due both to a reduced effect of the orbital angular momentum barrier and to the fact that the p-wave strength function has a maximum in this mass region. The ground state spins of ^{94}Mo and ^{95}Mo are 0^+ and $5/2^+$, respectively. Capturing p-wave neutrons on ^{95}Mo leads to p-wave resonances that have more than two spin groups. Table 4.2 lists the spin and parity of the resonances for molybdenum isotopes and the simulated value of the average multiplicity taken from the reference [59].

Table 4.2: The spins of s- and p-wave resonances for ^{94}Mo and ^{95}Mo isotopes and the predicted average multiplicity.

Isotope	$J^\pi(< M >)$			
^{94}Mo, s-wave	$1/2^+(3.25)$			
^{94}Mo, p-wave	$1/2^-(3.03)$	$3/2^-(3.07)$		
^{95}Mo, s-wave		$2^+(3.90)$	$3^+(4.23)$	
^{95}Mo, p-wave	$1^-(3.30)$	$2^-(3.68)$	$3^-(4.00)$	$4^-(4.30)$

In principle, our method can be utilized for any number n of spin groups. Equation (4.19) is a generalized form of the mixture model given in Eq. (4.7) for n number of spin and parity components. The EM algorithm is directly applied for each component, as given in Eqs. (4.11), (4.16) and (4.17):

$$g(y|\Omega) = \sum_{k=1}^{n} \beta_k f_k(y|\Omega_{(k)}, \Sigma_{(k)}). \tag{4.19}$$

Execution of the EM iteration guarantees that a local maximum of the likelihood function is reached, but does not guarantee that this is the best one. A possible technique to circumvent this difficulty is to initialize the algorithm multiple times with different initial parameters, measuring the likelihood function after each run. This exhaustive search increases the chances of finding the global maximum. For our data set there is some previously known information that can be utilized for an initial parameter guess. In other words, we can choose initial parameters using the resonances for which the spin and parity are previously known.

On the other hand, when the data really is clustered, and enough data is available, local search methods typically succeed in optimizing the objective and recovering the clustering. An upper bound on the computational limit of clustering the minimum required separation and minimum required sample size for which recovering the clustering is tractable. If the distances between the clusters are small, then we cannot separate them into different spin groups. When not enough samples are available, even when the data is generated from a well separated mixture of Gaussians, the correct model cannot be recovered, because there is not enough information in the data. However, to study these two limits is not our goal here: we directly applied the method for resonances of the ^{94}Mo and ^{95}Mo isotopes.

4.3.8 Results for ^{95}Mo resonances

For ^{95}Mo, there are six spin and parity groups and the separation between them is very small (see table 4.2). For 4^- - 3^+ and 3^- - 2^+ resonances, DICEBOX simulations predict that the differences between the average multiplicities are expected to be less than 2%. Therefore the γ-ray multiplicity method failed to assign the spin and parity for ^{95}Mo resonances. However, there is more information that can be utilized. The shape of the γ-ray spectrum is strongly dependent on the parity of the resonances.

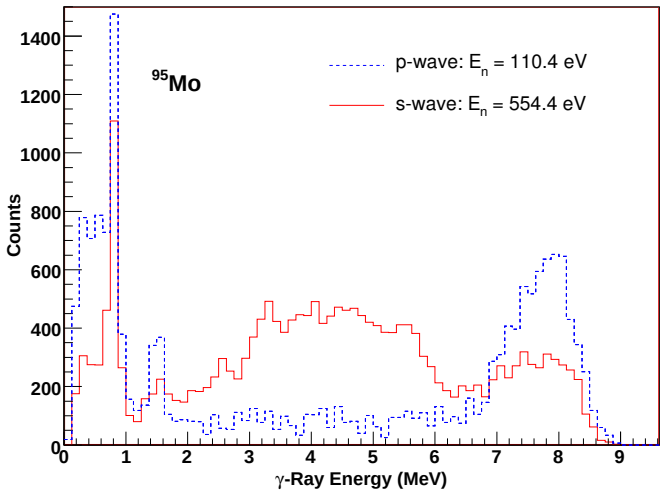

Figure 4.11: γ-ray spectrum of the s- and p-wave resonances in ^{95}Mo. The red line represents the p-wave resonance at 110.4 eV and the dashed blue line the s-wave resonance at 554.4 eV.

The s-wave resonances have positive parity and the p-wave resonances negative

parity. The γ-ray spectra for the two-step cascade has a hump around the 4 to 5 MeV region, but this is not true for the p-wave resonances (Fig. 4.11). Therefore we could simply check the shape of the γ-ray spectra and sort the resonances as p- or s-wave. During this classification process, we have seen that the strong resonances are usually s-wave and the weak resonances are p-wave. This is reasonable, because the orbital angular momentum barrier affects the reaction probability. Based on this simple assumption we classified some weak resonances as p-wave for which the γ-ray spectrum has extremely low statistics and we could not confidently recognize the shape of the resonances. Once we classified the resonances by their parity the multiplicity method can be applied.

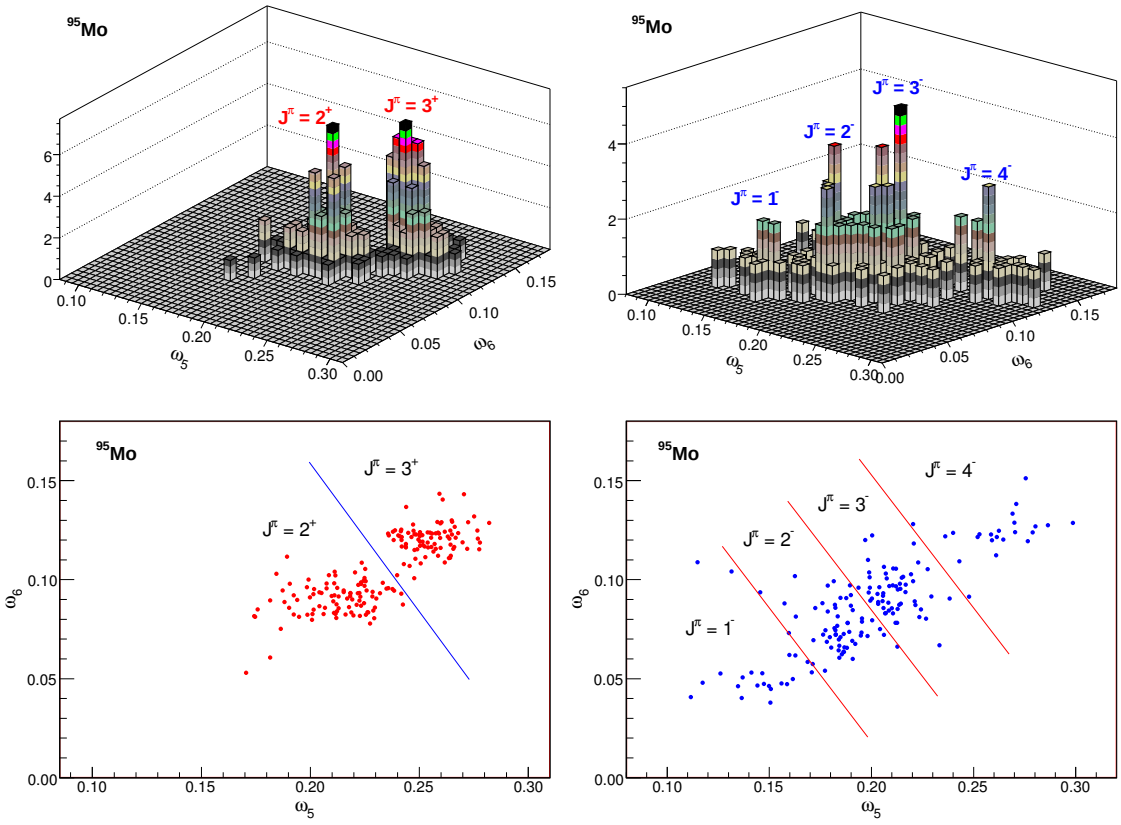

Figure 4.12: Scatter plot for s- and p-wave resonances in ^{95}Mo. On the left side are the s-wave resonances; the p-wave resonances are on the right.

Figure 4.12 shows the (m = 4 vs. m = 5) 2D scatter plot for the ^{95}Mo resonances. As we can see from the plot there are two peaks for s-wave resonances corresponding to 2^+ and 3+ and four peaks for p-wave resonances corresponding to 1^-, 2^-, 3^- and 4^-. As

predicted by the DICEBOX simulation 4^- - 3^+ and 3^- - 2^+ resonances are mixed, which is clearly shown in Fig. 4.13.

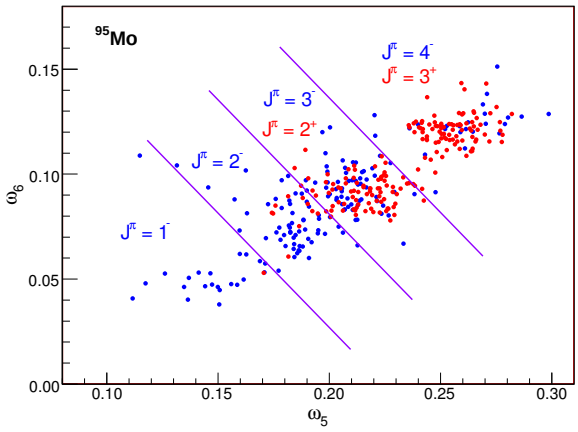

Figure 4.13: 2D scatter plot for ^{95}Mo. Blue circles represent p-wave resonances and red circles represent s-wave resonances.

The parity of the resonances was assigned by the shape of the γ-ray spectrum. We observed several cases that our parity assignments were different from the assignments in Mughabghab [10]. As an example, Fig. 4.14 shows the γ-ray spectrum of the s-wave resonance at energy 263.3 eV that was assigned as p-wave in reference [10] and a p-wave resonance at 1340 eV that was assigned as s-wave. Similar plots for the s-wave resonances at E_n = 466.7 eV, 1035.7 eV and 1495.5 eV are shown in Appendix B.

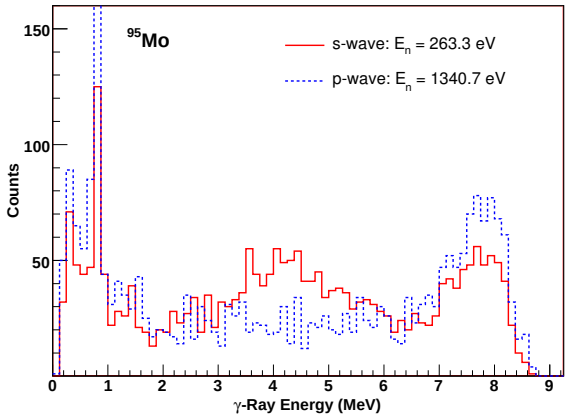

Figure 4.14: γ-Ray spectrum of parity mis-assigned resonances in ^{95}Mo.

After assigning the parities of the resonances, we are able to apply our new method

for s- and p- wave resonances separately. A superimposed plot (Fig. 4.15) shows spins of s- and p-wave resonances in the neutron energy range 100 eV to 250 eV. Our results result from separate iterations only on the positive or negative parity states. Similar plots are shown in Appendix C.

Table 4.3 shows A comparison of our results with those of reference [10]. The average multiplicities shown in the table were calculated using multiplicities $m = 2 - 7$.

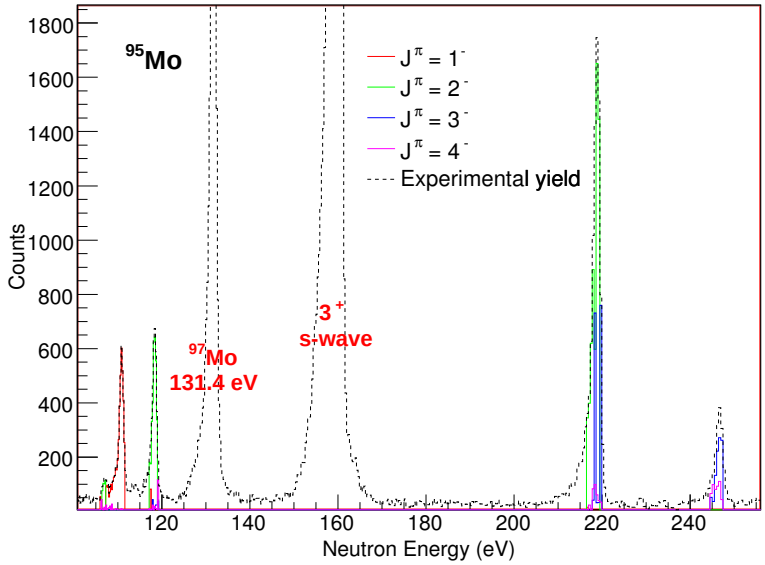

Figure 4.15: Spin Assignments of p-wave resonances in ^{95}Mo

Table 4.3: Spins of resonances for ^{95}Mo isotopes

Mughabghab				This Work				
En, eV	J	l	$g\Gamma_n$ (meV)	J	l	Prob. (%)	$\langle M_J \rangle$	Comment
44.9	3	0	222 ± 10	(3)	0	-	3.98	
110.4	1	1	0.18 ± 0.04	1	1	57.9	3.44	
117.8	2	[1]	0.26 ± 0.04	2	1	98.9	3.76	
159.5	3	0	16 ± 1	3	0	100.0	4.23	
218.3	(4)	1	2.0 ± 0.2	2	1	94.8	3.82	
245.8	(4)	[1]	0.48 ± 0.07	3	1	96.6	3.97	

Table 4.3 – continued from previous page

Mughabghab				This Work				
En, eV	J	l	$g\Gamma_n$ (meV)	J	l	Prob. (%)	$\langle M_J \rangle$	Comment
263.3	(3)	[1]	1.6 ± 0.2	2	0	99.0	3.99	
326.6	-	-	-	2	1	46.1	3.66	New
331.0	(2)	1	3.4 ± 0.8	1	1	100.0	3.54	
358.6	3	0	320 ± 60	3	0	100.0	4.28	
418.2	(2)	[1]	1.00 ± 0.14	(4)	1	87.4	3.83	
469.7	(2)	1	12 ± 1	2	0	99.1	3.97	
554.4	2	0	120 ± 20	2	0	93.2	4.04	
595.7	(3)	[1]	0.84 ± 0.20	3	1	52.4	3.75	
630.0	(4)	1	22 ± 3	2	1	75.5	3.80	
661.8	3	0	29 ± 1	3	0	97.3	4.17	
680.2	3	0	830 ± 50	3	0	100.0	4.26	
702.8	(2)	[1]	2.9 ± 0.3	-	-	-	-	Weak
708.3	(3)	[1]	13.3 ± 0.8	3	1	65.0	4.03	
745.5	(2)	1	7.9 ± 2.0	3	1	78.7	3.92	
769.8	3	0	27 ± 3	3	0	100.0	4.28	
898.4	2	0	265 ± 30	2	0	96.7	4.02	
932.1	(1)	[1]	3.6 ± 0.6	3	1	79.7	3.78	
956.5	(1)	[1]	1.5 ± 0.7	3	1	69.4	3.83	
980.7	2	0	47.0 ± 2.2	2	0	93.5	4.00	
1011.1	(4)	1	12 ± 1	3	1	67.1	3.94	
1023.8	3	0	130 ± 20	3	0	100.0	4.25	
1035.7	(4)	[1]	13 ± 1	3	0	100.0	4.32	
1059.2	(3)	[1]	9.1 ± 0.8	2	1	88.1	3.78	
1122.5	(1)	[1]	4.1 ± 0.6	(2)	1	85.0	3.85	Weak
1144.6	2	0	250 ± 50	2	0	97.7	4.02	
1170.5	(2)	[1]	22.08 ± 1.80	4	1	85.5	4.08	
1203.4	3	0	221 ± 9	3	0	100.0	4.26	
1296.9	(4)	[1]	11 ± 1	2	1	95.5	3.77	
1340.7	(2)	[0]	110 ± 8	3	1	94.9	4.03	

Table 4.3 – continued from previous page

Mughabghab				This Work				
En, eV	J	l	$g\Gamma_n$ (meV)	J	l	Prob. (%)	$\langle M_J \rangle$	Comment
1360.6	(4)	[1]	5.9 ± 0.8	3	1	96.4	3.90	
1386.7	(2)	[1]	12 ± 1	3	1	96.6	3.94	
1419.3	(3)	[0]	620 ± 70	3	0	100.0	4.23	
1437.0	(3)	[1]	15.0 ± 1.4	4	1	100.0	4.24	
1495.5	(2)	[1]	160 ± 40	2	0	99.6	3.99	Disagree
1570.0	(3)	[1]	12 ± 1	(4)	1	78.7	4.15	Weak
1589.5	(3)	[0]	300 ± 100	3	0	100.0	4.27	
1677.4	(2)	[0]	360 ± 50	3	0	100.0	4.23	
1704.1	(3)	[1]	40.4 ± 6.4	4	1	99.0	4.29	
1766.1	(3)	[0]	408 ± 46	3	0	100.0	4.25	
1788.0	(4)	[1]	55 ± 10	4	1	100.0	4.33	
1841.7	(2)	[1]	39.0 ± 5.2	3	1	83.5	3.88	
1853.3	(3)	[1]	6.4 ± 0.8	-	-	-	-	Weak
1925.1	(2)	[1]	36.0 ± 4.6	-	-	-	-	Weak
1950.2	(2)	[0]	390 ± 110	2	0	99.4	3.96	
1961.3	(3)	[1]	27.0 ± 2.8	-	-	-	-	Weak
2048.1	(2)	[0]	245 ± 100	2	0	99.7	3.91	
2130.1	(4)	[1]	61 ± 8	4	1	89.9	4.12	

4.3.9 Results for ^{94}Mo resonances

The situation was easier for ^{94}Mo, because it has only 3 spin groups and the expected separation between the parity groups is approximately 20% [59]. The difficulty is that the resonances extend up to 20 keV. The resolution of the DANCE system in this energy region is poor and the neutron flux is much lower at these higher energies. For these reasons we could not assign the spins of resonances at energies higher than about 10 keV.

Figure 4.16 shows the (m = 2 vs. m = 5) 2D scatter plot for the ^{94}Mo resonances. The three peaks correspond to the s- and p-wave resonances with spin $1/2^+$, $1/2^-$ and $3/2^-$. The clusters from the different spin groups were sufficiently separated to assign

spins. Table 4.4 compares the new results with reference [10].

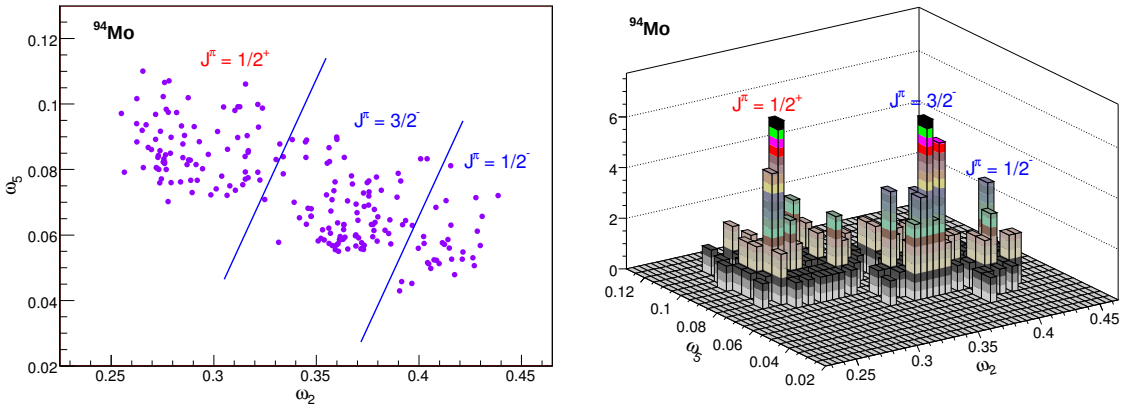

Figure 4.16: 2D scatter plot for ^{94}Mo.

As an example, Fig. 4.17 shows a graphical illustration of the results in the neutron energy range between 1 keV and 4 keV. The rest of the results are shown in Appendix D.

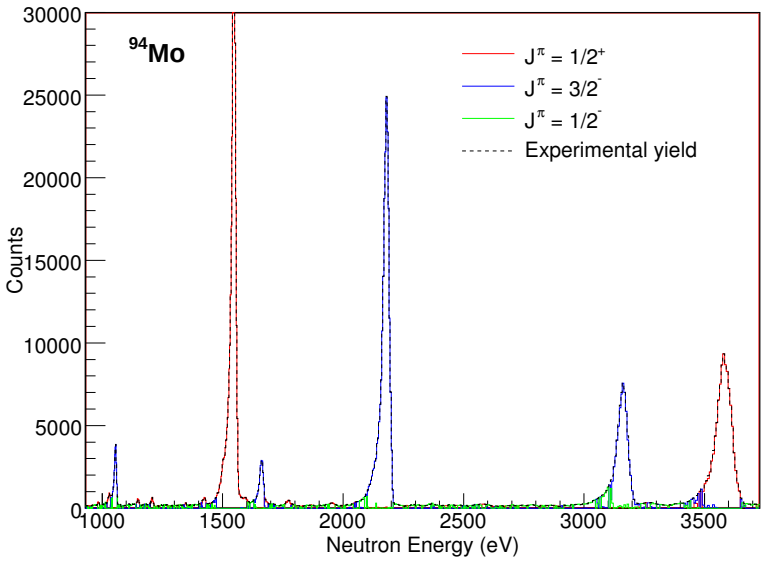

Figure 4.17: Spin assignments of neutron resonances in ^{94}Mo.

Table 4.4: The spins of resonances in ^{94}Mo.

Mughabghab				This Work				
En, eV	J	l	$g\Gamma_n$ (meV)	J	l	Prob. (%)	$\langle M_J \rangle$	Comments
108.8		[1]	0.16 ± 0.02	[3/2]	1	46.0	3.02	Spin Doublet
108.9				1/2	0	53.2	3.06	New
1051.7		[1]	6.1 ± 0.1	3/2	1	94.7	2.95	
1541.8		0	1100 ± 300	1/2	0	99.5	3.14	
1660.4		[1]	12.4 ± 1.7	3/2	1	97.3	2.98	
2178.4	3/2	1	383 ± 135	3/2	1	90.5	2.96	
3163	(3/2)	[1]	244	3/2	1	71.6	2.96	
3573	(3/2)	[1]	260	3/2	1	87.4	3.07	
3599	1/2	0	2500 ± 500	1/2	0	94.4	3.12	
4368	3/2	1	4000 ± 1000	1/2	1	51.4	2.67	Disagree
4622	1/2	[0]	511 ± 73	1/2	0	99.5	3.13	
4928	1/2	[1]	1090 ± 310	1/2	1	81.4	2.87	
5132	[3/2]	[1]	270	1/2	1	76.6	2.88	Disagree
5428	1/2	0	15300 ± 2000	1/2	0	92.6	3.08	
5454		[1]	8 ± 2	3/2	1	99.8	3.03	
5934				1/2	1	94.4	2.83	New
6407		[1]	30 ± 8	1/2	1	95.8	2.91	
6718	1/2	[0]	1000 ± 750	1/2	0	97.1	3.09	
6960		[1]	31 ± 8	1/2	1	62.5	2.88	
7128		[1]	9 ± 2	[1/2]	[1]	-	2.87	Weak
7860	-	-	-	3/2	1	64.5	3.05	Spin Doublet
7865	1/2	[0]	1000	1/2	0	61.2	3.08	
8275	[3/2]	[1]	4000	3/2	1	93.1	2.95	
8608	3/2	1	1000	3/2	1	85.3	2.93	
8660		[1]	210	3/2	1	80.6	2.93	
9590	[3/2]	[1]	1000	3/2	1	98.1	2.93	
9705	1/2	[0]	500	[1/2]	[0]	43.3	3.02	Weak
9813		[1]	350	3/2	1	95.6	2.94	

Table 4.4 – continued from previous page

Mughabghab				This Work				
En, eV	J	l	$g\Gamma_n$ (meV)	J	l	Prob. (%)	$\langle M_J \rangle$	Comments
10225	[3/2]	[1]	6000 ± 3000	3/2	1	98.8	2.96	
10540				1/2	1	75.2	2.90	New
10752	1/2	0	25000 ± 5000	3/2	[1]	95.5	2.99	Disagree
10776	[3/2]	[1]		1/2	[0]	48.4	3.02	Disagree
11400	-	-	-	[1/2]	[1]	78.2	2.91	Spin Doublet
11420	[3/2]	[1]	630	3/2	1	98.6	2.97	
11815	[3/2]	[1]	1900	3/2	1	99.1	2.97	
12205	[3/2]	[1]	440	3/2	1	94.8	2.93	
12280	(1/2)	[1]	260	1/2	1	97.1	2.90	

We have successfully assigned the spins of the ^{94}Mo resonances with the new method. We did not use the γ-ray spectrum as we did for ^{95}Mo. However, the γ-ray spectrum may be used to confirm our assignments. Figure 4.18 shows the γ-ray spectrum of s- and p-wave resonances gated on isolated strong resonances at $E_n = 1541$ eV, $E_n = 3163$ eV and $E_n = 5132$ eV.

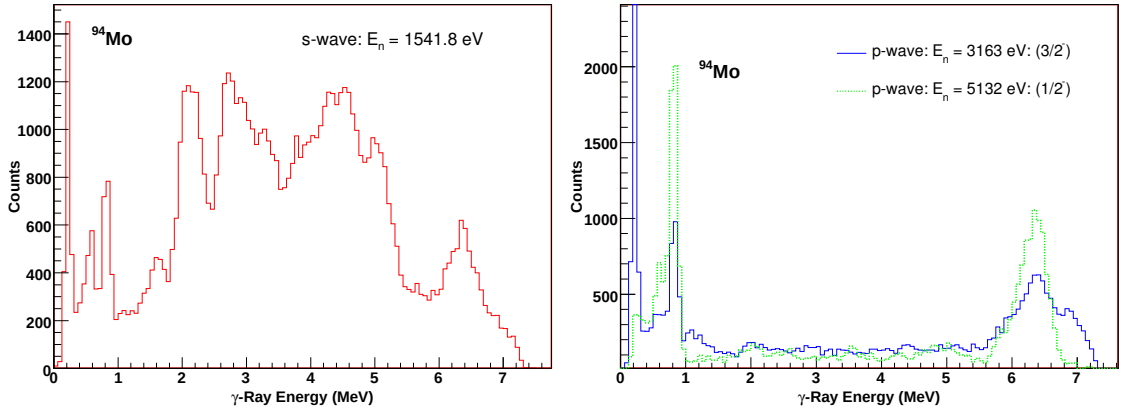

Figure 4.18: γ-Ray spectrum of s- and p-wave resonances in ^{94}Mo.

The shape of the γ-ray spectrum for s- and p-wave resonances is significantly different, as shown in Fig. 4.18. For the p-wave resonances, the intensity of primary transitions for 1/2 resonances with energies near 6.3 MeV is stronger than that for 3/2 resonances.

The p-wave resonances are usually weak, and thus the statistics of the γ-ray spectrum is not sufficient to see the intensity difference. However, the shape difference between the s- and p-wave resonances usually seems to be noticeable even for weak resonances. Figure 4.19 shows the γ-ray spectrum of a resonance at $E_n = 108.8$ eV.

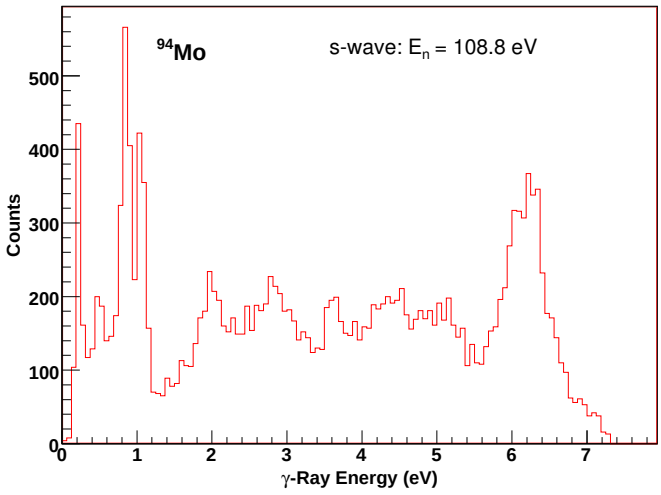

Figure 4.19: γ-Ray spectrum of a s-wave resonance at 108.8 eV.

The shape of the resonance shown in Fig. 4.19 does not resemble either a s-wave or a p-wave resonance. The hybrid shape may be observed because of background. Another possible explanation is that this is an unresolved spin doublet. Because of the resolution broadening at higher neutron energies, two resonances located close to each other are observed as spin doublets and the γ-ray spectrum of these resonances are also has a hybrid shape. In appendix E, we display the spectrum gated on several s-wave resonances that are mixed with nearby p-wave resonances.

4.4 Becvar's Method

A group at Charles university at Prague also introduced an updated method to determine spin of the neutron resonances based on the γ-ray multiplicity. At the moment, the paper on this method is in publication. So, the exact description of the method cannot be cited.

The idea of the method is briefly explained in the following: A set of quantities,

$\mu_m^{\pm}$, can be determined by the experimental yields from strong resonances whose spins are known. The $\pm$ signs stands for spin values $J = I \pm 1/2$ and the sets will be referred to as *prototypical* multiplicity distribution. Knowing sets $\mu_m^{\pm}$ together with experimental yields $y_m(E_n)$ and variances $\sigma_m^2(E_n)$ at energy E_n and multiplicity $m = m_{min}, ..., m_{max}$, one can the extract spin of the resonances. The optimum condition is determined by the minimum variance of the extracted yield corresponding to spin "+" or "−".

For the purpose of comparison, the method is applied to the same experimental data of ^{155}Gd [63]. The results are shown in Figs. 4.20-4.22. The spin of the resonances determined by two different methods were consistent in most cases. Spin $J = 1$ resonance at $E_n = 21.03eV$ and spin $J = 2$ resonance at $E_n = 6.3eV$ are chosen as prototypes.

One should keep in mind that the multiplicity distribution for resonances with the same spin can slightly fluctuate. For instance, the negative dip in the green curve and the overpredicted yield in the red curve at about 51.7 eV in the Fig. 4.21 are probably a consequence of the allowed fluctuations. The same kind of structure can be found elsewhere. On the other hand, it could also be an indication of contamination from a different isotope.

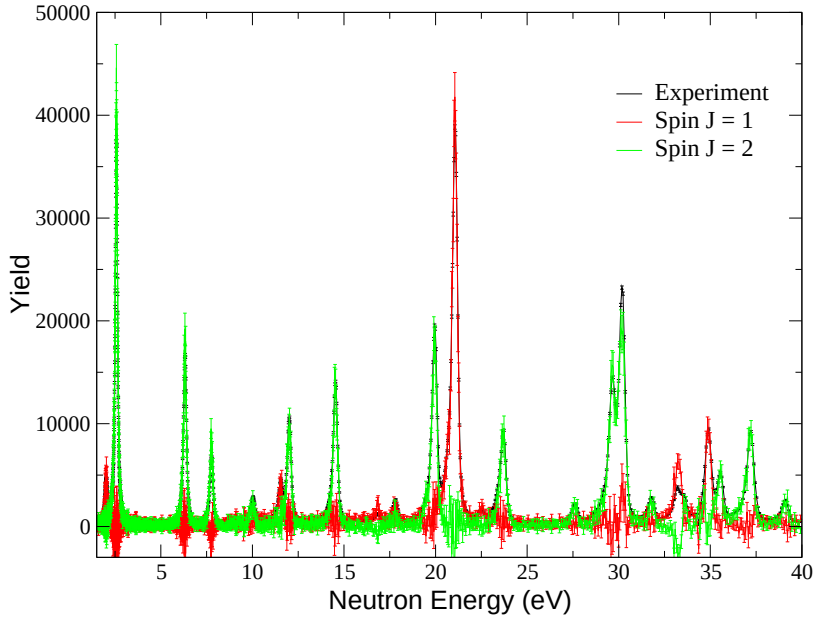

Figure 4.20: Spin of the ^{155}Gd resonances between $E_n = 1$ to 40 eV determined by the Becvar's method

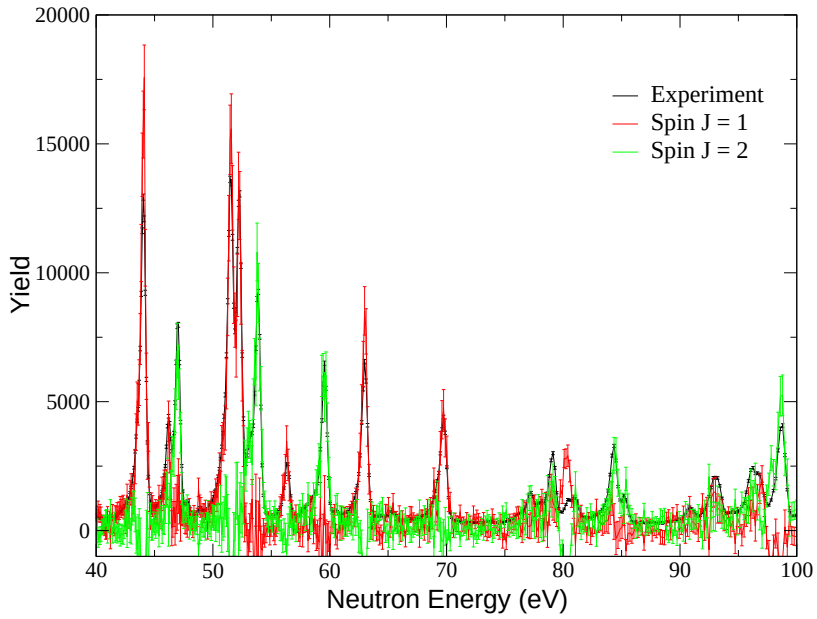

Figure 4.21: Spin of the ^{155}Gd resonances between E_n = 40 to 100 eV determined by the Becvar's method

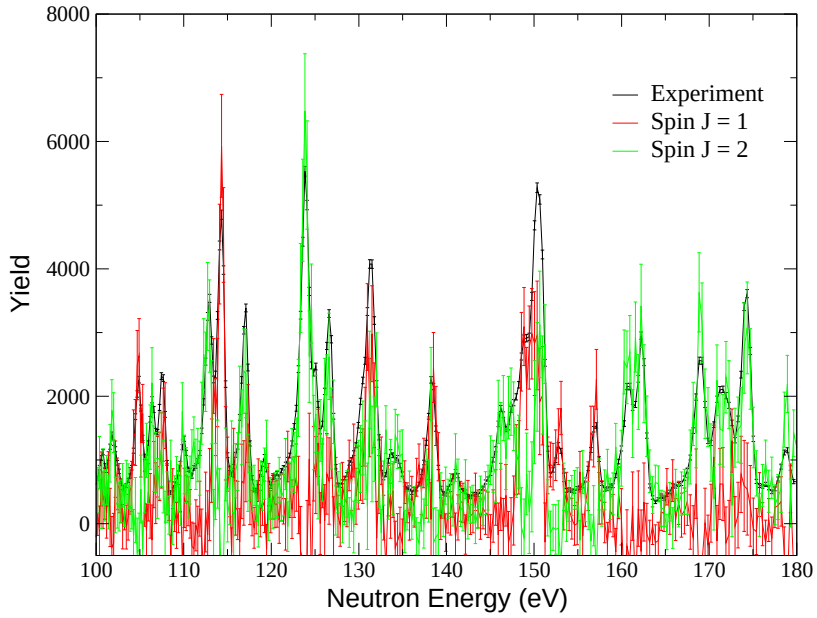

Figure 4.22: Spin of the ^{155}Gd resonances between E_n = 100 to 180 eV determined by the Becvar's method

This method was also applied to same data set of ^{94}Mo and ^{95}Mo [63]. In fact, the method works nicely if it has only two possible spin and parity groups of resonances. But, there are three possible spin and parity groups of neutron resonances in ^{94}Mo and six groups in ^{95}Mo. For this case, it would give several different ratios of deduced yields if there are more groups of resonances.

For ^{94}Mo, several combinations of prototypical resonances (such as $J^{\pi} = 1/2^{+}$ and $J^{\pi} = 1/2^{-}$ or $J^{\pi} = 1/2^{+}$ and $J^{\pi} = 3/2^{-}$ or $J^{\pi} = 1/2^{-}$ and $J^{\pi} = 3/2^{-}$) were tested and it indicates that the prototypical distributions for resonances with negative parity are very similar. As a consequence, the method assigned the parities of the resonances. The preliminary results of method agree with assignments given in Table 4.4 in almost all cases.

Chapter 5

Neutron Capture Cross Section of ^{155}Gd

In this chapter, we display the results of the neutron capture cross section measurement on ^{155}Gd. The cross-section was measured in the neutron energy range between $E_n = 2$ eV and $E_n = 10$ keV. There are several practical and theoretical interests in determining the cross sections on gadolinium isotopes. Gadolinium, the rare-earth metal of the lanthanide series of the periodic table, is an important element that has the highest absorption cross section for thermal neutrons of all of the stable isotopes. Accurate knowledge of the cross section is of considerable interest in reactor control application and in general for reactor calculations.

The clinical results of treating brain tumors with neutron capture therapy are very encouraging. In practice ^{10}B is widely used as the Neutron Capture Therapy (NCT) agent. ^{10}B undergoes the reaction ^{10}B(n,α)^{7}Li. ^{157}Gd is another nuclide that holds interesting properties of being a NCT agent. ^{155}Gd (nat.ab. 14.4 %) could be another possible alternative NCT isotope to ^{10}B besides ^{157}Gd. Because it has large thermal neutron cross-section of about 60,900 barns.

Evaluated and unevaluated Nuclear Data Libraries (NDL) [10, 64, 65] cite a large set of experimental data on the ^{155}Gd(n,γ) reaction. The resonance parameters – neutron width Γ_n and radiation width Γ_γ – that characterize the neutron capture cross-section in the resonance region were determined by transmission measurements in the 1960s and 1970s (see e.g., [66–68]). The most recent data [69] for the resonance parameters were obtained

from transmission and capture experiments at Rensselaer Polytechnic Institute (RPI) in 2006. Since there are some disagreements between the RPI results and the ENDF/B-VII.0, we were motivated to extract the resonance parameters from the DANCE experiment. The multilevel R-matrix fitting-code, SAMMY, was used to extract the parameters Γ_n, Γ_γ and the resonance energy E. The neutron widths multiplied by the spin statistical factor, $2g\Gamma_n$, were compared with the results in ENDF/B-VII.0 library and from the RPI data.

For many cases, the spin values in the nuclear data libraries were different from our values determined in Chapter 4. The spin assignments in the Atlas of Neutron Resonances [10] were mostly taken from a few experiments such as Asghar et al. [70] and Belyaev et al [71]. The spin values in the nuclear data library ENDF/B-VII were different from any of the experiments for many resonances (see Table 5.1). The experimental data in the unresolved resonance region is up to date. Our results in this energy region are in good agreement with experiments [72–75].

The new parameters allowed us to extract the s-wave neutron strength function S_0. The study of the resonance parameters and the s-wave neutron strength function is of interest in order to search for possible spin dependence of the strength function. ^{155}Gd lies in the valley of the split 4s giant resonance of the s-wave strength function.

5.1 Cross-Section Formula

The capture cross section at a particular neutron energy may be calculated by the equation:

$$\sigma_{n,\gamma}(E_n) = \frac{M}{N_A m S \varepsilon_{n,\gamma}(E_n)} \frac{N_{n,\gamma}(E_n)}{\Phi(E_n)} \tag{5.1}$$

where $N_A = 6.022 \cdot 10^{23}$ mole^{-1} is Avogadro's number, $M = 155$ g/mole is the molar mass of the ^{155}Gd isotope, $m = 1.008$ g/cm^2 is the areal density of the target, $S \approx 5.064$ cm^2 is the illuminated target area, $\varepsilon_{n,\gamma}(E_n)$ is the total efficiency for detecting capture gamma rays after applying gates on the event multiplicity and the total gamma-ray energy set around the Q-value of the reaction, $N_{n,\gamma}(E_n)$ is the number of capture events and $\Phi(E_n)$ is the neutron flux.

- The number of capture events $N_{n,\gamma}(E_n)$ will be measured by the DANCE array.

- The flux $\Phi(E_n)$ will be measured by the neutron monitors, but must be normalized to obtain the flux at the target position.
- The efficiency $\varepsilon_{n,\gamma}(E_n)$ will be estimated from the gated and ungated total γ-ray energy spectrum.

5.2 Neutron Flux Measurement

In DANCE experiments one measures the neutron flux with 3 different detectors located downstream from the array. For the cross-section calculation we used a proportional counter filled with BF_3+Ar gas and an n-type surface barrier Si detector.

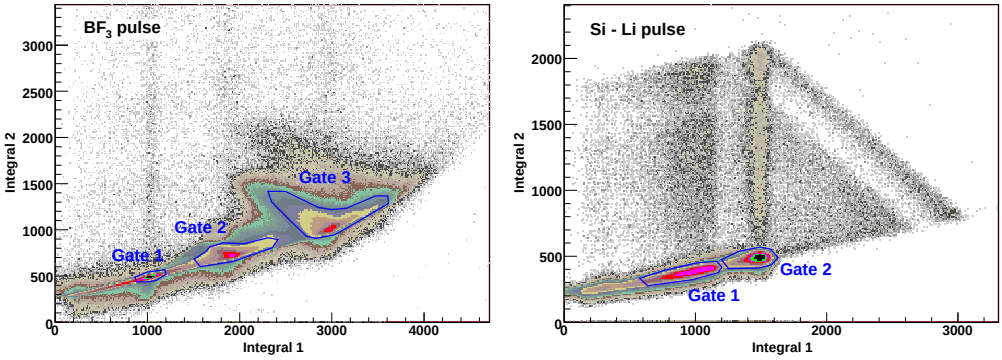

Figure 5.1: Slow vs Fast integral for the BF_3 and the ^{6}Li detectors. The blue lines gate the reaction products. (triton and alpha peaks for the Si-Li detector, ^{7}Li and α peaks for the BF_3 detector)

The BF_3 neutron monitor is positioned at 22.76 meter from the moderator and the charged particles from the ^{10}B(n,α)^{7}Li reaction were measured. The semiconductor detector consists of a ^{6}LiF target (of thickness 2 mm and size 3×4 cm^2) deposited on an 8-mm thick kapton foil and positioned in the center of the beam pipe at 45° angle approximately 22.59 meter from the neutron moderator. The Si detector was located perpendicular to the beam at a distance of 3 cm from the ^{6}Li foil. The tritons and alpha particles produced in the ^{6}Li(n,t)^{4}He reaction were measured. The neutron monitor signals were reduced in the same manner as the signals from the BaF_2 crystals, i.e., 32 points sampled at 50 ns starting 250 ns before the leading edge of the peak and 5 sequential integrals of 250 ns intervals [76]. The integral of the first 1.6 ms of the signal I_1 was determined from the sum of the first

32 points of the signal. The integral I_2 of the signal tail that followed immediately after I_1 was determined as the sum of the 5 integrals saved by the front-end data acquisition system. Figure 5.1 shows I_1 vs I_2 plots for the BF_3 and Si-Li detectors. The integrals I_1 and I_2 were used to discriminate reaction products from background and pile-up events. The event rates detected by the neutron monitors were converted to neutron fluxes using known cross sections. As an example, Figure 5.2 shows the neutron flux measured with ^{6}Li monitor for a single run.

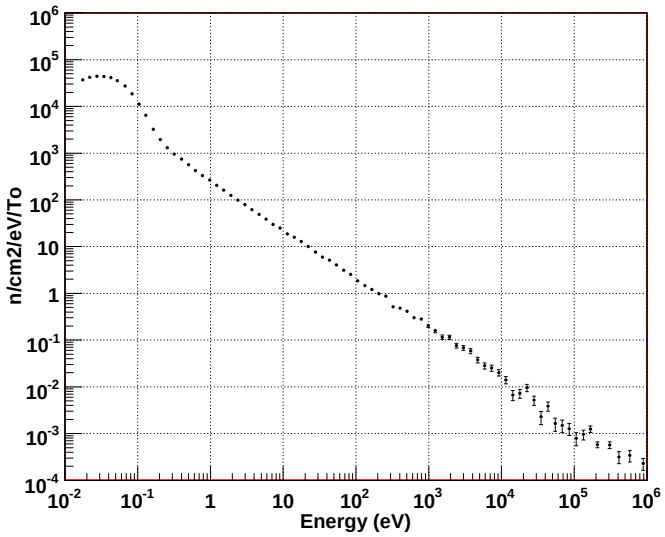

Figure 5.2: Neutron flux measured with the ^{6}Li neutron monitor for a single run.

The neutron flux measured with the ^{6}Li and the BF_3 monitors is not the same as the neutron flux at the target position in the center of the DANCE array. The reason for this is that the beam diverges with increasing distance from the last collimator in the flight path upstream of the DANCE target position. The image plate measurements determined that the beam spot at BF_3 monitor has a diameter of 1.4 cm, whereas the beam spot at the entry to the DANCE ball is approximately 1 cm in diameter. Additional measurements were performed, in order to determine the absolute flux at the target position. We used a 1-inch diameter gold target that has the same geometry as our ^{155}Gd target. The thickness of the gold target was 1 μm. The analysis of the gold data was accomplished by gating on the 4.9 eV resonance, but without any multiplicity or total γ-ray energy requirements. The background was subtracted using data directly above the 4.9 eV resonance. The result was

fitted with SAMMY where only a total normalization factor A was varied. Self shielding and Doppler broadening corrections were included in the analysis. The result obtained from the SAMMY fit was $A = 1.809$ for the ^{6}Li detector and $A = 1.709$ for the BF_3 detector. The factor A corresponds to a normalization factor . Therefore, the relation between the fluxes are :

$$\Phi(E_n) = \begin{cases} \varepsilon_{BF_3}\Phi_{BF_3}(E_n) \\ \varepsilon_{^6Li}\Phi_{^6Li}(E_n). \end{cases} \tag{5.2}$$

5.3 Efficiency Estimation

The efficiency is one of the most important characteristics of the detector system. Not all gamma rays emitted by the target and pass through the detector will produce a count. The probability that an emitted gamma ray will interact with the detector and produce a count is the efficiency of the detector.

$$\varepsilon_0 = \frac{\text{Counts in the Detector}}{\text{Total Number of Capture Events}} \tag{5.3}$$

The efficiency is determined with standard gamma ray sources whose activities are known. It is essential to know the detector response functions for γ-rays with different energies and multiplicities. GEANT4 simulations of the DANCE array were in good agreement with experiments performed with calibration sources ^{60}Co, ^{88}Y and ^{22}Na [53]. The simulation executed with mono-energetic γ-rays established that the detector efficiency is approximately constant at about 86% (Fig. 5.3). With this assumption, for two γ-rays the probability to detect at least one of the two γ-rays is approximately 98%.

To understand cascade efficiency, consider a simple nucleus that has equal probabilities: $\omega_1 = \omega_2 = 0.5$, of emitting one or two γ-rays and zero probability to emit three or more γ-rays in the cascade. For this simple nucleus, the total efficiency is calculated as

$$\varepsilon_0 = 0.86\omega_1 + 0.98\omega_2 = 0.92 \tag{5.4}$$

Since the γ-ray cascade of real nuclei and the detector response is much more complicated, a simulation is the ideal way to estimate the efficiency ε_0. The γ-ray cascade of the ^{155}Gd isotope was simulated using the Monte Carlo statistical code DICEBOX [30]; a detailed description of the simulation is given in Chapter 6.

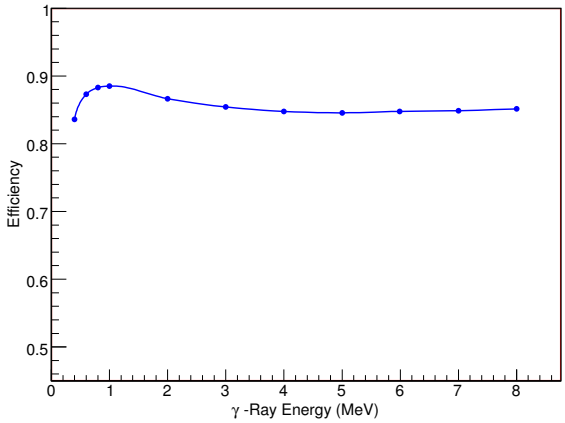

Figure 5.3: The simulated efficiency as a function of a single γ-ray. A 150 keV threshold was applied on each crystal.

The total number of capture events is estimated as

$$N_{total} = \frac{N_{ungated}}{\varepsilon_0}, \tag{5.5}$$

where $N_{ungated}$ is total number of counts in the experimental spectra with no gates applied and $\varepsilon_0 \approx 0.97$ is total efficiency estimated by the simulation.

For the DANCE experiments, several gates are applied to reduce background (see Chapter 3). A narrow total γ-ray energy gate will reduce the background but also reduce counting statistics. Therefore the appropriate gates are determined by signal-to-noise ratio analysis. The cluster multiplicity $m \geq 3$ and total γ-ray energy $6.5 < E_{total} < 8.6$ MeV gates are used for the cross section calculations.

The "gated efficiency" $\varepsilon_{n,\gamma}$ is calculated by the ratio of the counts within the gates and the ungated counts corrected by Eq (5.5):

$$\varepsilon_{n,\gamma} = \frac{\sum_{m=3}^{7} N_{gated}}{N_{ungated}} \varepsilon_0. \tag{5.6}$$

Using the counts in the strong resonances at $E_n = 21.03$ eV and $E_n = 14.51$ eV in Eq. (5.6), the efficiency of capture cascade detection $\varepsilon_{n,\gamma}$ was determined to be 37.5(2)%.

5.4 Cross-Section

We have determined all of the quantities in Eq. (5.1) and are able to extract the ^{155}Gd(n,γ) absolute cross-section. The cross-section is calculated from the counts in each neutron energy bin and the uncertainty is calculated by Eq. (3.1). Figure 5.4 compares the calculation with results from other experiments and the ENDF/B-VII.0 library. The corrections for experimental effects such as Doppler broadening etc. are applied to ENDF parameters in order to compare with the DANCE data.

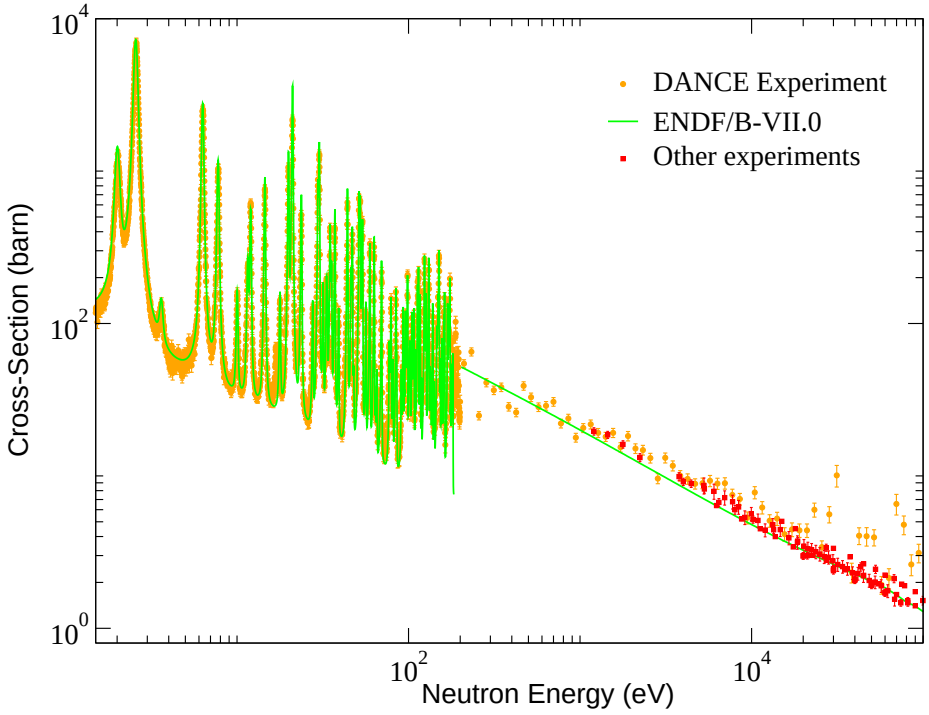

Figure 5.4: Cross section of the ^{155}Gd(n,γ)^{156}Gd reaction. The orange dots are the results of the DANCE experiment, the green line represents the ENDF/B-VII.0 data, and the red marks the other experiments.

The capture cross-section that we have obtained is overall in good agreement with other experiments and the ENDF data. Exact fitting of the resonances to obtain parameters is described in the following section. The other experiments at unresolved resonance region shown in Fig. 5.4 consist of several experiments that are listed in the EXFOR data library [64].

5.5 Fitting Procedure with SAMMY

The fitting procedure explained below is exactly same technique used in the RPI experiments [77]. SAMMY is a computer code used in the analysis and evaluation of experimental cross-section data in the resolved (RRR) and unresolved (URR) resonance region.

Statistical models predict that the radiation width Γ_γ should not vary much for resonances within a specific isotope, while the neutron width Γ_n can vary considerably. Insensitive parameters can occur when utilizing shape-fitting methods on resonances that are not well resolved. In such cases, an area analysis method provides a measure of the sensitivity. The area under an isolated optically thin ($N\sigma_0 << 1$) resonance in the capture yield is defined as

$$A \sim g\frac{\Gamma_\gamma \Gamma_n}{\Gamma_\gamma + \Gamma_n}, \tag{5.7}$$

where A is the capture yield area, N is the number density of the target material (atoms/barn), and σ_0 is the peak total cross section given as:

$$\sigma_0 = 4\pi\lambda\!\!\!^{-2}_0 \frac{a\Gamma_n}{\Gamma}, \tag{5.8}$$

where $\lambda\!\!\!^{-}_0$ is the reduced neutron wavelength at the resonance energy E_0. When Γ_n is much greater or smaller than Γ_γ, then

$$\begin{aligned} A &\sim g\Gamma_\gamma \quad \text{for} \quad \Gamma_n >> \Gamma_\gamma \\ A &\sim g\Gamma_n \quad \text{for} \quad \Gamma_\gamma >> \Gamma_n. \end{aligned} \tag{5.9}$$

When resonances are well resolved, such as those at low energy (few eV), SAMMY should be able to extract Γ_γ from shape fitting procedures. However, difficulties arise at higher energies when the resonance shape is dominated by Doppler and resolution broadening. Optically thin resonances that are dominated by capture ($\Gamma_\gamma >> \Gamma_n$) show a lack of sensitivity to the radiation width Γ_γ.

This is readily apparent from Eq. (5.9). Therefore, when dealing with capture resonance that has strong radiative channel, we cannot expect SAMMY to be sensitive to Γ_γ. The Bayesian analysis used by SAMMY should automatically make sure that insensitive parameters will not vary. However, in some cases, SAMMY varied insensitive parameters considerably.

The above area analysis equations enabled the development of a method that was used to decide whether SAMMY was considered to be sensitive to Γ_γ or not. The method was based upon a radiation width sensitivity factor, which is defined by taking the following ratio:

$$S \equiv \frac{\Gamma_\gamma}{\Gamma_n}. \tag{5.10}$$

The first step in the fitting method was the determination of the radiation width sensitivity factor for each resonance in the energy region of interest. The values for the resonance parameters in Eq. 5.10 were taken from ENDF-B/VII.0. It was decided that when $S > 10$ the resonance may be considered insensitive to Γ_γ and SAMMY was only allowed to solve for Γ_n. When $S < 10$ then SAMMY is assumed to be sensitive to Γ_γ and is permitted to solve for both Γ_γ and Γ_n simultaneously. Most of the resonances in ^{155}Gd were insensitive to Γ_γ.

For resonances deemed insensitive to Γ_γ, the value of the radiation width was fixed to an average value $\langle\Gamma_\gamma\rangle$. The average radiation width for ^{155}Gd isotope was given as 109.8 meV in ENDF-B/VII.0 library. The average width given in the RIPL-II library was 108 ± 10 and the Mughabghab [10] gives 110 meV. The statistical model (see Chapter 3) predicts the average radiation width is dependent from initial (capture) and final (ground) states of the compound nuclei which parametrize with spin, parity, and energy of the states. Hence, we assume the average widths for resonances with different spin would be different. In other words, we calculated two average Γ_γ corresponding to resonances with spin $J = 1$ and $J = 2$. This average value for a particular spin resonance was calculated by averaging all of the sensitive and low energy Γ_γ parameters with same spin. It should be noted that the fitting method is an iterative process. This stemmed from the fact that the average radiation width changed as the sensitive parameters changed during subsequent SAMMY runs. Several SAMMY runs were needed in order to ensure convergence between the sensitive parameters and the average radiation width $\langle\Gamma_\gamma\rangle$. In other words, SAMMY runs were repeated until the value of the sensitive parameters did not change, which would prevent the average radiation width from also changing. This lack of change is what is meant by the term convergence. All sensitivity factors with values greater than 10 are shaded for emphasis. In these particular resonances SAMMY will be considered insensitive to Γ_γ except if the resonance is optically thick or at low energy. The second step in the fitting method was to let SAMMY vary all resonance parameters established in step one. Close attention was

paid to see if SAMMY changed the average radiation width values $\langle\Gamma_\gamma\rangle$ that were calculated in step one for insensitive parameters. It was observed that SAMMY changed these values by less than 5%, ensuring that these were very good initial guesses and that SAMMY was relatively insensitive to these parameters. If these parameters were sensitive then SAMMY would have forced them to change appreciably from the average radiation width $\langle\Gamma_\gamma\rangle$ used as the initial guess. In those cases in which SAMMY did change the radiation width greatly with respect to the average (i.e., greater than two standard deviations) then it was fixed to the ENDF value and not allowed to vary any longer. The values arising from this second step in the fitting method were considered to be the final parameters.

5.6 Cross Section in the Resonance Region

The epithermal resonance data were examined over the energy range of 1 eV to 200 eV with the use of SAMMY. The fit results in the neutron energy range 1 eV to 9 eV are shown in the following figures as an example. Similar plots are shown in Appendix F for the entire resonance region.

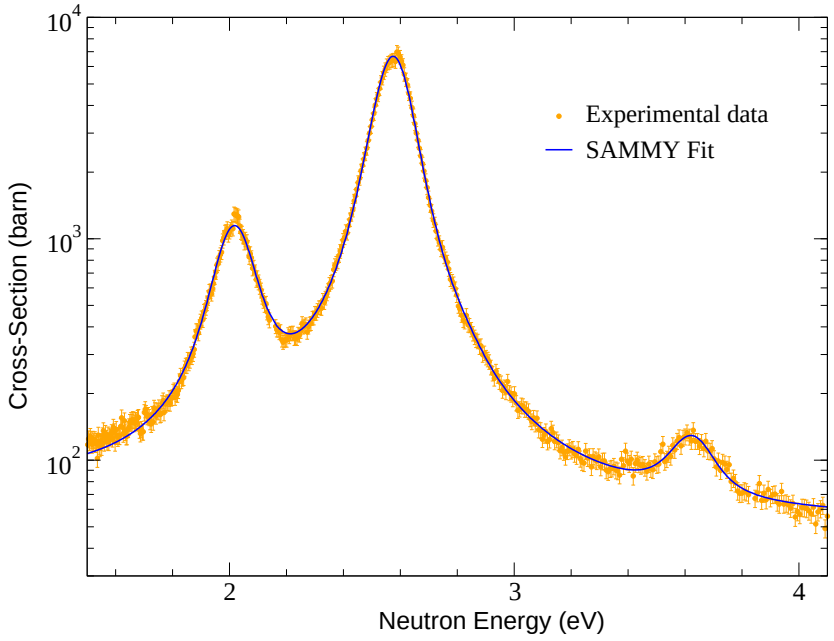

Figure 5.5: Resonances between 1 eV and 4 eV (Fit with SAMMY).

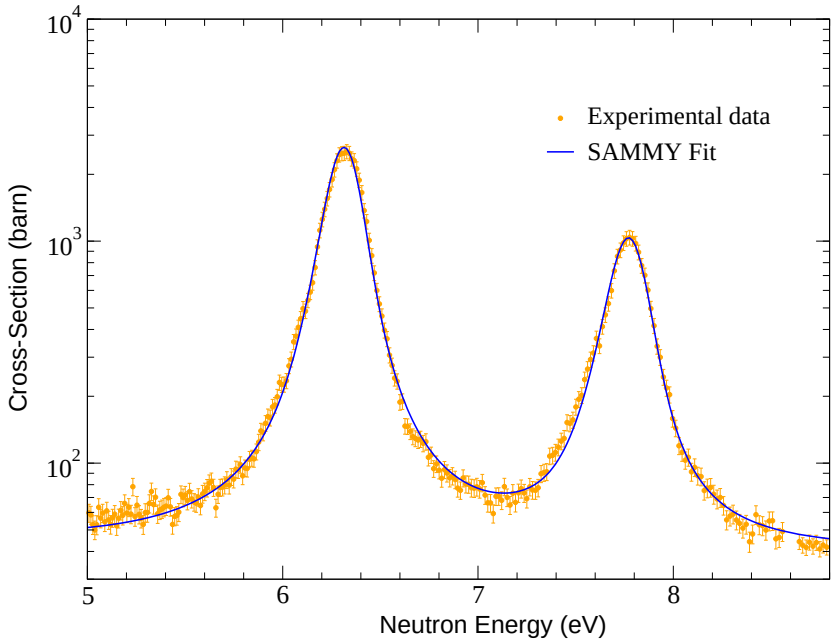

Figure 5.6: Resonances between 4 eV and 9 eV (Fit with SAMMY).

The radiation and neutron widths given by the fit are presented in Table 5.1 along with evaluated parameters from ENDF/B-VII.0 and the RPI data [69]. Note that the errors on the resonance parameters are purely statistical errors.

All resonance spins in the RPI experiment were the same as those assigned in ENDF/B-VI. But, for many resonances, the spin we have determined in Chapter 4 was different from ENDF. Therefore, we compared $2g\Gamma_n$ values instead of Γ_n.

Table 5.1: The resonances parameters for ^{155}Gd isotopes

ENDF-B VII				This Work				RPI, (2006)		
En, eV	J	$2g\Gamma_n$ (meV)	Γ_γ (meV)	En, eV	J	$2g\Gamma_n$ (meV)	Γ_γ (meV)	En, eV	$2g\Gamma_n$ (meV)	Γ_γ (meV)
2.008±0.01	1	0.278±0.003	110±1	2.02	1	0.25±0.01	122±2	2.012±0.0002	0.3±0.01	128±1
2.568±0.13	2	2.18±0.02	111±1	2.58	2	1.99±0.02	109±2	2.5729±0.0003	2.138±0.003	107.1±4
3.616±0.006	1	0.033±0.002	130±17	3.62	1	0.039±0.002	130±0	3.616±0.003	0.038±0.02	130±0
6.3±0.02	2	2.5±0.15	114±7	6.31	2	2.76±0.03	120±3	6.3057±0.0002	2.75±0.01	108.8±1
7.75±0.01	2	1.4±0.05	124±4	7.76	2	1.41±0.02	121±4	7.7477±0.0004	1.45±0.01	109±1
10.01±0.01	2	0.21±0.02	115±20	10.02	2	0.26±0.01	115±0	9.991±0.003	0.25±0.04	110±20
11.53±0.01	1	0.45±0.03	125±23	11.53	1	0.47±0.01	125±0	11.508±0.001	0.58±0.08	120±40
11.99±0.01	2	1.1±0.05	112±11	11.99	2	1.38±0.02	115±5	11.964±0.008	1.4±0.04	130±20
14.51±0.01	1	2.4±0.2	103±10	14.5	2	2.67±0.04	117±5	14.476±0.009	2.57±0.09	130±10
17.77±0.02	2	0.49±0.03	120±25	17.76	2	0.54±0.02	120±0	17.729±0.005	0.59±0.04	130±40
19.92±0.02	2	5.7±0.4	104±16	19.91	2	5.92±0.1	124±7	19.86±0.01	5.625±0.1	118±6
21.03±0.04	2	19.5±0.9	98±6	21.01	1	14.3±0.3	128±4	20.97±0.02	14.5±0.5	140±20
23.67±0.04	2	3.9±0.1	120±15	23.62	2	3.81±0.06	138±6	23.6±0.02	3.64±0.08	140±10
27.57±0.05	1	0.84±0.02	125±20	27.55	2	0.91±0.02	125±0	27.509±0.002	0.982±0.04	140±20
29.58±0.05	2	5.4±0.4	108±22	29.54	2	6.8±0.2	135±13	29.5±0.02	6±0.1	113±2
30.1±0.06	2	13±3	100±11	30.1	2	12.8±0.2	140±15	30.05±0.02	13.9±0.5	130±10
31.72±0.06	2	1.4±0.04	118±20	31.69	2	1.32±0.03	121±8	31.66±0.01	1.55±0.07	140±20
33.14±0.07	1	1.4±0.3	109.8±0	33.09	1	1.53±0.07	129±13	33.1±0.2	1.2±0.6	110±30

Table 5.1 – continued from previous page

ENDF-B VII				This Work				RPI, (2006)		
En, eV	J	$2g\Gamma_n$ (meV)	Γ_γ (meV)	En, eV	J	$2g\Gamma_n$ (meV)	Γ_γ (meV)	En, eV	$2g\Gamma_n$ (meV)	Γ_γ (meV)
33.51±0.07	1	1.2±0.3	115±35	33.49	2	1.21±0.04	130±30	33.4±0.3	0.75±3	120±90
34.83±0.07	1	4.6±0.3	152±23	34.8	1	4.2±0.2	120±6	34.73±0.02	5.1±0.2	131±4
35.47±0.07	2	2.3±0.12	118±23	35.43	2	2.43±0.07	145±8	35.39±0.01	2.71±0.06	140±10
37.12±0.08	1	6.3±0.2	101±20	37.11	2	5.93±0.09	144±6	37.066±0.003	6.2±0.03	139±6
39±0.08	2	1.3±0.2	118±23	38.98	2	1.48±0.04	127±15	38.93±0.01	1.56±0.07	130±60
43.92±0.1	1	13±1	136±9	43.89	1	14±0.3	151±12	43.83±0.07	13±9	140±90
46.1±0.1	2	2.8±0.2	126±20	46.03	1	2.6±0.1	131±8	45.98±0.02	2.9±0.1	128±6
46.87±0.1	2	6.7±0.3	100±12	46.86	2	6.67±0.01	132±10	46.79±0.02	12.75±0.4	140±30
47.73±0.11	1	0.49±0.04	109.8±0	47.67	2	0.4±0.03	118±11	47.628±0.006	0.29±0.03	107±10
51.38±0.11	1	14±0.7	109.8±0	51.34	1	16.4±0.7	147±18	51.25±0.03	15.2±0.6	130±30
52.13±0.12	1	14.6±0.5	115±39	52.09	1	14.4±0.8	149±13	52.01±0.03	15.7±0.8	140±20
53.03±0.08	2	1.7±0.06	109.8±0	53.01	2	1.4±0.1	119±11	52.89±0.02	1.5±0.2	80±30
53.74±0.08	2	9.6±0.7	92±20	53.68	2	10.1±0.3	116±7	53.62±0.02	10.9±0.2	140±30
56.22±0.08	2	2.7±0.2	120±18	56.16	1	3±0.1	129±12	56.12±0.01	3.1±0.1	120±40
59.32±0.09	2	8.3±0.2	129±19	59.35	2	9.6±0.2	154±25	59.3±0.01	8.6±0.4	140±40
62.84±0.09	2	10±0.4	90±15	62.77	1	10.9±0.4	126±9	62.73±0.02	10.6±0.5	150±30
64.09±0.1	2	0.32±0.04	109.8±0	64.23	2	0.26±0.01	115±11	64.028±0.006	0.61±0.05	110±40
65.2±0.11	1	1±0.2	109.8±0	65.1	1	0.75±0.04	117±11	66.4±0.5	0.4±0.4	120±10
69.4±0.1	2	7.9±0.3	109.8±0	69.53	1	8.33±0.04	98±8	69.4±0.1	15±5	100±100
77±0.1	2	2±0.1	109.8±0	76.88	2	2.5±0.1	130±13	76.85±0.01	3.7±0.3	110±60

Table 5.1 – continued from previous page

ENDF-B VII				This Work				RPI, (2006)		
En, eV	J	$2g\Gamma_n$ (meV)	Γ_γ (meV)	En, eV	J	$2g\Gamma_n$ (meV)	Γ_γ (meV)	En, eV	$2g\Gamma_n$ (meV)	Γ_γ (meV)
77.8±0.1	1	0.9±0.05	109.8±0	77.69	1	1.2±0.2	119±10	77.63±0.01	0.7±0.1	110±20
78.8±0.1	2	5.3±0.5	109.8±0	78.81	2	5.5±0.2	116±11	78.75±0.06	10±1	110±30
80.05±0.12	2	0.39±0.14	109.8±0	80.17	1	0.21±0.03	110±10	80±1	0±3	112±4
80.9±0.1	1	1.8±0.2	109.8±0	80.77	2	1.81±0.08	121±11	80.9±0.3	1.08±0.08	110±30
84.2±0.1	1	6.9±0.2	109.8±0	84.01	2	7.6±0.2	119±11	83.97±0.02	7.7±0.1	120±40
85±0.1	1	2.3±0.12	109.8±0	84.95	2	2.6±0.1	126±10	84.91±0.01	1.65±0.3	110±40
90.5±0.13	2	1.6±0.06	109.8±0	90.54	1	1.7±0.2	120±10	90.51±0.02	3.1±0.2	110±90
92.5±0.15	2	2.7±0.29	109.8±0	92.38	1	2.6±0.3	114±11	92.47±0.02	2.67±0.06	110±20
92.8±0.2	2	3.9±0.36	109.8±0	92.91	2	5.4±0.3	122±12	92.9±0.03	4.35±0.07	110±50
94.1±0.15	2	0.68±0.05	109.8±0	94.22	1	0.51±0.06	110±11	93.99±0.01	0.8±0.1	110±40
95.7±0.2	2	4.8±0.33	109.8±0	95.72	2	4.8±0.2	132±12	95.7±0.03	8.9±0.4	110±50
96.6±0.2	1	4.7±0.31	109.8±0	96.43	1	4.5±0.4	122±11	96.4±0.2	2.8±0.7	110±50
98.3±0.2	1	13±0.39	109.8±0	98.34	2	13.5±0.4	132±10	98.3±0.03	8.8±0.4	150±20
100.2±0.1	1	1.6±0.2	109.8±0	100.3	2	1.4±0.1	109±11	99.9±0.1	1.9±0.2	110±10
101.4±0.1	2	3.4±0.3	109.8±0	101.4	2	3±0.2	116±11	101.42±0.02	2.6±0.2	140±30
102.1±0.1	1	1.3±0.2	109.8±0	102.1	1	1.5±0.2	111±11	102.03±0.03	1.14±0.6	110±50
104.4±0.1	1	6.8±0.8	109.8±0	104.5	1	6.6±0.4	130±11	104.36±0.09	3.7±0.9	110±80
105.9±0.1	1	4.6±0.4	109.8±0	106	2	4.7±0.3	116±11	105.8±0.1	4.5±0.8	140±20
107.1±0.1	2	7.8±0.6	109.8±0	107.1	1	8±0.5	109±10	107.14±0.04	11.2±2.5	110±80
109.6±0.1	1	3.5±0.3	109.8±0	109.6	2	4±0.2	128±12	109.37±0.02	5.5±0.4	115±2

Table 5.1 – continued from previous page

ENDF-B VII				This Work				RPI, (2006)		
En, eV	J	$2g\Gamma_n$ (meV)	Γ_γ (meV)	En, eV	J	$2g\Gamma_n$ (meV)	Γ_γ (meV)	En, eV	$2g\Gamma_n$ (meV)	Γ_γ (meV)
112.4±0.04	2	11.3±1.5	84±10	112.4	2	13.3±0.5	100±9	112.4±0.04	11.4±0.3	90±70
113.8±0.2	2	19±3	67±12	113.9	1	22±2	90±7	113.81±0.05	25±1.2	130±20
116.5±0.2	1	13±1.7	116±94	116.6	2	13.8±0.4	126±12	116.56±0.06	15.7±0.6	120±80
118.6±0.2	2	2.5±0.2	109.8±0	118.8	2	3.6±0.2	126±12	118.66±0.02	3.1±0.5	110±50
123.4±0.2	1	27±4.3	159±65	123.4	2	30.2±0.9	195±30	123.35±0.05	30±4.5	200±100
124.4±0.2	2	8.3±0.9	109.8±0	124.5	2	7.8±0.5	120±11	124.49±0.03	5±1.2	120±20
126±0.2	1	15.4±2.1	109.8±0	126.1	2	16.5±0.6	126±12	126.11±0.02	10.9±0.3	110±60
128.6±0.2	2	1.4±0.17	109.8±0	128.9	1	1±0.16	111±11	128.53±0.02	2.1±0.3	110±30
129.8±0.2	2	3.2±0.53	109.8±0	129.8	2	5.7±0.4	115±11	129.82±0.01	4.2±0.4	110±40
130.8±0.2	1	36.4±5.7	109.8±0	130.9	1	33.2±2	139±23	130.79±0.01	16.5±2.2	150±30
133±0.2	1	2.8±0.4	109.8±0	133.1	2	3.9±0.3	121±12	133.04±0.01	4±0.3	140±20
133.8±0.2	2	2.9±0.5	109.8±0	133.9	1	3.1±0.4	108±11	133.95±0.01	4.2±0.3	110±30
134.7±0.2	2	1.1±0.2	109.8±0	134.6	2	1.1±0.1	115±11	135.13±0.02	2.4±0.2	110±60
137.8±0.2	1	16±1.5	109.8±0	137.8	2	12.8±0.4	135±11	137.99±0.08	67.5±22.5	120±80
140.4±0.2	1	3.1±0.34	109.8±0	140.5	1	2.7±0.3	108±10	140.55±0.05	3.7±0.2	130±10
141.4±0.2	2	1.3±0.21	109.8±0	141.3	2	1.2±0.1	112±11	141.3±0.01	2.1±0.1	120±10
145.6±0.2	2	7.7±0.7	109.8±0	145.6	2	8.2±0.4	122±11	145.66±0.01	8.1±0.4	150±20
146.9±0.2	2	4.7±0.6	109.8±0	146.9	2	5.8±0.4	113±11	147.02±0.01	6.6±0.3	130±10
148.2±0.2	2	12±1.4	109.8±0	148.2	1	12±1	115±11	148.4±0.3	10.7±1.1	110±10
149.6±0.2	1	25±7.2	109.8±0	149.5	1	24±3	116±11	149.53±0.03	27±1.5	110±40

Table 5.1 – continued from previous page

ENDF-B VII				This Work				RPI, (2006)		
En, eV	J	$2g\Gamma_n$ (meV)	Γ_γ (meV)	En, eV	J	$2g\Gamma_n$ (meV)	Γ_γ (meV)	En, eV	$2g\Gamma_n$ (meV)	Γ_γ (meV)
150.2±0.2	2	31±11	109.8±0	150.2	2	32±2	118±11	150.37±0.04	100±37.5	110±40
152.2±0.2	1	6±0.5	109.8±0	152.2	1	6.9±0.5	116±11	152.27±0.01	4.6±0.7	150±40
154±0.2	2	1.4±0.2	109.8±0	154.2	2	0.84±0.06	112±11	153.8±0.05	1.4±0.3	160±30
156.3±0.2	2	9.6±0.8	109.8±0	156.3	1	11±0.7	117±10	156.4±0.1	37.5±12.5	110±80
160.1±0.2	2	12±1.3	109.8±0	160.1	2	14.4±0.7	118±11	160.03±0.07	12.9±0.6	110±50
161.6±0.2	2	25±3.2	109.8±0	161.6	2	24±1	115±9	161.57±0.08	27±1	150±20
168.3±0.2	1	22.6±2.4	109.8±0	168.3	2	25.5±0.9	142±12	168.2±0.09	23±3	123±6
170.3±0.2	2	10.4±1.5	109.8±0	170.2	1	10±0.9	118±11	170.2±0.1	10±1.25	80±30
171.4±0.2	2	11.5±1.6	109.8±0	171.4	2	9±0.6	120±12	171.6±0.1	22.5±1.25	110±60
173.5±0.2	2	41±5	109.8±0	173.6	2	42±2	133±12	173.5±0.1	41.2±2.5	110±80
175.6±0.2	2	2.6±0.29	109.8±0	175.2	2	1.8±0.2	114±11	175.46±0.05	5.2±0.7	110±40
178±0.2	1	7.3±0.7	109.8±0	178	2	6.4±0.4	113±11	177.99±0.02	9.7±1.5	130±10
180.4±0.3	1	11±1.1	109.8±0	180.3	2	13.7±0.6	125±11	180.34±0.04	7.3±0.2	110±40
183.3±0.3	1	8±0.8	109.8±0	183.1	1	8.8±0.9	121±11	183.2±0.05	1.3±0.2	110±40

5.7 Analysis of the Resonance Parameters

One-by-one comparison of the neutron widths, $2g\Gamma_n$, are shown in Fig. 5.7. This type of plot is useful to see if there are any systematic discrepancy between the parameters.

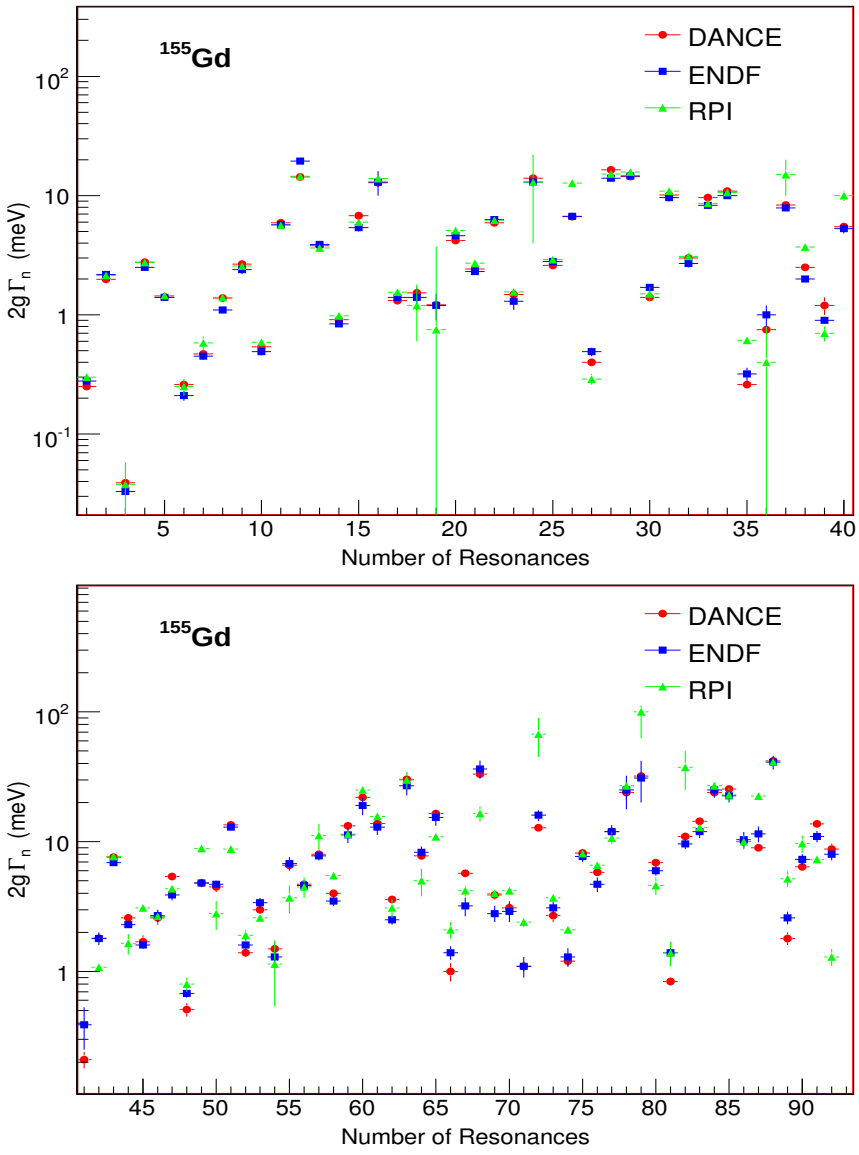

Figure 5.7: Comparison of the $2g\Gamma_n$ values.

It may be concluded that the resonance parameters determined from the DANCE experiment are overall in good agreement with the previous data. However, a few things

can be noticed from the comparison shown in the Fig. 5.7 and Table 5.1. The energy for each resonance changes very little when compared with the energies quoted from the other sources.

A large majority of the DANCE values of Γ_γ appear to be larger than previously published average values. The larger values of Γ_γ in this work may be the result of the insensitivity explained in the previous section. The bigger Γ_γ than the previous average is also observed in the RPI experiments for many resonances. As a consequence, both DANCE and RPI parameters give larger average radiation widths; $\langle\Gamma_\gamma\rangle^{(\mathrm{DANCE})} = 123 \pm 12$ meV and $\langle\Gamma_\gamma\rangle^{(\mathrm{RPI})} = 122 \pm 18$ meV. The average radiation width given in nuclear data libraries were approximately 110 meV. However, the systematic uncertainties of our parameters are relatively large and we may assume that the averages are in agreement.

The neutron widths are comparable to those previously published except for a few cases. There were large discrepancy between RPI and ENDF parameters at 137.7 eV and 150.2 eV; the DANCE results are consistent with the ENDF parameters. The reduced neutron width is important to accurately determine neutron strength function S_0. Figure 5.8 shows the cumulative reduced neutron width as a function of neutron energy.

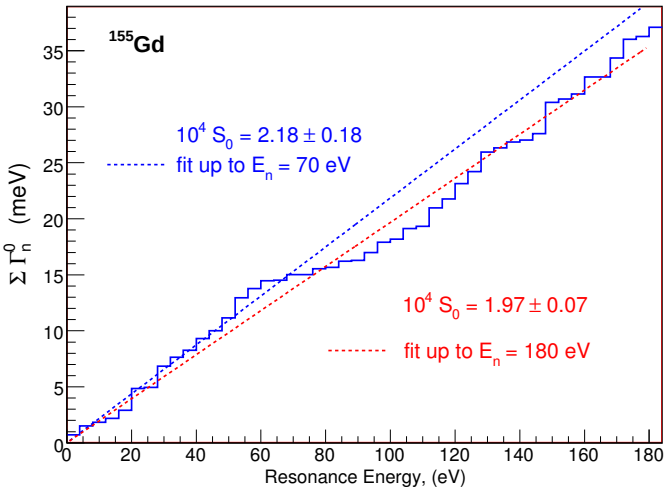

Figure 5.8: Cumulative reduced neutron width versus resonance energy.

The slope of the plot determines the s-wave neutron strength function, S_0. A least square fit of the data up to $E_n = 70$ eV determined the strength function as $10^4 S_0 = 2.18 \pm 0.18$ and the fit up to $E_n = 180$ eV gives $10^4 S_0 = 1.97 \pm 0.07$. The error on the

strength function is estimated to be $\sqrt{2/N}S_0$.

The reduced neutron width distribution should agree with the Porter-Thomas distribution (Eq. 2.19), which is χ^2-distribution with one degree of freedom. The $\nu = 1$ distribution is confirmed for many nuclei by neutron width analysis. However, deviation from the expected distribution is observed for some nuclei including ^{155}Gd [78]. The $\nu > 1$ cases are referred as non-statistical effects. But, no conclusion can be made without missing level corrections. As we can see from Fig. 5.8 and 4.10 there might some missing resonances above 70 eV. A detailed analysis [9] is required for further conclusions.

Chapter 6

Photon Strength Functions in ^{156,157,159}Gd isotopes

In Chapter 2, we introduced theoretical models of the Photon Strength Function (PSF) and the Level Density (LD) within the framework of the statistical model of nuclear reactions. In this chapter we shall discuss an experimental method to determine the PSF. The majority of experimental results, such as the Lorentzian parameters of the giant dipole resonance are gathered from the analysis of photo-nuclear reaction cross sections. However, such experiments cannot provide any information about the γ-ray strength function below the particle separation threshold. Information about the low energy tail of the PSF has been primarily obtained by neutron capture experiments.

Resonance-like structures in the PSF below the particle threshold were observed in many experiments. In recent years, several direct and indirect methods were introduced to study the PSFs at low energy. For example, the two-step γ-cascade after thermal neutron capture provides information about the sum of electric and magnetic dipole transition strengths. Experiments on more than 50 different nuclei ranging from ^{28}Al to ^{200}Hg were performed at the Frank Laboratory of Neutron Physics in Dubna and at the Rez facility in Prague [79]; they provide information concerning the properties of the PSFs at low energy.

A group at Oslo Cyclotron Laboratory performed a series of experiments using pick-up (^{3}He,$\alpha\gamma$) and inelastic (^{3}He,^{3}He$'\gamma$) reactions. The sequential extraction procedure, so called "Oslo Method", simultaneously extracts the LD and PSF.

The low energy enhancement of the PSF is also studied directly by Nuclear

Resonance Fluorescence (Photon-Scattering) experiments at the ELBE accelerator of the Forschungszentrum Rossendorf near Dresden, Germany, and at the High Intensity γ-Ray Source (HIγS) at TUNL.

The radiative decay of compound nuclei at a high excitation energy region, but below the nucleon separation energy, is called the quasi-continuum, This region is described by the extreme statistical model. In other words, the γ-cascade following neutron capture is assumed to be a purely statistical process. The average transition rate can be represented by the PSFs and the LD. The Monte-Carlo code DICEBOX simulates radiative decay of compound nuclei from a highly excited initial state to the ground state. A variety of phenomenological models of the PSFs and LD are assumed as the input of the code. The most appropriate model and its parameters are chosen by comparing experimental and simulated γ-ray spectra.

6.1 γ-Ray Spectra Following Neutron Capture

In a neutron capture reaction, a bombarding neutron is absorbed by the target nucleus to form a compound nucleus at an excitation energy that is equal to the sum of the neutron separation energy and the kinetic energy of the neutron: $E^* = S_n + E_n$. The compound nuclei emits γ-rays which carry off the excitation energy. The γ-decays from highly excited compound states populates a number of intermediate states in the quasicontinuum. The experimental γ-ray spectra contributions from all possible transition γ-rays. As an example, Fig 6.1 shows a simple cascade scheme with a multiplicity m = 3 spectrum.

As shown in Fig 6.1, a nucleus decays into the intermediate state s_i emitting a γ ray with energy $E_{\gamma 1} = (S_n + E_n) - E_i$. The γ-rays emitted from a second generation transition between the intermediate states s_i and s_j and the third generation transition from the intermediate state s_j to ground state are also shown in Fig 6.1 (blue and red arrows). Since there are an enormous number of intermediate states between the capture and ground states, the γ-ray spectra accumulated by the numerous cascades become essentially continuous (Fig 6.1).

If we assume that the transition probability, p_{ij}, from a state s_i to s_j depends only the individual properties of these states, sequential transitions are considered independent

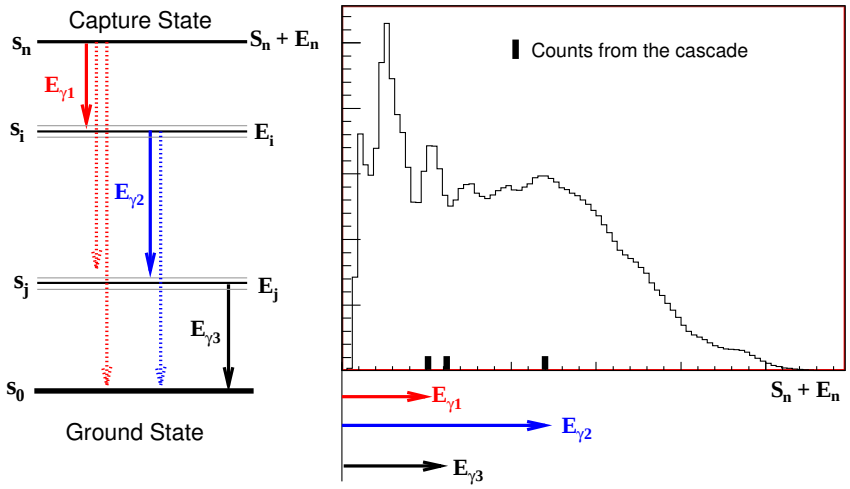

Figure 6.1: Schematic representation of the γ-ray spectrum accumulation for a multiplicity m = 3 cascade.

steps. In other words, the transition rate between the states s_i and s_j is independent of the way the excited state s_i is created. The excited state s_i can decay either by emitting a single γ-ray or several γ-rays via multiple steps.

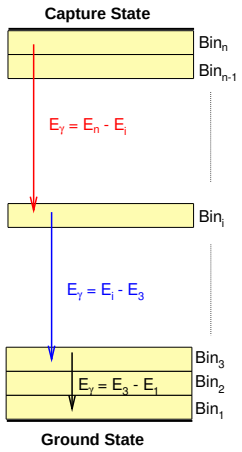

Figure 6.2: Transitions between the excitation bins.

Due to hardware and software detector thresholds, only the γ-rays with energy above the threshold E_{tr} are counted. Also, due to the detector resolution, the γ-rays within certain intervals of energy, $E_\gamma \pm \Delta E$, are counted in the same energy bin. the experimental γ-ray histogram is accumulated as a number of bins n, each with a width ΔE . Therefore, the nuclear γ-cascade consists of transitions between excitation energy bins with width ΔE. Figure 6.1 shows a schematic representation of the transitions between excitation bins.

All possible transitions probabilities between the excitation bins will form a *TransitionMatrix* (Eq. 6.1).

$$P = \begin{pmatrix} 0 & p_{cn} & p_{c(n-1)} & p_{c(n-2)} & \cdots & p_{c1} & p_{c0} \\ 0 & 0 & p_{n(n-1)} & p_{n(n-2)} & \cdots & p_{n1} & p_{n0} \\ 0 & 0 & 0 & p_{(n-1)(n-2)} & \cdots & p_{(n-1)1} & p_{(1-1)0} \\ \vdots & & & & & \vdots & \vdots \\ 0 & 0 & 0 & 0 & ... & 0 & p_{10} \\ 0 & 0 & 0 & 0 & ... & 0 & 1 \end{pmatrix} \tag{6.1}$$

where the specific element of the transition matrix p_{ij} is the transition probability between excitation bin_i and bin_j. For example, $p_{c(n-2)}$ is the transition probability from the initial capture state, c, to excitation bin $(n-2)$.

One can say the first indexes are read "from" and second indexes are read "to". Hence, the raw elements of the matrix corresponds to the probabilities of the transitions initiated from the same bin and the column elements of the matrix corresponds to the probabilities of the transitions into the same bin. Appendix G explains more about the transition matrix using a simple example. Note that all raw elements are normalized, $\sum_{j=0}^{n} p_{ij} = 1$. This means that if the nuclei is currently at any excited state i, then it must decay into one of the states located at lower energy.

Previous papers propose that the transition strength is a relatively smooth function of energy, $f(E)$. The transition strength between levels in bin i and j is assumed constant (here, we assume that each excitation bin_i contains ρ_i number of levels). Therefore the transition rate from a specific level at bin i to any level at bin j is proportional to $f(E_i - E_j)\rho(E_i)$.

The transition matrix (6.1) can be decomposed as

$$P = \begin{pmatrix} 0 & f_1 & f_2 & f_3 & ... & f_n & (1-\sum_{i=1}^{n} f_i\rho_{n-i+1})/\rho_n \\ 0 & 0 & f_1 & f_2 & ... & f_{(n-1)} & (1-\sum_{i=1}^{n-1} f_i\rho_{n-i})/\rho_{n-1} \\ 0 & 0 & 0 & f_1 & ... & f_{(n-2)} & (1-\sum_{i=1}^{n-2} f_i\rho_{n-i-1})/rho_{n-2} \\ \vdots & & & & & \vdots & \vdots \\ 0 & 0 & 0 & 0 & ... & 0 & 1/\rho_1 \\ 0 & 0 & 0 & 0 & ... & 0 & 1/\rho_0 \end{pmatrix} \begin{pmatrix} \rho_c \\ \rho_n \\ \rho_{(n-1)} \\ \vdots \\ \rho_1 \\ \rho_0 \end{pmatrix} \tag{6.2}$$

Hence, one can build the transition matrix as given in Eq. (6.2), if one knows the form of the energy dependent functions $f(E)$ and $\rho(E)$. The transition matrix completely

determines the statistical decay process of the compound nucleus. Interesting questions can be answered, such as what is the probability that the nucleus reaches the ground state after m steps for a given initial state? (i.e., what is the probability of the cascade having γ-ray multiplicity m) Other interesting questions include: On average, what is the probability the cascade populates each excitation bins? Or, on average, what is the probability to emit γ rays with energy E_γ for an m step cascade? etc ...

Unfortunately, the inverse problem –to determine the functional form of the transition strengths and the level density is the actual problem. Obviously, there is no straightforward way to obtain the transition matrix from the γ-ray spectra. However, at least, one may try to use statistical iterative methods such as *Markov Chain Monte Carlo*. For this thesis, we will use the DICEBOX + Geant4 code to determine the PSFs in the Gd isotopes.

The experimental γ-ray spectra for compound nuclei ^{156}Gd, ^{157}Gd and ^{159}Gd are shown in Fig. 6.3, 6.4, 6.5 and 6.6.

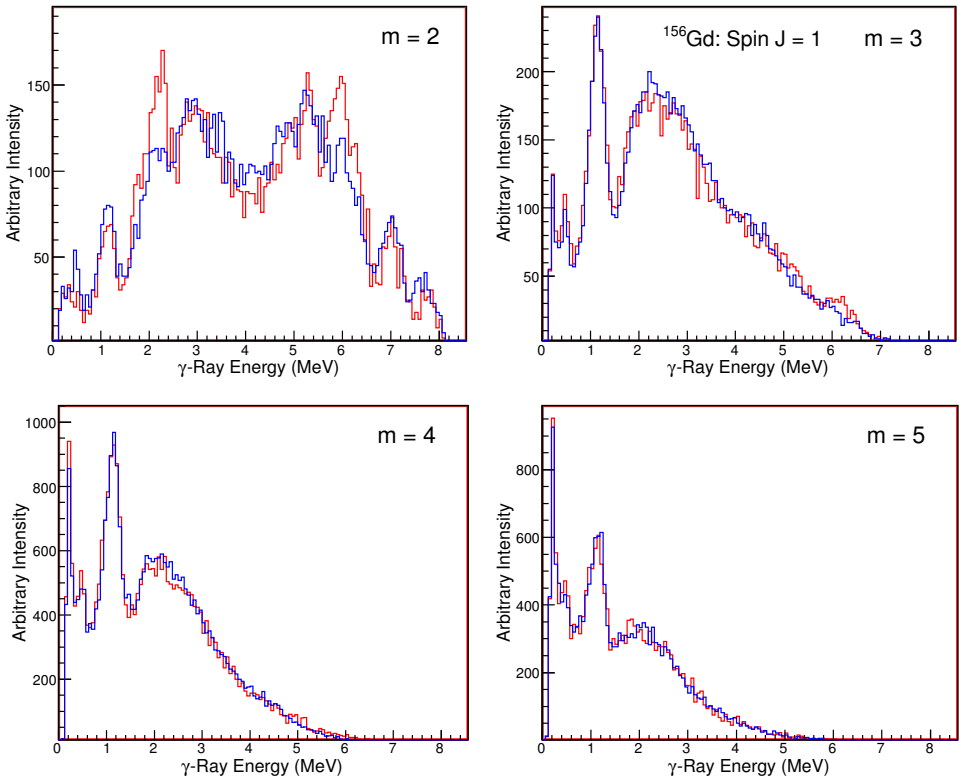

Figure 6.3: Experimental γ-ray spectra of spin J = 1 resonances in ^{156}Gd.

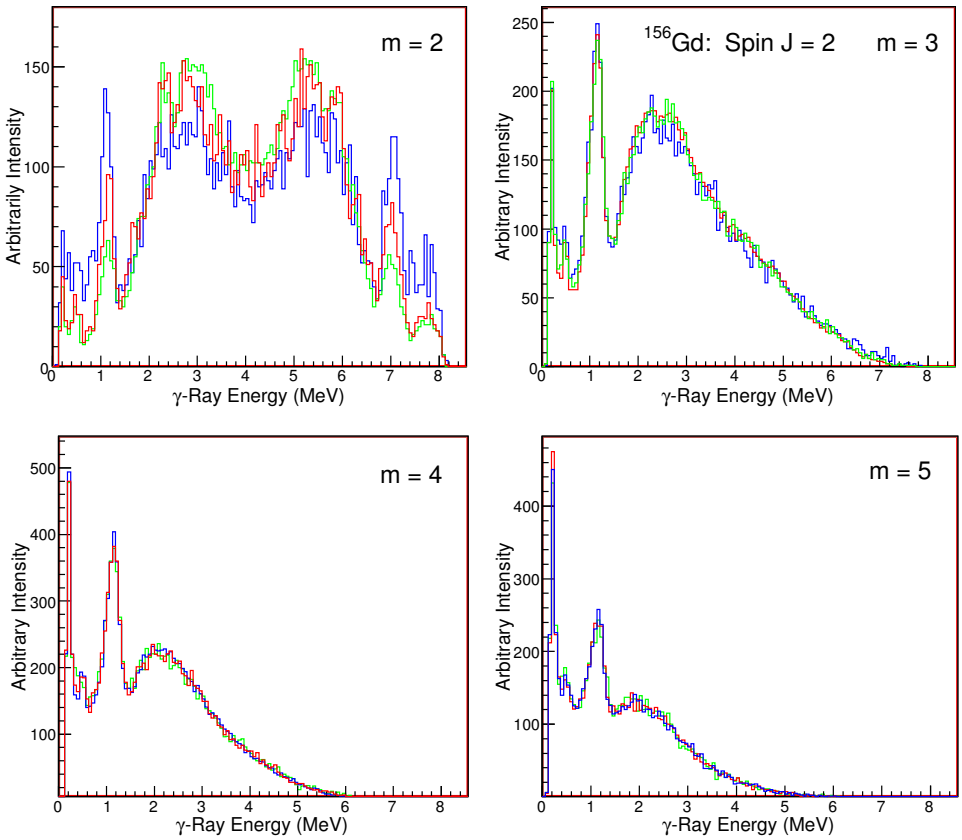

Figure 6.4: Experimental γ-ray spectra of spin J = 2 resonances in ^{156}Gd.

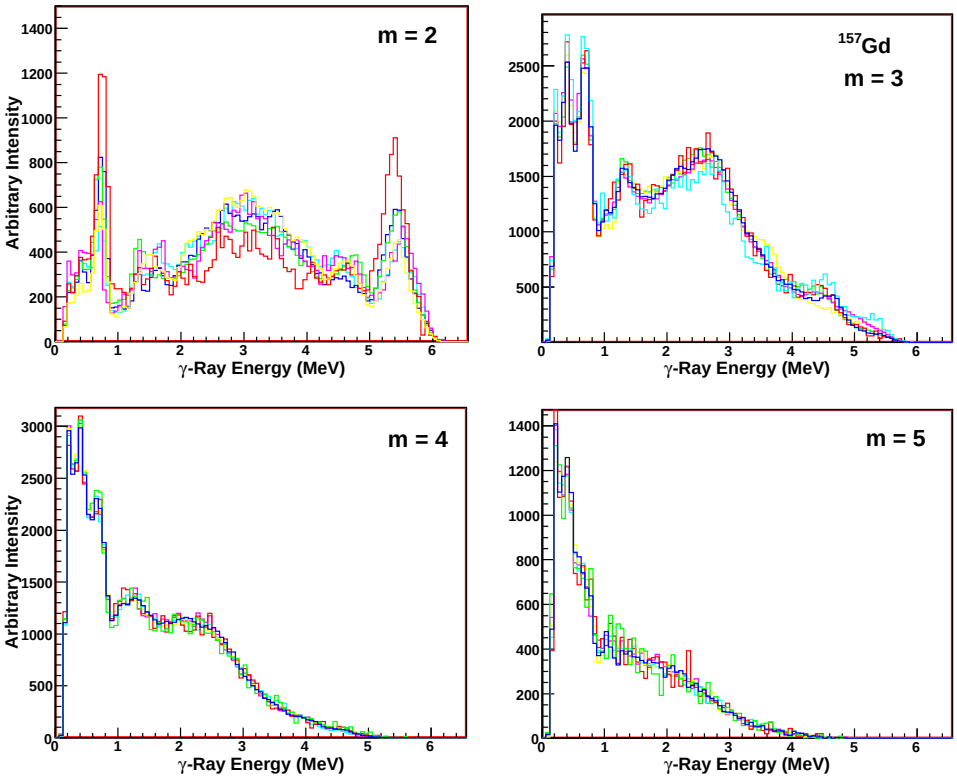

Figure 6.5: Experimental γ-ray spectra for ^{157}Gd, m = 3-5.

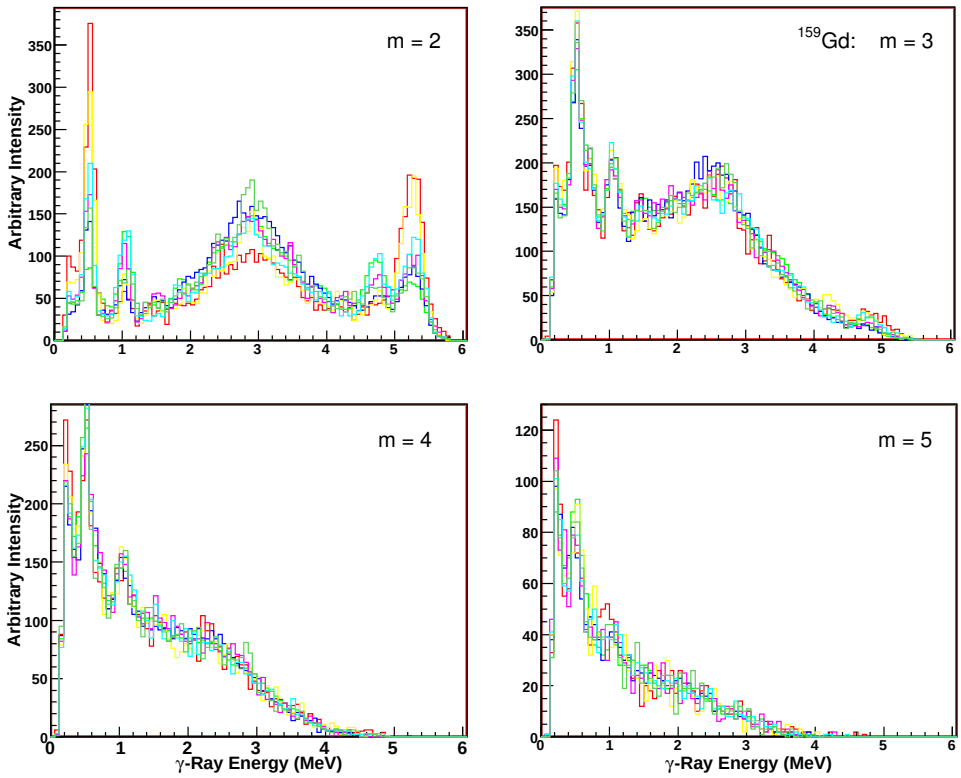

Figure 6.6: Experimental γ-ray spectra for ^{159}Gd, m = 3-5.

6.2 DICEBOX code

A detailed description of the statistical model code DICEBOX can be found in [30]. The assumptions used in DICEBOX code are outlined below:

- Below a certain energy, E_{crit}, the properties of all of the levels are known from spectroscopic experiments. This includes energies E, spins J, parities π, branching ratios I, multipole mixture coefficients δ, and the internal conversion coefficients α.
- Above this critical energy, the levels are assumed to be a random discretization of an a priori known level-density formula, $\rho(E, J)$.
- A partial radiation width $\Gamma_{if}^{(XL)}$, is a random realization of a chi-square-distributed

quantity the expectation value of which is equal to

$$y^2_{(XL)} f^{(XL)}(E_\gamma) E_\gamma^{2L+1} / \rho(E_i),$$

where $f^{(XL)}$ and ρ are given from the trial models and $y^2_{(XL)}$ is a randomly generated number drawn from a normal distribution with zero mean and unit variance.

- Selection rules governing the γ decay are fully observed
- Any pair of partial radiation widths $\Gamma_{if}^{(XL)}$ is statistically uncorrelated

The Reference Input Parameter Library (RIPL) collects all previous experimental data to provide input parameters for theoretical calculations of nuclear reactions involving light particles. Therefore, most of the input parameters for DICEBOX simulation are contained in the RIPL library. The level properties below the critical energy is taken from the RIPL.

6.2.1 PFS and LD Models used in simulations

LD parameter: The level density parameters are relatively well established in previous work. We used the Back-Shifted Fermi Gas (BSFG) formula Eq. (2.62) for all simulations. The level density parameters are obtained by fitting the model formula to the recommended spacing, D_0, of s-wave neutron resonances and to the cumulative number of low-lying levels. The free parameters of the BSFG model a and the excitation-energy shift E_1 (the energy back-shift) are listed in Table 6.1. Also the free parameters in the Constant Temperature Formula (CTF) nuclear temperature T and back shift E_0 are listed. The parameters listed in the Table 6.1 are extracted from reference [80].

Table 6.1: LD parameters for BSFG and CTF models.

Isotope	a(MeV^{-1})	E_1 (MeV)	T (MeV)	E_0 (MeV)
^{153}Gd	19.29(38)	0.87(8)	0.58(3)	1.94(21)
^{155}Gd	19.35(34)	0.67(13)	0.58(2)	1.74(22)
^{156}Gd	18.45(21)	0.36(9)	0.60(2)	0.61(17)
^{157}Gd	18.36(44)	0.70(12)	0.59(2)	1.63(20)
^{158}Gd	17.91(13)	0.28(8)	0.61(1)	0.69(16)
^{159}Gd	17.71(27)	0.71(12)	0.61(2)	1.68(19)

E1 strength: We used two models for the electric dipole transition strengths. As we discussed in Chapter 2 the standard Lorentzian shape model fails to represent E1 strength below the particle separation energy. Our first choice for the E1 strength was the Kadmenskii-Markushev-Furman (KMF) model. The second one is a "hybrid" model that it matches KMF at low γ-ray energies and matches the BA model at high energies. The experimental Giant Dipole Resonance (GDR) parameters listed in the RIPL database were obtained by fitting Lorentzian curves to total photo-neutron cross section data. The energy position of the maximum E_0, the damping width Γ and the peak cross section σ_0 is listed in Table 6.2.

Table 6.2: The experimental GDR parameters.

	Peak 1			Peak 2		
Isotope	E_0 (MeV)	σ_0 (mb)	Γ (MeV)	E_0 (MeV)	σ_0 (mb)	Γ (MeV)
^{156}Gd	11.2	180.0	2.6	15.20	242.0	3.60
^{157}Gd	11.2	180.0	2.6	15.20	242.0	3.60
^{158}Gd	11.7	165.0	2.6	14.90	249.0	3.80
^{160}Gd	12.23	215.0	2.77	15.96	233.0	5.28

The two peaks correspond to two different modes of dipole vibration of deformed nuclei. The macroscopic interpretations are referred to as vibration along the axis of symmetry and perpendicular to the symmetry axis.

M1 strength: The situation for M1 strength is more complicated. The experimental data on this mode of transition is sparse. Previous work with DANCE experiments observed that the M1 strength is very important in reproducing the γ-ray spectra. In other words, the parameters of models of M1 strength are adjusted in order to make the experimental and simulated spectra agree.

The first model we used for the M1 transition strength is given by

$$f_\gamma^{(M1)}(E_\gamma) = k_{M1} E_\gamma^k \tag{6.3}$$

where k and k_{M1} are free parameters. In single particle (SP) model, the transition strength, $f_\gamma^{(M1)}$ is constant that is the case of $k = 0$ in Eq. 6.3.

However, existence of the low energy resonance like structure in M1 transitions of deformed nuclei was first suggested theoretically [81] and it was confirmed in 1984 in

high-resolution inelastic electron experiment on ^{156}Gd [82]. Later on, many experiments observed strong low-lying magnetic excitations around 3 MeV in the rare earth nuclei. In the first theoretical model, the M1 mode is interpreted as a counter-rotational oscillation of the deformed proton body against the deformed neutron body which are usually referred to as *scissors mode*. In even-even nuclei, the scissors mode strength is closely correlated to the collective E2 excitation strength and, thus, depends quadratically on the nuclear deformation parameter [83]. Hence, studying systematic behavior of the scissors mode as a function of deformation will be one of our goals.

The microscopic model predicts another strong 1^+ excitations in nuclei wherein spin-orbit partners of large angular momentum are on opposite sides of the Fermi surface, which called *spin-flip* transition. With the spins aligned, the spin-orbit partners are in a slightly excited state and, the nucleon flip its spin orientation back to the lower energy configuration gives resonance transitions. Figure 6.7 shows protons spin-flip transitions in ^{40}Ar.

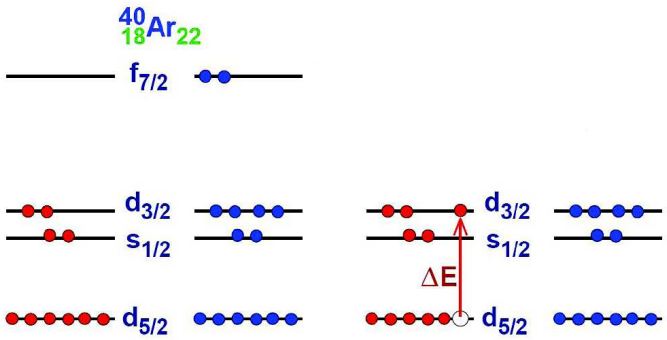

Figure 6.7: Protons spin flip M1 transition in ^{40}Ar. (Picture is taken from Dr.N.Pietralla, Darmstadt presentation)

The proton inelastic scattering (p,p') experiment [84], performed at TRIUMF, observed substantial M1 strength lying in the range 5-10 MeV for rare earth nuclei. The similar results found in many other deformed rare earth nuclei.

Based on the previous information, we considered two modes of M1 strength in the simulation for the decay of the ^{156}Gd compound nucleus; the scissors mode is located around 3 MeV and the spin-flip mode is located around 5-10 MeV. We tried several different combinations of models of E1 and M1 strength. The best reproduction of experimental spectra is obtained in double hump structure for both modes (spin-flip and scissors). Fig-

ure 6.8, 6.9, 6.10 and 6.11 shows comparison of the experimental and simulated γ-ray energy spectra for ^{156}Gd. For this simulation we used the hybrid model for the E1 strength and the parameters for the M1 strength are listed in Table 6.3.

Table 6.3: Spin-flip and scissors mode parameters in M1 transitions for ^{156}Gd.

M1 modes	E_0 (MeV)	σ_0 (mb)	Γ (MeV)
Scissors	2.6	0.1	0.2
	3.1	0.2	0.4
Spin-Flip	6.0	0.8	0.8
	8.0	1.2	1.8

Appendix F shows simulation result for more complicated cases. The same (as shown in Table 6.3) spin-flip modes are used for all levels. But the scissors mode has single resonance (2.6 0.1 0.4) built on all levels and an additional resonance term with parameter (3.1 0.4 0.4) is added for transitions to the ground state, first excited (2^+) and second excited (4^+) states.

6.3 Comparison with Experimental Results

In different models combinations of the decay simulation, the parameters of LD and E1 transition strengths was fixed at the values given in Table 6.2 and 6.1. Single-particle model is used for the E2 transition that is constant at $5 \cdot 10^{-9}$ MeV^{-3}. The parameters of M1 strength was adjusted to fit experimental and simulated spectra (Table 6.3).

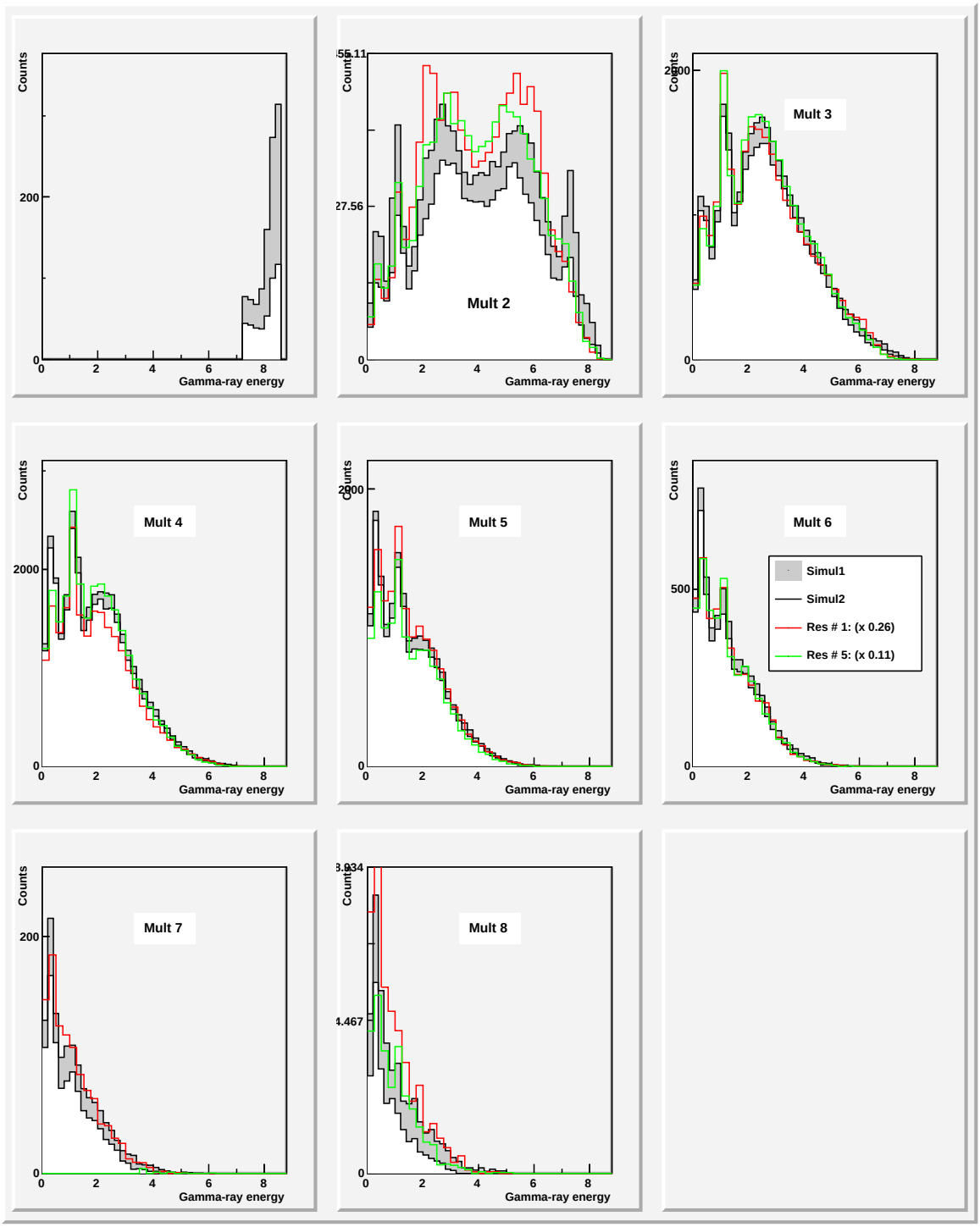

Figure 6.8: Comparison of γ-ray spectra of spin 1^- resonances.

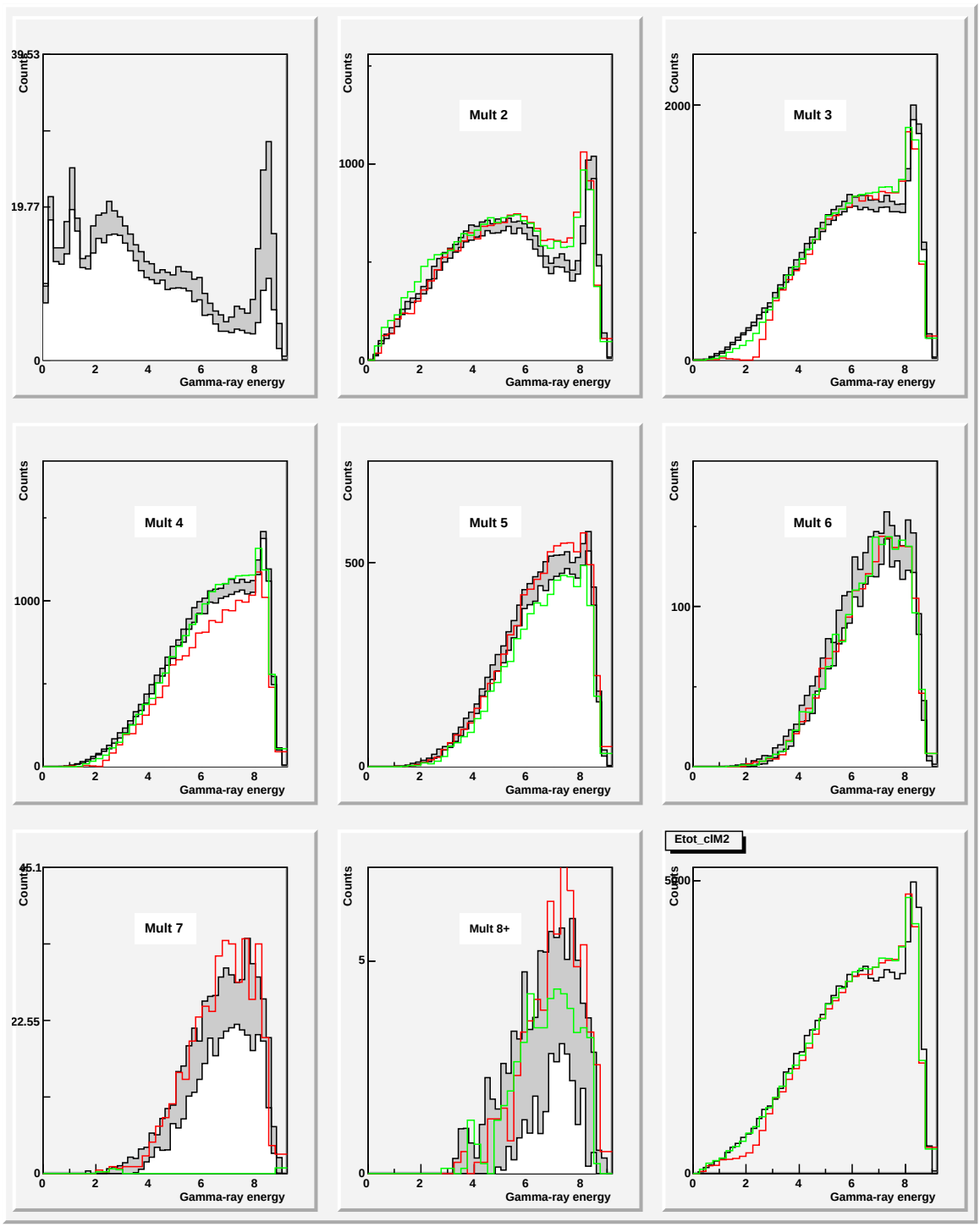

Figure 6.9: Comparison of total γ-ray spectra of spin 1^- resonances.

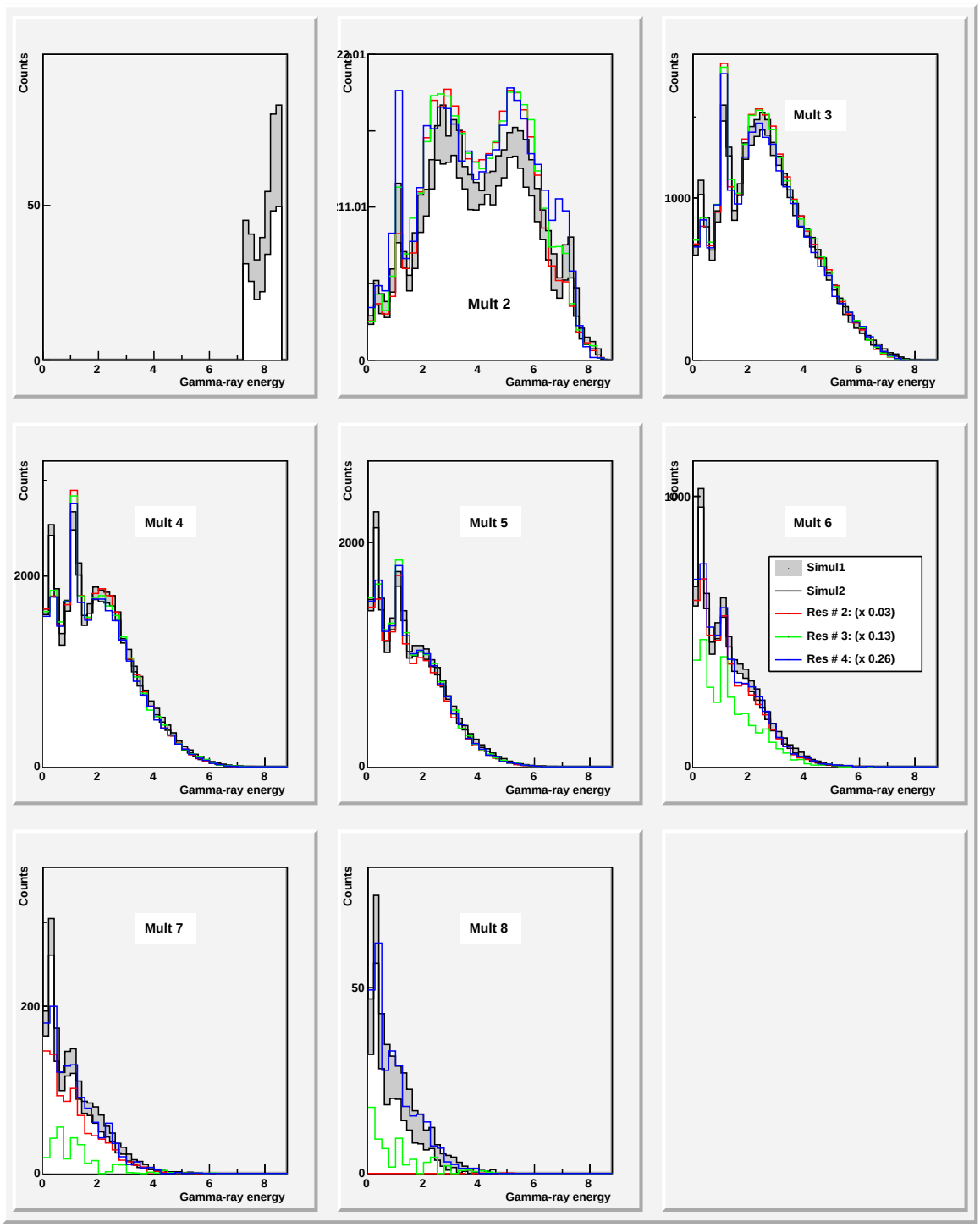

Figure 6.10: Comparison of γ-ray spectra of spin 2^- resonances.

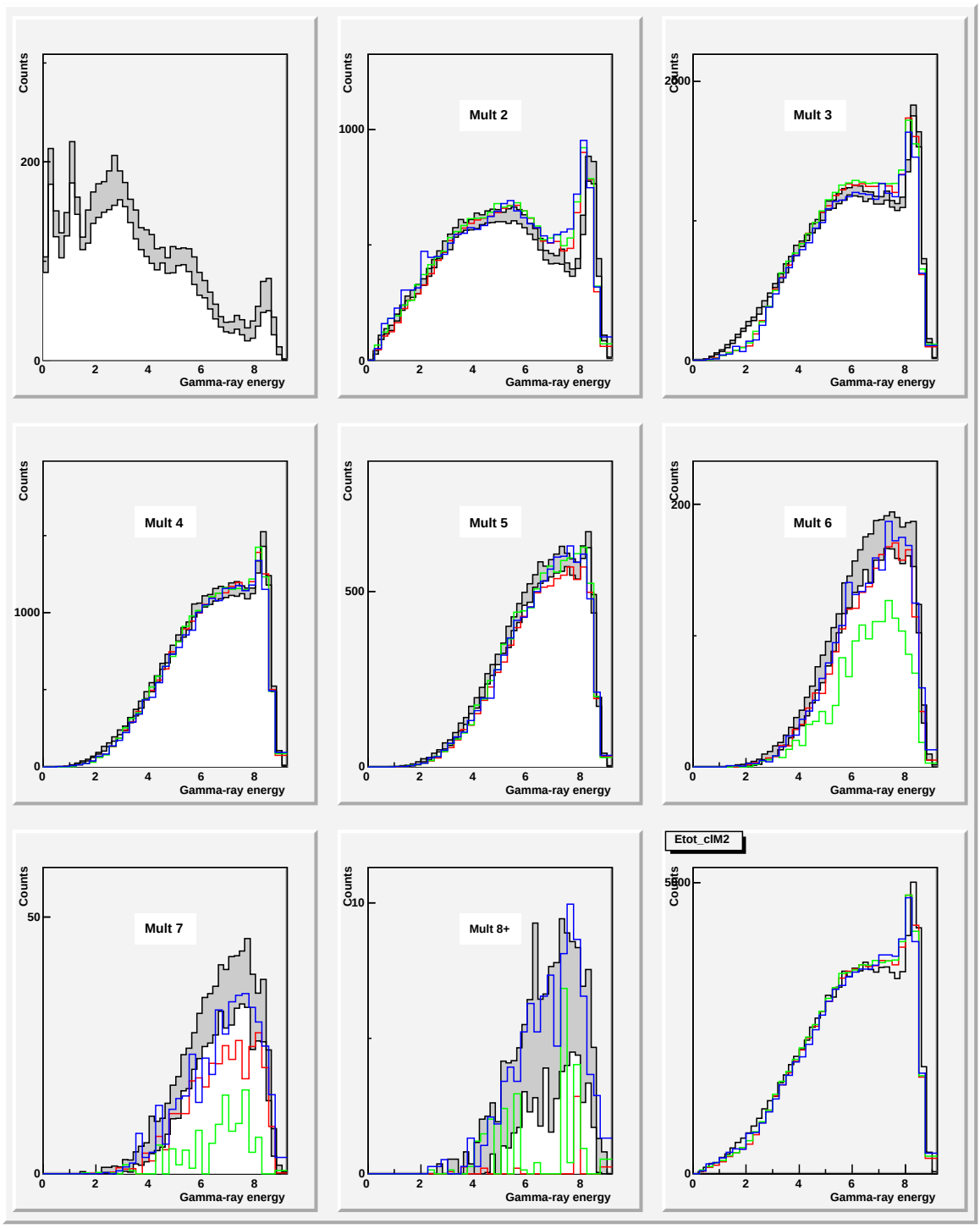

Figure 6.11: Comparison of total γ-ray spectra of spin 2^- resonances.

Chapter 7

Summary

The neutron capture reaction on ^{155}Gd, ^{156}Gd and ^{158}Gd has been measured with the DANCE calorimeter at Los Alamos Neutron Science Center.

A new spin determination method based on the statistical pattern recognition technique was developed. The method improves several type of shortcomings in previous methods: a) It does not use a prototype resonance. Instead, it estimates the maximum likelihood values of the multiplicity distribution using all of the neutron resonances. Thus it considers the Porter-Thomas fluctuations and experimental errors in the multiplicity distribution. b) By considering the multi-dimensional multiplicity space, this method uses as much information as is available and the sensitivity of the method is improved. c) It calculates the probability that the spin assignment is correct.

The computational limit of the method is determined by the minimum required separation of the multiplicity distributions and the minimum required sample size. If the distances between the clusters are small, then one cannot separate them into different spin groups. When not enough samples are available, even when the data is generated from well separated distributions, the correct assignment cannot be made, because there is not enough information in the data.

Using this new technique spins of almost all of the ^{155}Gd s-wave resonances have been assigned. The average level spacing of the s-wave neutron resonances was calculated as $D_0 = 1.76 \pm 0.09$ eV. The staircase plots were drawn for each spin group (Fig. 4.10) and the average level spacings determined as $D_{0.1} = 4.6 \pm 0.4$ eV and $D_{0.2} = 2.9 \pm 0.2$ eV, respectively, for $J = 1$ and $J = 2$ resonances. The level spacings for the two spin groups

are in agreement with the expected $2J + 1$ spacing dependence. Several spin doublets and one new resonance (at energy 22.2 eV) were observed.

The generalized method was used for spin assignments of s- and p-wave resonances in ^{94}Mo and ^{95}Mo isotopes. The results were compared with previous resonance data.

The ^{155}Gd(n,γ)^{156}Gd cross section has been measured for the incident neutron energy range from 1 eV to 10 keV. The results are in good agreement with other experiments. Neutron resonances parameters – Γ_γ and Γ_n – were obtained using the multilevel R-matrix code SAMMY.

Using the new resonance parameters the s-wave neutron strength function, S_0, was determined as $10^4 S_0 = 2.18 \pm 0.18$ that agrees well with Mughabghab value. A large majority of the DANCE values of Γ_γ appear to be larger than previously published average values. As a consequence, the average radiation widths was given $\langle \Gamma_\gamma \rangle = 123 \pm 12$ meV.

The Monte Carlo code DICEBOX was used to simulate γ-decay of the compound nucleus ^{156}Gd. Comparing the simulated and experimental spectra, we determined several low energy resonance-like structures in the M1 strength. The 4 peaks correspond to M1 spin-flip and scissors mode vibrations. The Lorentzian parameters of each mode was determined.

Bibliography

[1] A. M. Lane and R. G. Thomas, Rev. Mod. Phys. **30**, 257 (1958).

[2] A. M. Lane and J. E. Lynn, Nucl. Phys. **17**, 563 (1960).

[3] M. A. Preston, *Physics of the Nucleus*, Addison-Wesley Pub. Co., London, 1962.

[4] C. E. Porter and R. G. Thomas, Phys. Rev. **104**, 483 (1956).

[5] J. E. Lynn, *The Theory of Neutron Resonance Reactions*, Clarendon Press, Oxford, 1968.

[6] C. E. Porter, *Statistical Theories of Spectral Fluctuations*, Academic Press, New York, 1965.

[7] M. L. Mehta, *Random Matrices, 3rd ed.*, Elsevier Ltd., Amsterdam, 2004.

[8] H. A. Weidenmüller and G. E. Mitchell, Rev. Mod. Phys **81**, 539 (2009).

[9] U. Agvaanluvsan, Ph.D. thesis, NC State Unversity, 2002.

[10] S. F. Mughabghab, *Atlas of Neutron Resonances*, Elsevier Ltd., Amsterdam, 2006.

[11] H. Feshbach, C. E. Porter, and V. F. Weisskopf, Phys. Rev. **96**, 448 (1954).

[12] N. Bohr, Nature **137**, 344 (1936).

[13] E. Fermi, E. Amaldi, O. D'Agostino, F. Rasetti, and E. Segre, Proc. Roy. Soc. A **146**, 483 (1934).

[14] V. F. Weisskopf, Phys. Rev. **52**, 295 (1937).

[15] W. Hauser and H. Feshbach, Phys. Rev. **87**, 366 (1952).

[16] H. Feshbach, *Nuclear Spectroscopy, Part. B*, Academic Press, Inc., New York, 1960, p. 625.

[17] H. A. Bethe, Phys. Rev. **50**, 332 (1936).

[18] H. A. Bethe, Rev. Mod. Phys. **9**, 69 (1937).

[19] T. D. Newton, Can. J. Phys. **34**, 804 (1956).

[20] A. Gilbert and A. G. W. Cameron, Can. J. Phys. **43**, 1446 (1965).

[21] W. Dilg, W. Schantl, H. Vonach, and M. Uhl, Nucl. Phys. A **217**, 269 (1973).

[22] A. V. Ignatyuk, G. N. Smirenkin, and A. S. Tishin, Sov. J. Nucl. Phys. **21**, 255 (1975).

[23] S. K. Kataria, V. S. Ramamurthy, and S. S. Kapoor, Phys. Rev. C **18**, 549 (1978).

[24] A. S. Iljinov *et al.*, Nucl. Phys. A **543**, 517 (1992).

[25] A. V. Ignatyuk, *Handbook for Calculations of Nuclear Reaction Data*, IAEA-TECDOC-1034, (IAEA, Vienna, 1998), p. 65.

[26] P. Demetriou and S. Goriely, Nucl. Phys. A **695**, 95 (2001).

[27] G. H. Lang, C. W. Johnson, S. E. Koonin, and W. E. Ormand, Phys. Rev. C **48**, 1518 (1993).

[28] H. Nakada and Y. Alhassid, Phys. Lett. B **436**, 231 (1998).

[29] Y. Alhassid, S. Liu, and H. Nakada, Phys. Rev. Lett. **83**, 4265 (1999).

[30] F. Becvar, Nucl. Instum. Methods Phys. Res. A **417**, 434 (1998).

[31] M. Krticka, Ph.D. thesis, Charles Unversity, Prague, 2002.

[32] T. von Egidy, H. H. Schmidt, and A. N. Behkami, Nucl. Phys. A **481**, 189 (1988).

[33] V. F. Weisskopf, Phys. Rev. **83**, 1073 (1951).

[34] J. M. Blatt and V. F. Weisskopf, *Theoretical Nuclear Physics*, John Wiley and Sons, Inc., New York, 1952.

[35] G. A. Bartholomew, Ann. Rev. Nucl. Sci. **11**, 259 (1961).

[36] P. Axel, Phys. Rev. **126**, 671 (1962).

[37] R. T. Carpenter, in *International Conference on Nuclear Physics with Reactor Neutrons*, 1963, ed. F. E. Throw, ANL-6797, p. 194.

[38] C. M. McCullagh, M. L. Stelts, and R. E. Chrien, Phys. Rev. C **23**, 1394 (1981).

[39] J. Kopecky and M. Uhl, in *Measurement, Calculation and Evaluation of Photon Production Data*, 1994, NEA/NSC/DOC(95)1, p. 119.

[40] J. Kopecky, *Handbook for Calculations of Nuclear Reaction Data*, IAEA-TECDOC-1034, (IAEA, Vienna, 1998), p. 97.

[41] D. M. Brink, Ph.D. thesis, Oxford University, 1955.

[42] A. B. Migdal, J. Phys. (USSR) **8**, 331 (1944).

[43] M. Goldhaber and E. Teller, Phys. Rev. **74**, 1046 (1948).

[44] M. Krticka and F. Becvar, J. Phys. G **35**, 014025 (2008).

[45] F. Becvar, P. Cejnar, R. E. Chrien, and J. Kopecky, Phys. Rev. C **46**, 1276 (1992).

[46] Y. P. Popov, in *Proc. Neutron Induced Reactions, Topical Conf., Smolenice, Physics and Applications*, Vol 10, ed. P.Oblozynski, 1982, Bratislava, p. 121.

[47] S. G. Kadmenskii, V. P. Markushev, and V. I. Furman, Sov. J. Nucl. Phys. **37**, 165 (1983).

[48] J. Kopecky and R. E. Chrien, Nucl. Phys. A **468**, 285 (1987).

[49] S. F. Mughabghab and C. L. Dunford, Phys. Lett. B **487**, 155 (2000).

[50] J. Kopecky and M. Uhl, Phys. Rev. C **41**, 1941 (1990).

[51] J. Kopecky, M. Uhl, and R. E. Chrien, Phys. Rev. C **47**, 312 (1993).

[52] M. Heil *et al.*, Nucl. Instrum. Methods Phys. Res. A **459**, 229 (2001).

[53] M. Jandel *et al.*, Nucl. Instrum. Methods Phys. Res. B **261**, 1117 (2007).

[54] R. Reifarth *et al.*, Nucl. Instrum. Methods Phys. Res. A **531**, 530 (2004).

[55] J. M. Wouters *et al.*, IEEE Trans. Nucl. Sci. **53**, 880 (2006).

[56] N. M. Larson, Updated users guide for sammy, Technical Report ORNL/TM-9179/R7; ENDF-364/R, ORNL, 2007.

[57] R. Reifarth *et al.*, Review of geant simulations and comparison with first experiments at dance, Technical Report LA-UR-03-5560, LANL, 2003.

[58] C. Coceva, F. Corvi, P. Giacobbe, and G. Garraro, Nucl. Phys. A **117**, 586 (1980).

[59] S. A. Sheets *et al.*, Phys. Rev. C **76**, 064317 (2007).

[60] P. E. Koehler *et al.*, Phys. Rev. C **76**, 025804 (2007).

[61] K. Fukunaga, *Introduction to Statistical Pattern Recognition (Second Edition)*, Academic Press, Inc., San Diego, 1990.

[62] G. J. McLachlan and T. Krishnan, *The EM Algorith and Extensions*, John Wiley and Sons, Inc., New York, 1997.

[63] M. Krticka, Private Communications, 2009.

[64] Experimental Nuclear Reaction Data, BNL, US Dept. of Energy, http://www.nndc.bnl.gov/exfor.

[65] Evaluated Nuclear Data File, BNL, US Dept. of Energy, http://www.nndc.bnl.gov/endf.

[66] H. B. Moller, F. J. Shore, and V. L. Sailor, Nucl. Sci. Eng. **8**, 183 (1960).

[67] S. F. Mughabghab and R. E. Chrien, Phys. Rev. **180**, 1131 (1969).

[68] S. J. Friesenhahn, M. P. Fricke, D. G. Costello, W. M. Lopez, and A. D. Carlson, Nucl. Phys. A **146**, 337 (1970).

[69] G. Leinweber *et al.*, Nucl. Sci. Eng. **154**, 261 (2006).

[70] M. Asghar, P. Ribon, E. Silver, and J. Trochon, Nucl. Phys. A **145**, 549 (1970).

[71] F. N. Belyaev, V. P. Bolotskii, B. V. Efimov, and G. V. Muradyan, Yad. Fiz. **52**, 625 (1990).

[72] K. Wisshak *et al.*, Phys. Rev. C **52**, 2762 (1995).

[73] W. C. Chung *et al.*, J. Korean Phys. Soc. **50**, 409 (2007).

[74] W. C. Chung, T. I. Ro, G. Kim, M. Igashira, and T. Ohsaki, J. Korean Phys. Soc. **48**, 835 (2006).

[75] V. S. Shorin, V. N. Kononov, and E. D. Poletaev, Yad. Fiz. **19**, 5 (1974).

[76] M. Jandel *et al.*, Phys. Rev. C **78**, 034609 (2008).

[77] D. P. Barry, Ph.D. thesis, Rensselaer Polytechnic Institute, 2003.

[78] A. Pandita and H. M. Agrawal, J. Phys. Soc. Japan **61**, 3524 (1992).

[79] G. P. Gueorguiev, J. Honzatko, V. A. Khitrov, C. Panteleev, and A. M. Sukhovoj, Nuclear Physics A **740**, 20 (2004).

[80] T. von Egidy and B. Dorel, Phys. Rev. C **72**, 044311 (2005).

[81] N. L. Iudice and F. Palumbo, Phys. Rev. Lett. **41**, 1532 (1978).

[82] D. Bohle *et al.*, Phys. Lett. B **137**, 27 (1984).

[83] N. Pietralla *et al.*, Phys. Rev. C **52**, R2317 (1995).

[84] D. Frekers *et al.*, Phys. Lett. B **244**, 178 (1990).

Appendices

APPENDIX A

Spin assignments of the neutron resonances in ^{155}Gd.

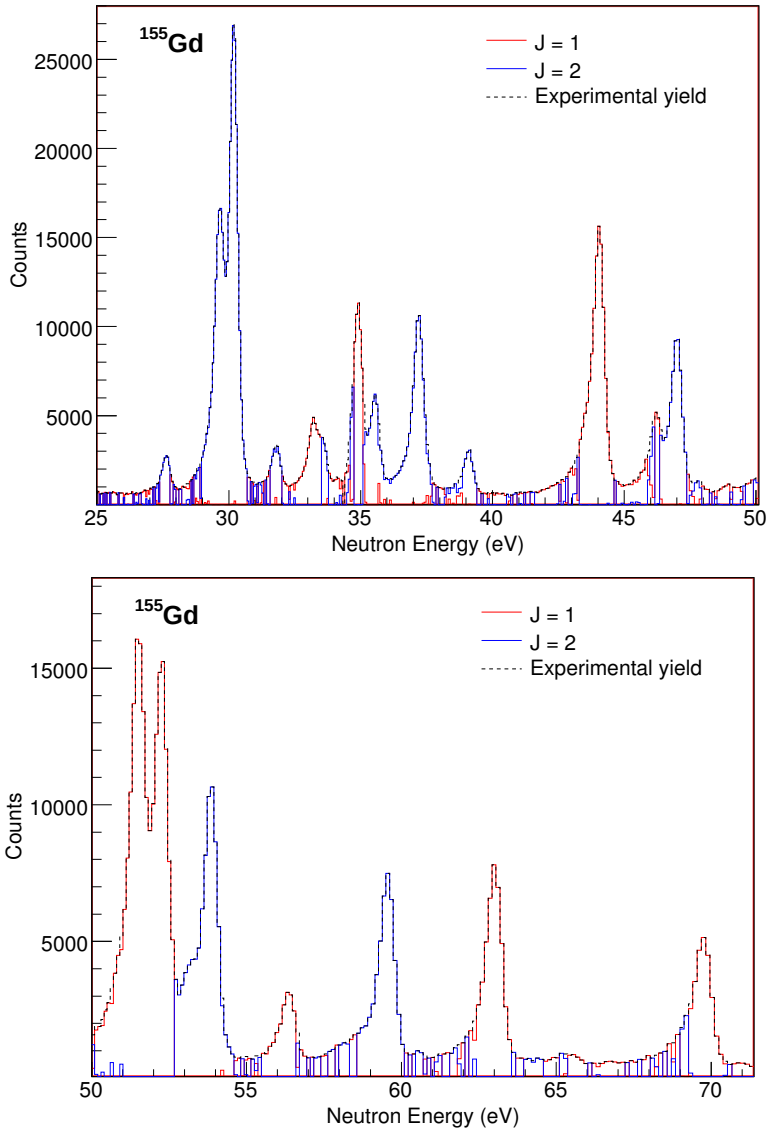

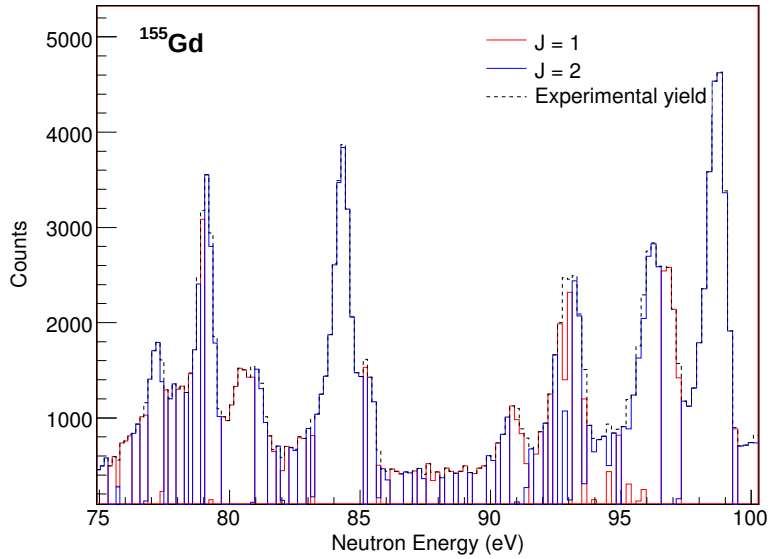
155Gd
J = 1
J = 2
Experimental yield
Counts
Neutron Energy (eV)
5000
4000
3000
2000
1000
75
80
85
90
95
100

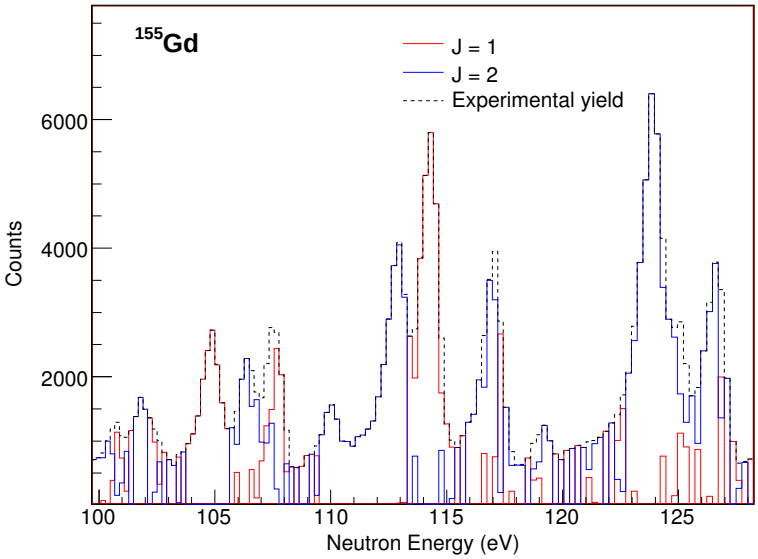
155Gd
J = 1
J = 2
Experimental yield
Counts
Neutron Energy (eV)
6000
4000
2000
100
105
110
115
120
125

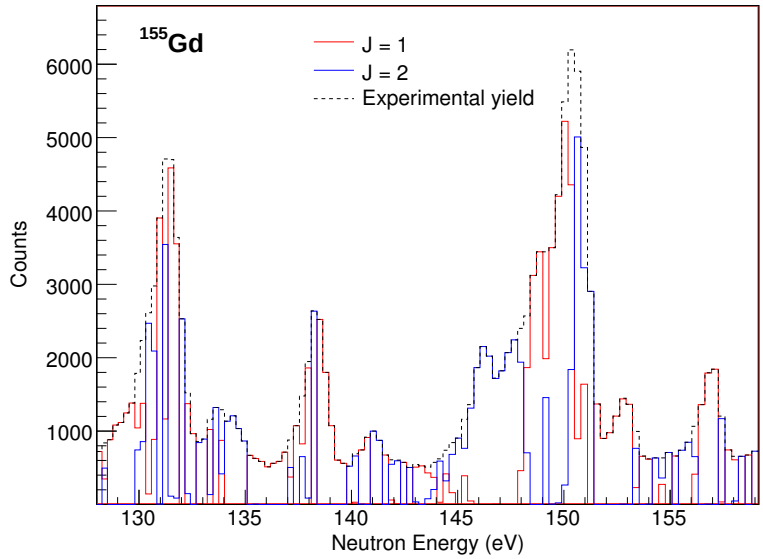
155Gd
J = 1
J = 2
Experimental yield
Counts
Neutron Energy (eV)
6000
5000
4000
3000
2000
1000
130
135
140
145
150
155

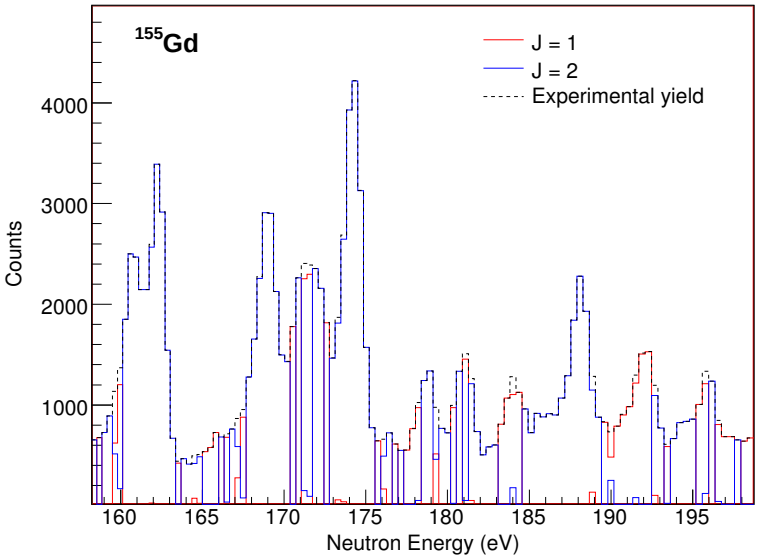
155Gd
J = 1
J = 2
Experimental yield
Counts
Neutron Energy (eV)
4000
3000
2000
1000
160
165
170
175
180
185
190
195

APPENDIX B

γ-Ray spectra of the s-wave resonances in ^{95}Mo that was mis-assigned as p-wave resonances.

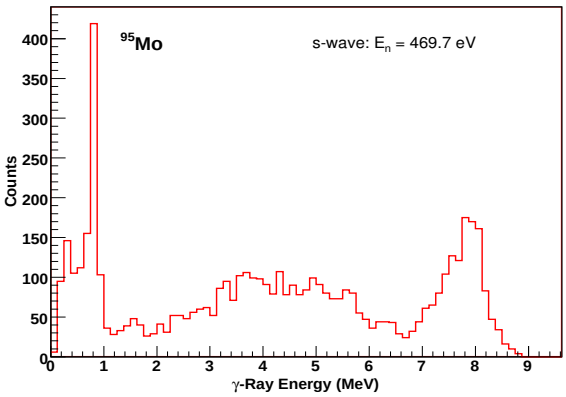

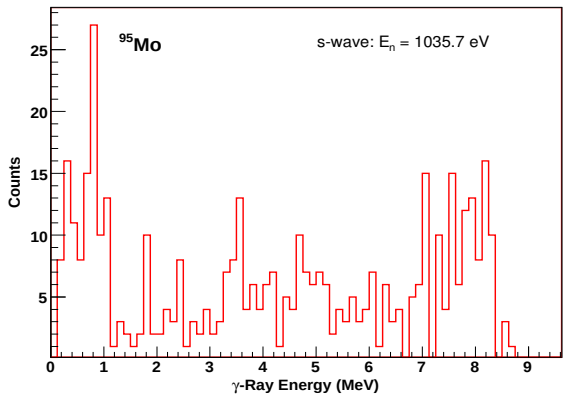

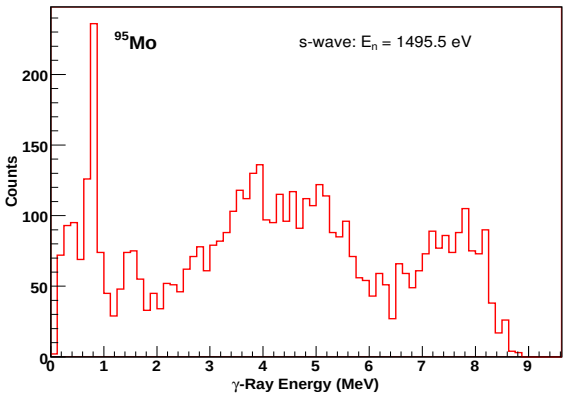

APPENDIX C

Spin assignments of the neutron resonances in ^{95}Mo.

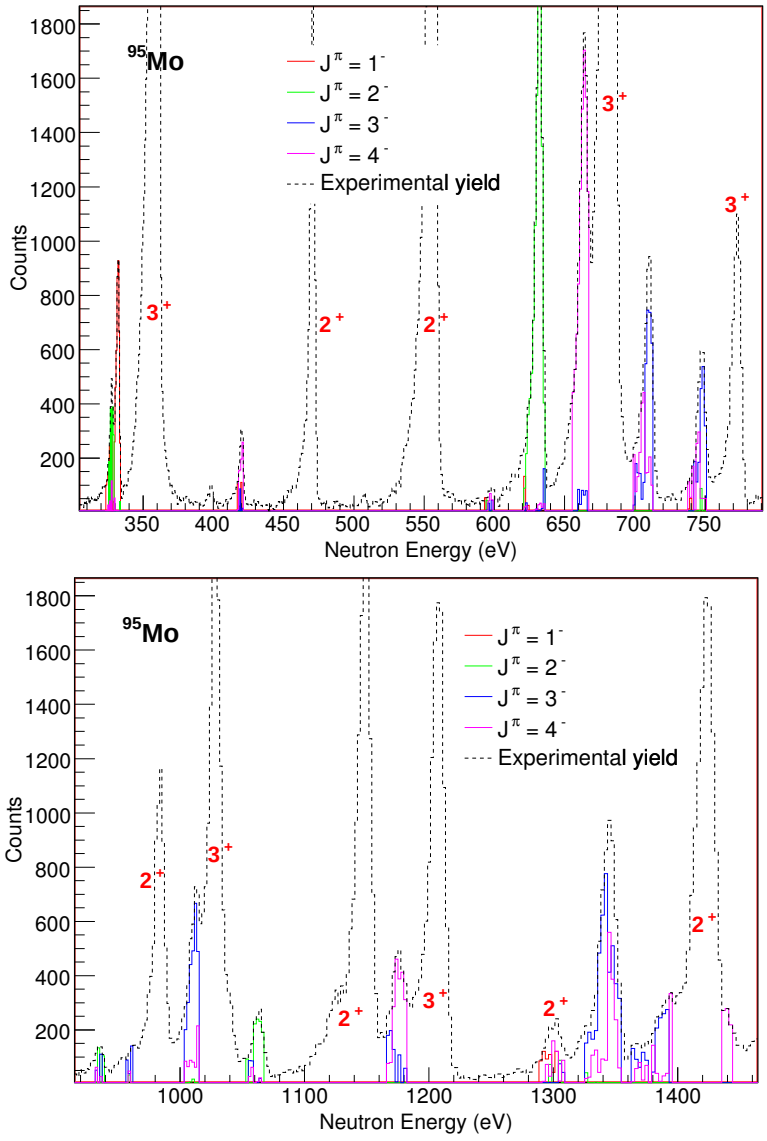

APPENDIX D

Spin assignments of the neutron resonances in ^{94}Mo.

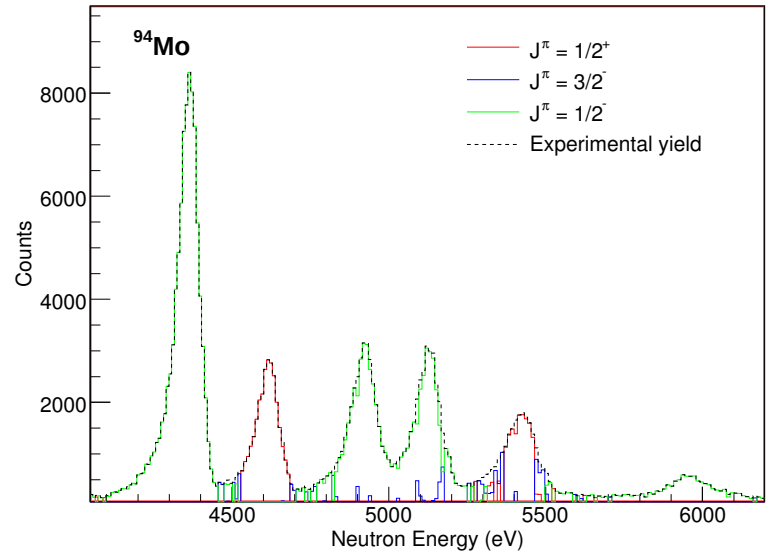

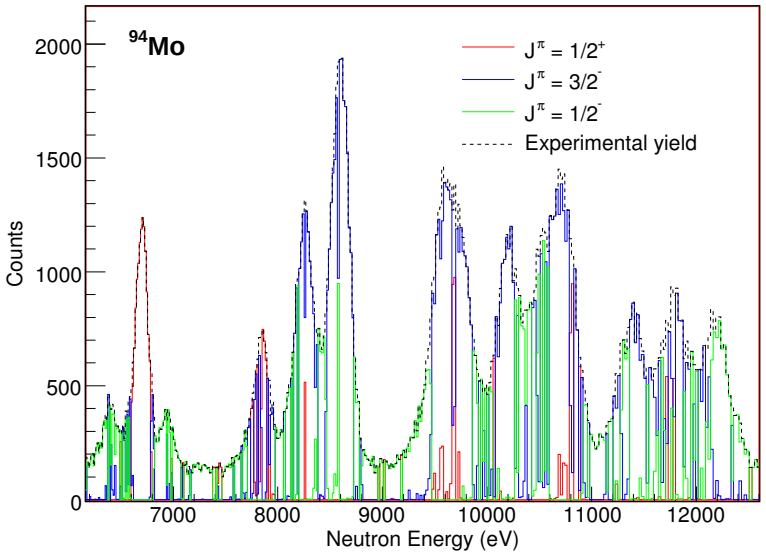

APPENDIX E

γ-Ray spectrum of s-wave resonances at neutron energy 5428 eV, 7865 eV, 9705 eV and 10776 eV.

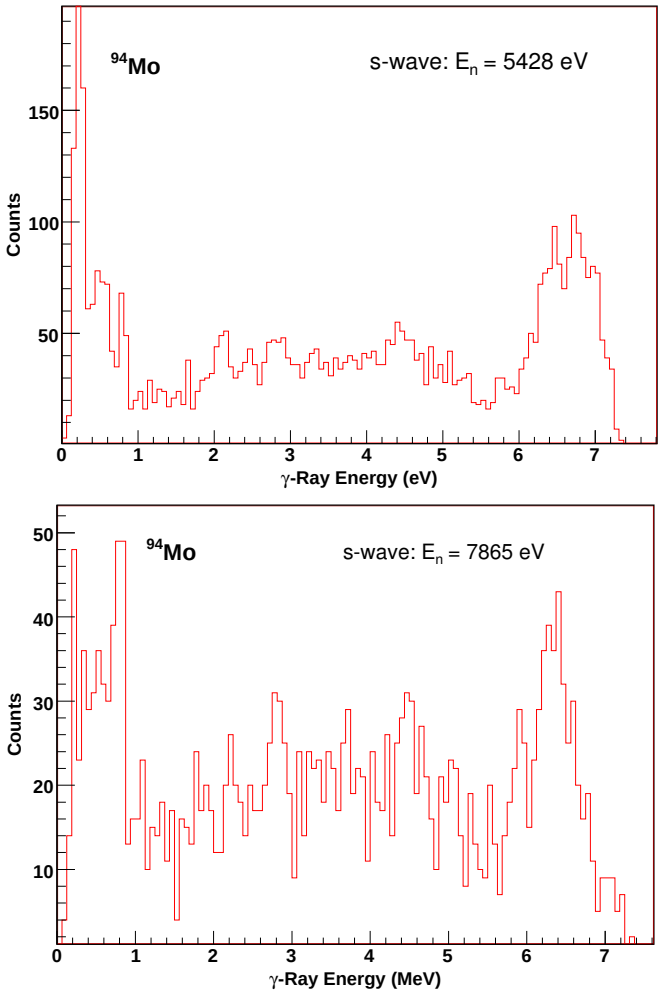

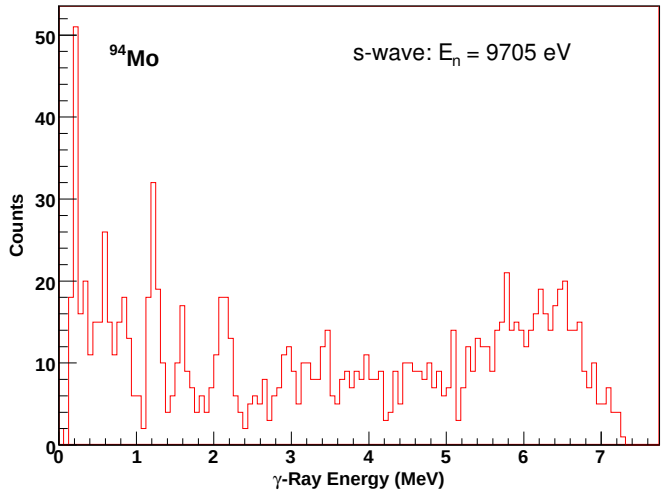
94Mo
s-wave: En = 9705 eV
Counts
γ-Ray Energy (MeV)

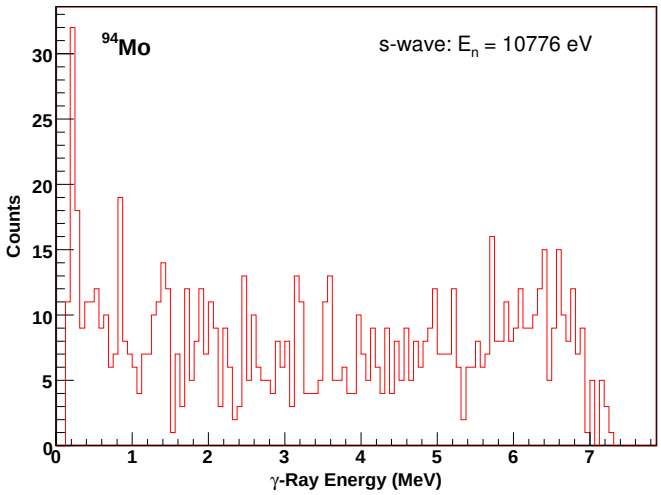
94Mo
s-wave: En = 10776 eV
Counts
γ-Ray Energy (MeV)

γ-Ray spectrum of p-wave resonances at neutron energy 10752 eV.

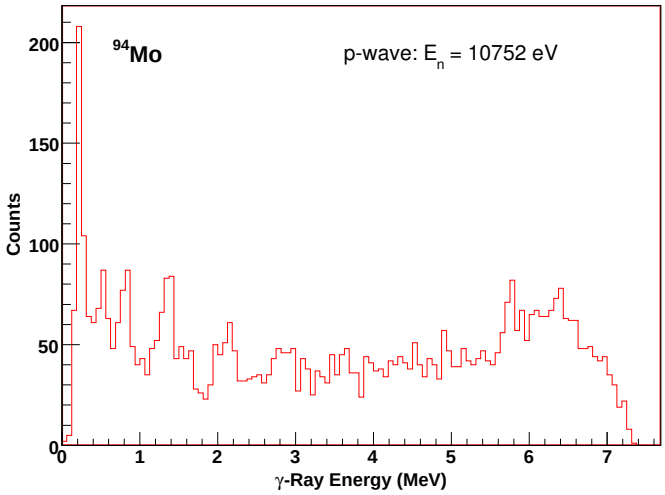

APPENDIX F

SAMMY Fit results of the resonances in ^{155}Gd.

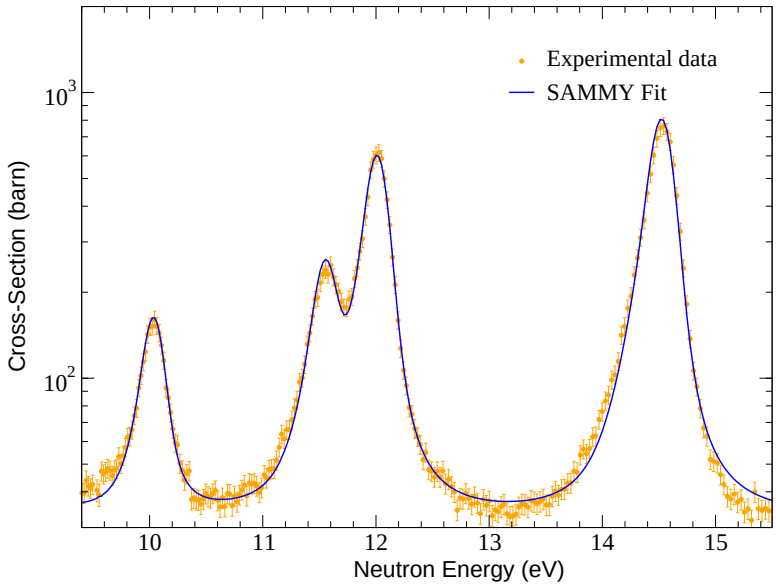

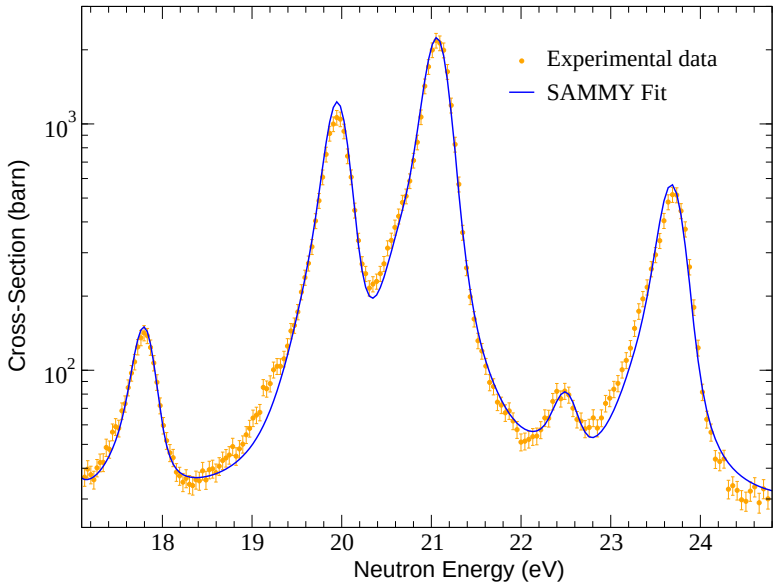

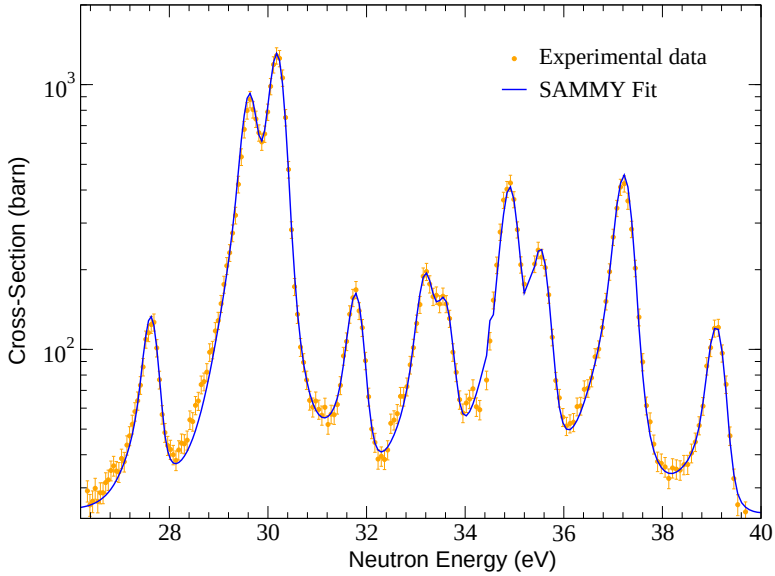
Experimental data
SAMMY Fit
Cross-Section (barn)
Neutron Energy (eV)
10^3
10^2
28
30
32
34
36
38
40

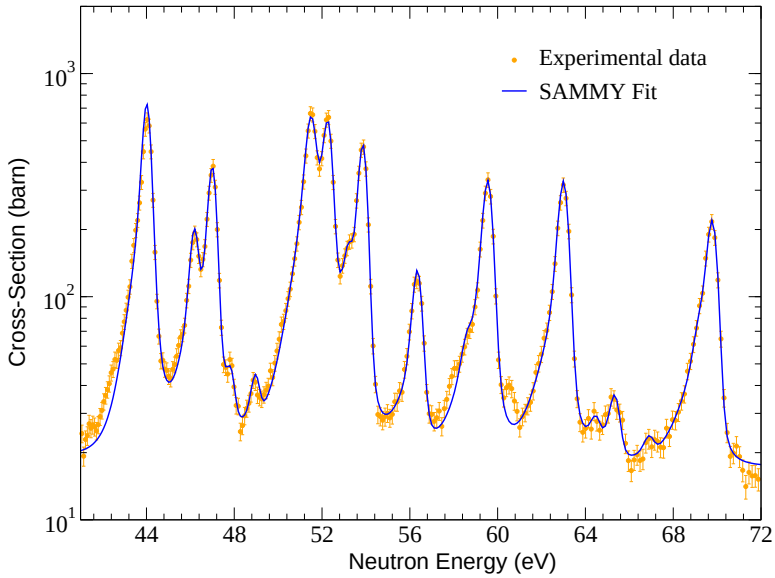
Experimental data
SAMMY Fit
Cross-Section (barn)
Neutron Energy (eV)
10^3
10^2
10^1
44
48
52
56
60
64
68
72

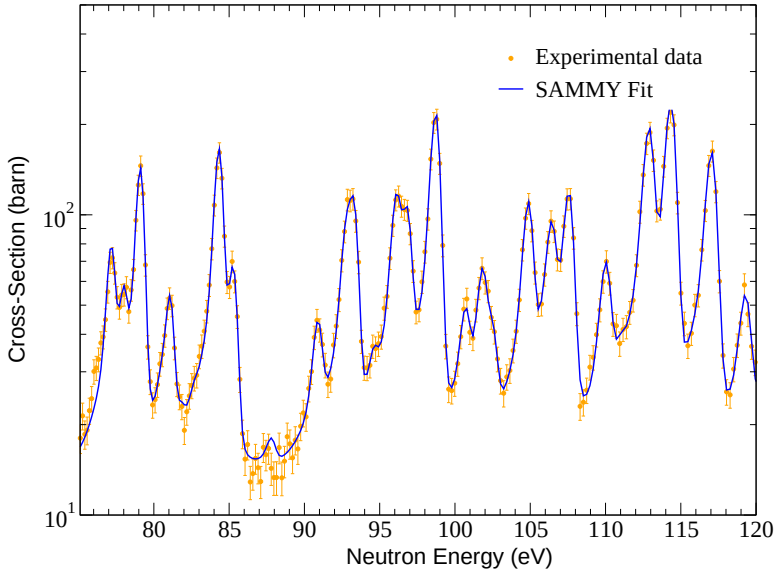
Experimental data
SAMMY Fit
Cross-Section (barn)
10^2
10^1
80
85
90
95
100
105
110
115
120
Neutron Energy (eV)

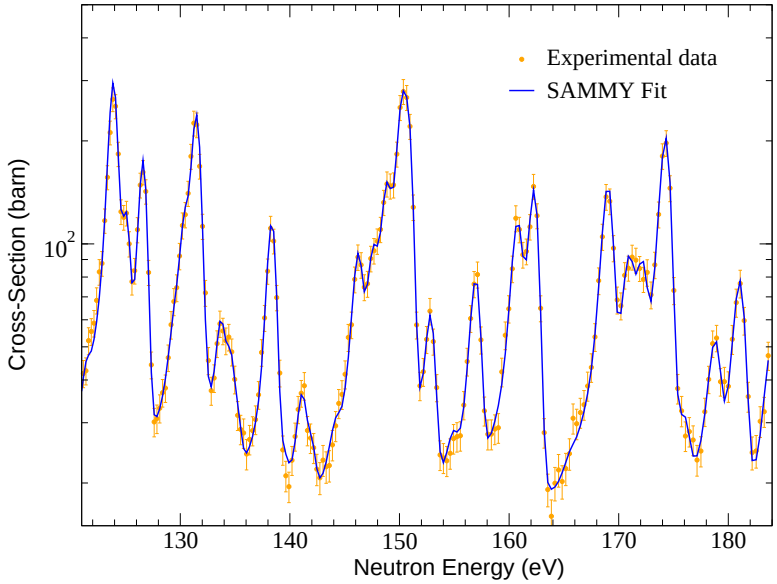
Experimental data
SAMMY Fit
Cross-Section (barn)
10^2
130
140
150
160
170
180
Neutron Energy (eV)

APPENDIX G

Compound nuclear γ-ray cascade with independent steps may be considered a Markovian process. In mathematics, a Markov chain, is a random process where all information about the future is contained in the present state (i.e. one does not need to examine the past to determine the future). To be more exact, the process has the Markov property, meaning that future states depend only on the present state, and are independent of past states. In other words, the description of the present state fully captures all the information that could influence the future evolution of the process. For the sequence of random variables $X_1, X_2, X_3, ..., X_n$ with the Markov property, it may be written formally,

$$Pr(X_{n+1} = x | X_1 = x_1, X_2 = x_2, ..., X_n = x_n) = Pr(X_{n+1} = x | X_n = x_n) \qquad (.1)$$

The possible values of X_i form a countable set S called the state space of the chain.

To build a transition matrix for the nuclear cascade, first consider a simple nuclei that has only 3 discrete excited states above the ground state (Fig 6.1). The states are numbered from s_0 to s_3 starting from ground state. Let's denote a transition probability from state s_i to s_j as p_{ij}. So, for example, transition probability from state s_3 to s_2 is p_{32}. If the cascade (chain) is initiated from the capture state s_3, in first step, it emits a γ-ray and comes to the one of the levels below s_3 (the probability stay at same state is zero). If the nuclei is at state s_2 it will decay into level s_1 or s_0 but it's not goes back to state s_3. For the state s_1 it has only one possibility come to the ground state. If the nuclei is at ground state s_0, then it will stay there forever. So, we have a chain with 4 possible states that numbered s_3, s_2, s_1 and s_0. The transition matrix, P, is given as

$$P = \begin{array}{c} s_3 \\ s_2 \\ s_1 \\ s_0 \end{array} \begin{pmatrix} 0 & p_{32} & p_{31} & p_{30} \\ 0 & 0 & p_{21} & p_{20} \\ 0 & 0 & 0 & p_{10} \\ 0 & 0 & 0 & 1 \end{pmatrix} \qquad (.2)$$

The ij-th entry, p_{ij}, of the matrix is a probability to populate level s_j in the next step, if the nuclei is currently at state s_i and this probability does not depend upon which states the nuclei was in before the current.

The transition matrix has property given in following theorems and the proofs may be found in any literature.

Theorem 1: Let P be the transition matrix of a Markov chain. The ijth entry p_{ij}^n of the matrix P^n gives the probability that the Markov chain, starting in state s_i, will be in state s_j after n steps.

Theorem 2: Let P be the transition matrix of a Markov chain, and let u be the probability vector which represents the starting distribution. Then the probability that the chain is in state s_i after n steps is the ith entry in the vector

$$u^{(n)} = uP^n. \tag{.3}$$

Consider again a simple cascade given above. One may easily calculate a square of transition matrix given in Eq. (.2) as.

$$P^2 = \begin{pmatrix} 0 & 0 & p_{32}p_{21} & 1 - p_{32}p_{21} \\ 0 & 0 & 0 & 1 \\ 0 & 0 & 0 & 1 \\ 0 & 0 & 0 & 1 \end{pmatrix} \tag{.4}$$

The obvious consequence is that the probability of the nuclei comes to the ground state is 1 if the cascade initiated from level s_2 or below. For the cascade initiated from capture state, s_3, the probability to be at state s_1 is $p_{32}p_{21}$ and the probability to come ground state is $1 - p_{32}p_{21}$.

We know that the nuclear γ-ray cascade is always initiated from capture state (s_3). So, the probability vector for initial distribution is $u^{(0)} = \begin{pmatrix} 1 & 0 & 0 & 0 \end{pmatrix}$. The probability vector $u^{(1)}$ after first cascade is given by Theorem 2.

$$u^{(1)} = u^{(0)}P = \begin{pmatrix} 0 & p_{32} & p_{31} & 1 - p_{32} - p_{31} \end{pmatrix}$$

And the probability vector $u^{(2)}$ after second cascade is.

$$u^{(2)} = u^{(0)}P^2 = \begin{pmatrix} 0 & 0 & p_{32}p_{21} & 1 - p_{32}p_{21} \end{pmatrix}$$

At last, the nuclei will come its ground state after third cascade and the probability of being excited states are zero. This will seen in P^3 matrix as all entries are zero except last column that has entries 1. The ground state is an absorption state and the chain is called *absorbing Markov chain.*

APPENDIX H

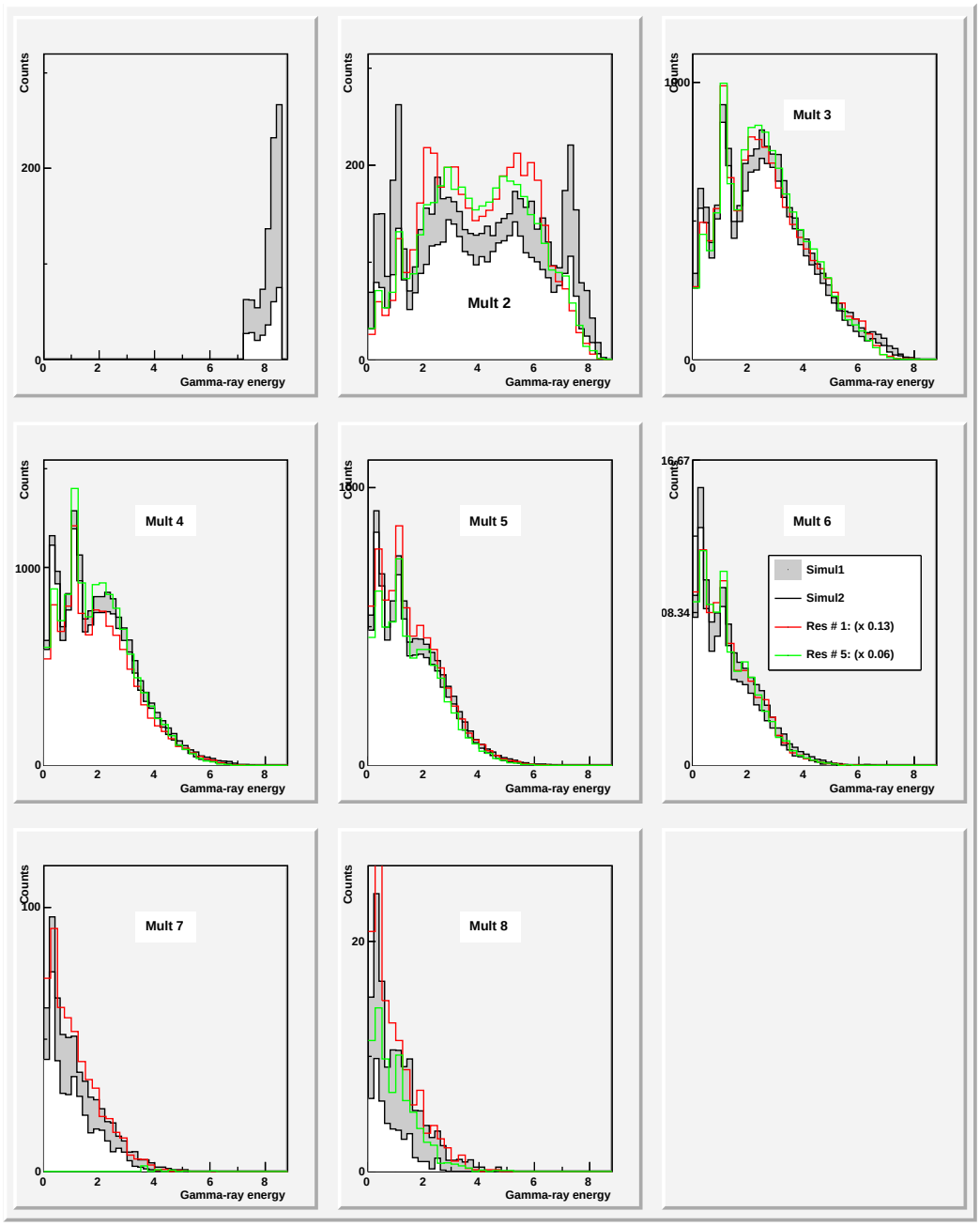

Figure .1: Comparison of γ-ray spectra of spin 1^- resonances.

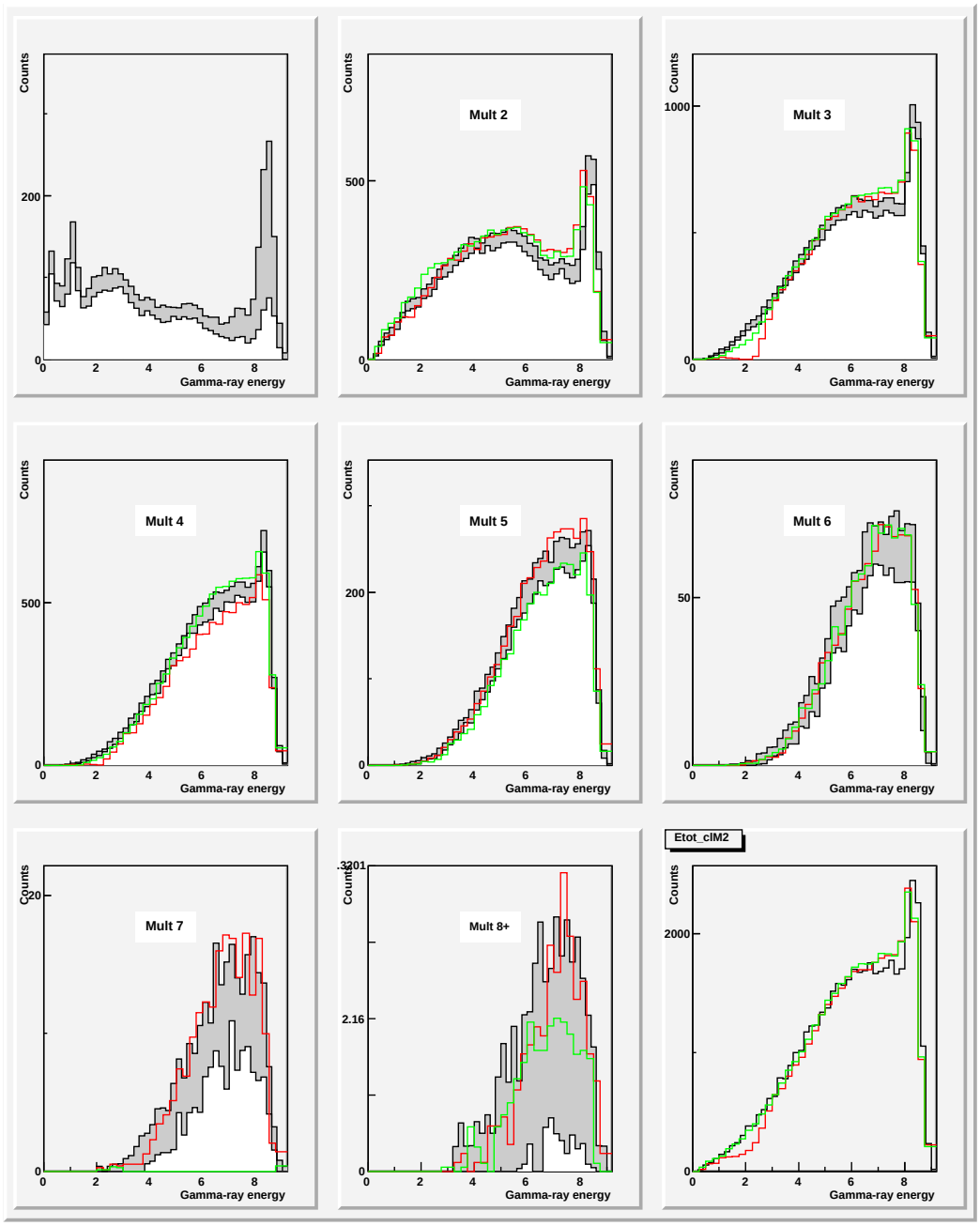

Figure .2: Comparison of total γ-ray spectra of spin 1^- resonances.

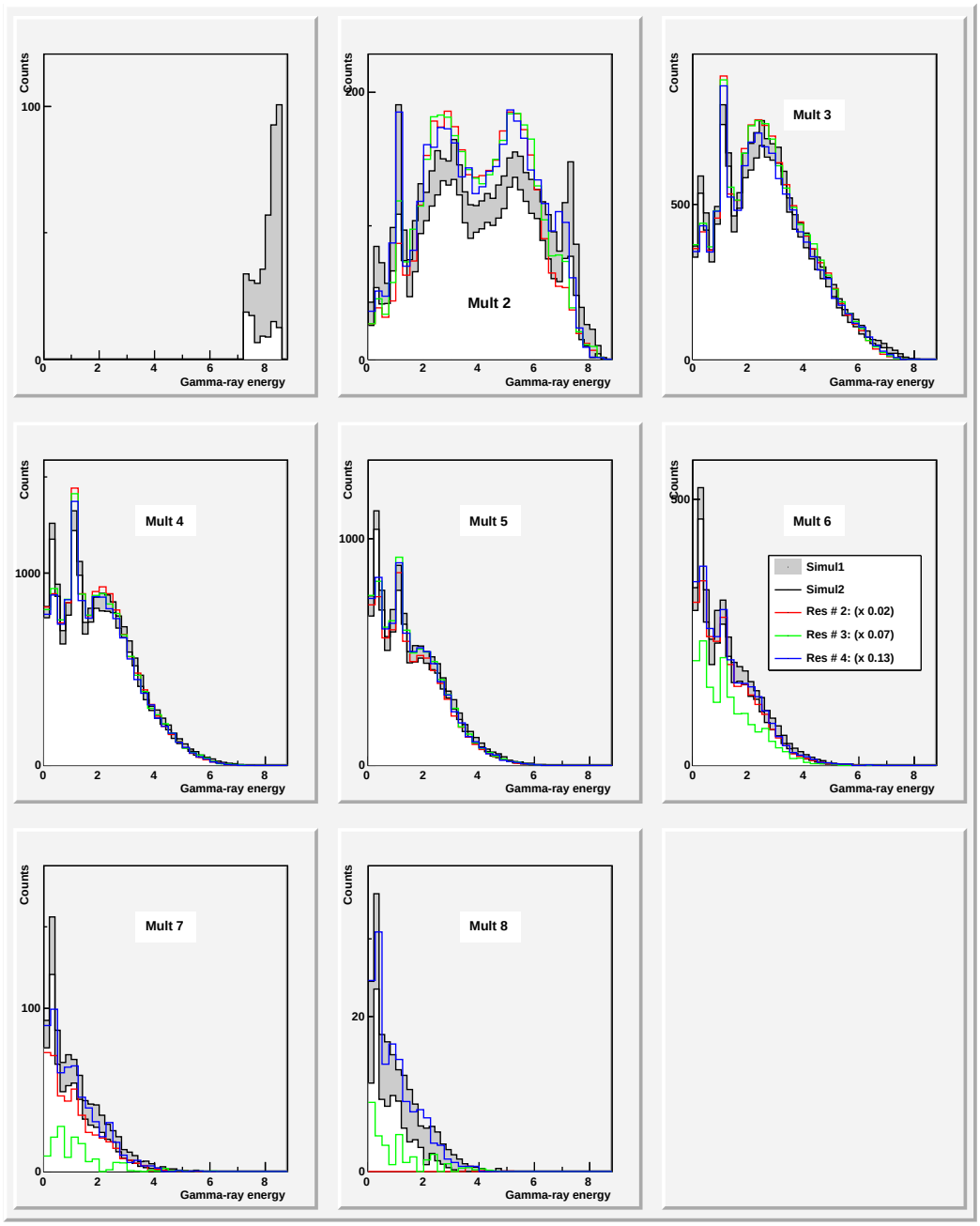

Figure .3: Comparison of γ-ray spectra of spin 2^- resonances.

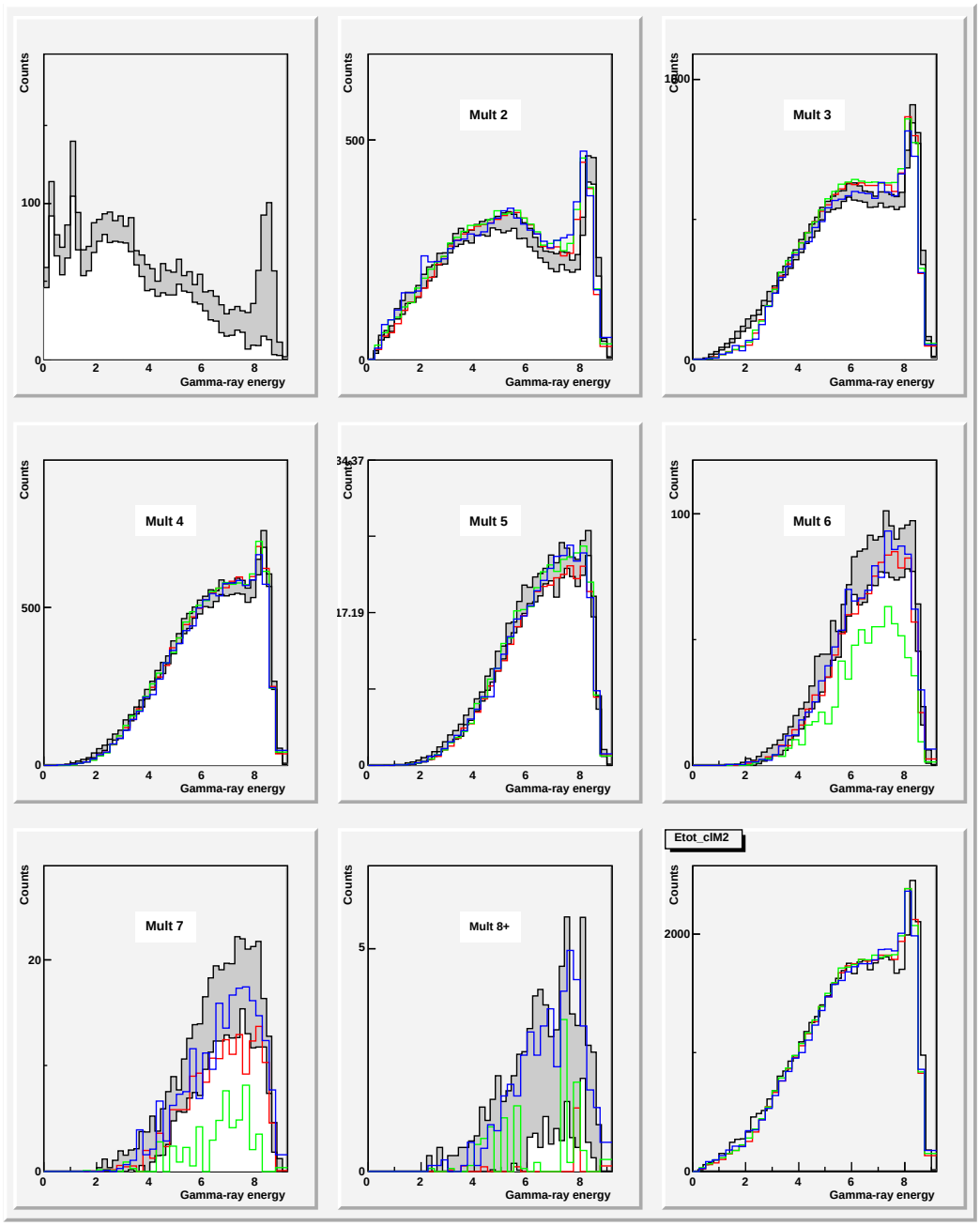

Figure .4: Comparison of total γ-ray spectra of spin 2^- resonances.